PolyPublie
Polytechnique Montréal

POLYTECHNIQUE MONTRÉAL
UNIVERSITÉ D'INGÉNIERIE

Titre: Title:	Spherical Bragg Resonators for Advanced Electromagnetic Emission Engineering and Lasing Applications
Auteur: Author:	Yalina Garcia Puente
Date:	2024
Type:	Mémoire ou thèse / Dissertation or Thesis
Référence: Citation:	Garcia Puente, Y. (2024). Spherical Bragg Resonators for Advanced Electromagnetic Emission Engineering and Lasing Applications [Thèse de doctorat, Polytechnique Montréal]. PolyPublie. https://publications.polymtl.ca/59214/

Document en libre accès dans PolyPublie
Open Access document in PolyPublie

URL de PolyPublie: PolyPublie URL:	https://publications.polymtl.ca/59214/
Directeurs de recherche: Advisors:	Raman Kashyap
Programme: Program:	Génie physique

Ce fichier a été téléchargé à partir de PolyPublie, le dépôt institutionnel de Polytechnique Montréal
This file has been downloaded from PolyPublie, the institutional repository of Polytechnique Montréal

https://publications.polymtl.ca

POLYTECHNIQUE MONTRÉAL

affiliée à l'Université de Montréal

Spherical Bragg Resonators for advanced electromagnetic emission engineering and lasing applications

YALINA GARCIA PUENTE

Département de génie physique

Thèse présentée en vue de l'obtention du diplôme de *Philosophiæ Doctor*

Génie physique

Août 2024

© Yalina Garcia Puente, 2024.

POLYTECHNIQUE MONTRÉAL

affiliée à l'Université de Montréal

Cette thèse intitulée :

Spherical Bragg Resonators for advanced electromagnetic emission engineering and lasing applications

présentée par **Yalina GARCIA PUENTE**

en vue de l'obtention du diplôme de *Philosophiæ Doctor*

a été dûment acceptée par le jury d'examen constitué de :

Stéphane KÉNA-COHEN, président

Raman KASHYAP, membre et directeur de recherche

Gunes KARABULUT KURT, membre

Pavel CHEBEN, membre externe

DEDICATION

To my parents

ACKNOWLEDGEMENTS

I first met Prof. Raman Kashyap in March 2017 at a conference in Havana, Cuba – the XIV Symposium and XII Congress of the Cuban Physics Society. Through the esteemed Emerging Leaders in the Americas Program (ELAP) scholarship, I got the opportunity to come to Montreal for the first time. This scholarship paved the way for an exciting new phase in my life – working alongside Prof. Kashyap and his team in the Fabula's lab. Professor Kashyap has had a profound impact on my professional growth. His motivation to explore and delve into cutting-edge research topics has challenged me more than once over the years. But, in turn, it has stimulated my scientific curiosity and critical thinking and reinforced my commitment to excellence. I am grateful for the opportunity to embark on this doctoral journey under his guidance.

A special shoutout goes to Antsar, an invaluable friend who has extended her work experience and motherly affection on a personal level since I arrived in the lab. I also want to give a big thanks to Jyothis. From day one, her enthusiasm made me feel welcome and supported me through the ups and downs of this journey. As well, I would like to express my appreciation to my colleagues at Fabulas: Amirhossein, Sébastien, Victor, Frédéric, Antoine, Pierre, Anthony, Yannick, Qingtao, Jacynthe, Foroogh, Ehsan, Mahshid, and Reyhane.

I also want to thank Professors Jean-Jacques Laurin and Baptiste Auguié for their essential contributions to my research. I'm grateful for the help of technicians: Jules Gauthier, Steve Dubé, Jean-Sébastien Décarie, Traian Antonescu, Maxime Thibault and Jean-Paul Lévesque. I appreciate their support, which was crucial for realizing the experimental results presented in this thesis.

I was able to achieve this milestone thanks to the constant support and encouragement of my beloved friends and family. A special thank you goes to my parents, Ruben García Díaz and Emma Rosa Puente Perez, for their love, support, and trust in my decisions. My deepest gratitude is reserved for my husband, Yoandris, whose invaluable support has been paramount through these challenging years.

RÉSUMÉ

Les résonateurs optiques et les microcavités dotés d'un facteur de qualité (Q) élevé et d'un petit volume modal V ont récemment suscité une attention considérable. Ces cavités permettent une interaction améliorée entre l'émetteur de lumière et le mode de cavité à Q élevé, entraînant des modifications notables dans le processus d'émission spontanée. Cela a notamment favorisé le développement de sources de photons uniques et de lasers sans seuil. L'obtention d'un Q élevé dans les microcavités est généralement réalisée par réflexion interne totale. Par exemple, la confinement par réflexion interne totale dans des microsphères de silice peut générer des modes de galerie de diffusion avec des facteurs de qualité pouvant atteindre 10^9. Cependant, la réflexion interne totale impose des contraintes sur la taille de telles cavités, les limitant généralement à quelques dizaines de microns ou plus. Par conséquent, la grande taille de la cavité réduit la force de couplage entre l'émetteur de lumière et le mode optique à Q élevé.

En revanche, l'utilisation de cavités de défaut dans des cristaux photoniques, basées sur des réflexions de Bragg, offre une solution à ce problème en créant des cavités à Q élevé de tailles plus petites. Les micropiliers semi-conducteurs représentent un exemple de cavités optiques confinées par Bragg, où la réflexion de Bragg confine la lumière dans une dimension, tandis que la réflexion interne totale accomplit la même chose dans les deux autres dimensions. Un autre exemple concerne les structures de défaut dans les cristaux photoniques bidimensionnels (2D), où l'effet de bande interdite photonique 2D est utilisé pour obtenir un confinement de Bragg dans le plan bidimensionnel, avec une réflexion interne totale qui confine les photons dans la troisième dimension.

En tenant compte de ces facteurs, un concept intéressant consiste à créer des résonateurs de Bragg sphériquement symétriques avec une géométrie de type oignon. Cette conception vise à obtenir un confinement de Bragg omnidirectionnel approprié de la lumière, combinant ainsi un facteur de qualité élevé avec une dimension spatiale de la cavité de quelques microns. Par conséquent, cela permet de modifier de manière significative le processus d'émission spontanée à l'intérieur de telles cavités. Une proposition préliminaire concerne une structure périodique dans des coordonnées sphériques, en utilisant une sphère multicouche. En veillant à ce que l'épaisseur optique des couches, alternant entre des indices de réfraction élevés et faibles, soit un quart de longueur d'onde,

les photons peuvent être confinés tridimensionnellement à l'intérieur de la sphère centrale. Cependant, il y a seulement un nombre limité de travaux publiés sur des études expérimentales explorant les performances de ces dispositifs, et les applications potentielles envisagées doivent encore être démontrées.

Cette recherche de doctorat se concentre sur la modélisation et l'optimisation de nouveaux systèmes basés sur les résonateurs de Bragg sphériques (SBR). La thèse comprend quatre articles qui explorent différents aspects des SBR et de leurs applications. Dans le premier article, des SBR de taille millimétrique fabriqués à l'aide de la technologie d'impression tridimensionnel (3D) sont étudiés expérimentalement et validés numériquement. L'étude analyse les dépendances fréquentielles des coefficients de réflexion et de transmission, et calcule les valeurs propres des fréquences pour examiner la densité des états photoniques dans ces SBR. L'influence de la position de la source sur l'énergie des ondes électromagnétiques du résonateur est également examinée. Nous démontrons que les SBR peuvent agir en tant que cavités omnidirectionnelles, modifiant la densité des états électromagnétiques par rapport à l'espace libre, ce qui permet d'amplifier ou d'inhiber les processus d'émission spontanée.

Le potentiel des SBR pour l'ingénierie de l'amplification optique et du gain de seuil dans les applications de laser est démontré de manière théorique dans le deuxième article. Une méthode récursive de matrice de transfert est utilisée pour étudier la diffusion dans un SBR dopé à l'Er^{3+}. Le facteur de gain de seuil pour le laser est déterminé en scannant les pôles et les zéros de la S-matrice dans le plan de fréquence complexe.

Une nouvelle approche visant à renforcer les champs magnétiques dans les nanoantennes tout-diélectrique en utilisant des SBR est présentée dans le troisième article. L'étude optimise la résonance du dipôle magnétique d'une nanoantenne sphérique à coque SiO_2/Si. Les taux de désintégration radiatifs et non radiatifs d'un émetteur Eu^{3+} sont étudiés, révélant que le couplage de résonance du dipôle magnétique de la nanoantenne avec le mode SBR améliore significativement le champ magnétique modal. Les résultats montrent un facteur de Purcell élevé d'environ $\sim 5 \times 10^3$, l'un des plus élevés signalés dans la littérature à notre connaissance.

Le quatrième article propose une nouvelle structure plasmonique de Tamm en couplant une structure de nanosphère métallique à coque Au/SiO_2 avec un SBR SiO_2/TiO_2. L'analyse théorique

montre une absorption maximale dans la région de l'interstice de bande du SBR, attribuée au couplage entre le plasmon polariton de Tamm (TPP) et les modes de défaut du SBR. Les résultats suggèrent le potentiel de génération de modes TPP à haute Q pour des applications telles que les commutateurs, les dispositifs de calcul logique optique et l'optique non linéaire. Ces articles contribuent collectivement à la compréhension et à l'utilisation des SBR, démontrant leurs capacités dans divers domaines, notamment la photonique, l'optoélectronique, l'information quantique et la plasmonique.

ABSTRACT

Optical resonators and microcavities with a high quality (Q) factor and a small modal volume V have recently garnered significant attention. These cavities enable enhanced interaction between the light emitter and the high Q cavity mode, leading to notable modifications in the spontaneous emission process. This, in turn, has facilitated the development of single photon sources and threshold-less lasers. The attainment of high Q in microcavities is commonly achieved through total internal reflection. For instance, confinement via total internal reflection in silica microspheres can generate whispering-gallery modes with quality factors as high as 10^9. However, total internal reflection imposes constraints on the size of such cavities, typically limiting them to tens of microns or larger. Consequently, the large size of the cavity diminishes the coupling between the light emitter and the high-Q optical mode.

On the other hand, using defect cavities in photonic crystals, based on Bragg reflections, offers a solution to this problem by creating high Q cavities with smaller sizes. Semiconductor micropillars represent an example of Bragg-confined optical cavities, where Bragg reflection confines light in one dimension, while total internal reflection accomplishes the same in the other two dimensions. Another example involves defect structures in two-dimensional (2D) photonic crystals, where the 2D photonic band gap effect is employed to obtain Bragg confinement in the 2D plane, with total internal reflection confining photons in the third dimension.

Considering these factors, an intriguing concept involves the creation of spherically symmetric Bragg resonators with an onion-like geometry. This design aims to achieve proper omnidirectional Bragg confinement of light, thereby combining a high Q factor with a cavity spatial dimension of a few microns. Consequently, it allows for significantly altering the spontaneous emission process within such cavities. A preliminary proposal involves a periodic structure in spherical coordinates, employing a multilayered sphere. By ensuring that the optical thickness of the layers, alternating between high and low refractive indices, is a quarter wavelength, photons can be confined three-dimensionally inside the core sphere. However, there are only a limited number of published works on experimental studies exploring the performance of these devices, and the envisioned potential applications still need to be demonstrated.

This Ph.D. research focuses on the modeling and optimization of novel Spherical Bragg Resonator (SBR)-based systems. The thesis comprises four articles that explore different aspects of SBRs and their applications.

In the first article, millimeter-sized SBRs fabricated using three-dimensional (3D) printing technology are experimentally investigated and numerically validated. The study analyzes the frequency dependencies of reflection and transmission coefficients while also determining eigenfrequency values to estimate the density of photonic states within these SBRs. Additionally, we evaluate the impact of the source position on the electromagnetic wave energy within the resonator. Our findings illustrate that SBRs have the capability to function as omnidirectional cavities, changing the density of electromagnetic states in contrast to free space. This, in turn, leads to the enhancement or suppression of spontaneous emission processes.

The potential of SBRs to engineer optical amplification and threshold gain for lasing applications is theoretically demonstrated in the second paper. A recursive transfer matrix method is employed to investigate the scattering in an Er^{3+} doped SBR. The determination of the threshold gain factor for lasing involves scanning the poles and zeros of the S-matrix within the complex frequency plane.

A novel approach to enhance magnetic fields in all-dielectric nanoantennas using SBRs is introduced in the third article. The study optimizes the magnetic dipole resonance of a SiO_2/Si core-shell spherical nanoantenna. The radiative and non-radiative decay rates of a Eu^{3+} emitter are investigated, revealing that the coupling between the magnetic dipole nanoantenna resonance and the SBR mode effectively amplifies the modal magnetic field. The findings demonstrate a high Purcell factor of $\sim 5 \times 10^3$, one of the highest reported in the literature to our knowledge.

The fourth article proposes a novel Tamm plasmon-like resonance supporting structure by coupling an Au/SiO_2 core-shell metal nanosphere structure with a SiO_2/TiO_2 SBR. The theoretical analysis shows a peak absorption in the SBR bandgap region, attributed to the coupling between the Tamm plasmon polariton (TPP) and defect modes in the SBR. The results suggest the potential of generating high-Q TPP modes for applications such as switches, optical logic computing devices, and nonlinear optics.

These articles collectively contribute to the understanding and utilization of SBRs, demonstrating their capabilities in various fields, including photonics, optoelectronics, quantum information, and plasmonics.

TABLE OF CONTENTS

DEDICATION III

ACKNOWLEDGEMENTS IV

RÉSUMÉ V

ABSTRACT VIII

TABLE OF CONTENTS XI

LIST OF FIGURES XV

LIST OF SYMBOLS AND ABBREVIATIONS XXII

LIST OF APPENDICES XXIII

CHAPTER 1. INTRODUCTION 1

1.1 Motivation and problem identification 4

1.2 Objectives 5

1.3 Organization of the thesis 6

CHAPTER 2. LITERATURE REVIEW 8

2.1 Spherical Bragg resonator 8

2.2 Modelling techniques 11

2.2.1 Recursive Transfer-Matrix method 12

2.3 Fabrication techniques 15

2.3.1 PECVD for SBRRs fabrication 16

2.4 Active nanophotonic applications 18

2.4.1 Spontaneous emission engineering 18

2.4.2 Loss compensation and amplification 22

2.4.3 Resonant scattering of dielectric nanosphere 25

2.4.4 Tamm plasmonic polaritons 30

CHAPTER 3. ARTICLE 1: EXPERIMENTAL CHARACTERIZATION OF SPHERICAL BRAGG RESONATORS FOR ELECTROMAGNETIC EMISSION ENGINEERING AT MICROWAVE FREQUENCIES 34

3.1 Introduction 34

3.2 Results and discussion 37

3.2.1 Reflectance spectra and local density of states 38

3.2.2 Geometrical and spatial dependence of the resonant modes 40

3.2.3 Theoretical and experimental scattering 44

3.3 Conclusions 46

3.4 Methods 46

3.4.1 SBR fabrication and experimental measurements 47

3.5 Funding 49

3.6 Acknowledgments 49

3.7 Author contributions 49

3.8 Disclosures 49

3.9 Data availability 49

3.10 Supplementary Information 50

CHAPTER 4. ARTICLE 2: SPHERICAL BRAGG RESONATORS FOR LASING APPLICATIONS: A THEORETICAL APPROACH 52

4.1 Introduction 52

4.2 Theory of light scattering 53

4.2.1 Decay rate 54

4.2.2 Scattering, absorption, and extinction efficiencies 55

4.2.3 Gain media and loss compensation 56

4.3 Results and discussion 57
4.3.1 Scattering efficiencies and modal analysis 59
4.3.2 Gain 61
4.3.3 Pole zero gain threshold 63
4.4 Conclusions 68
4.5 Funding, acknowledgments, and disclosures 68
4.5.1 Funding 68
4.5.2 Acknowledgments 69
4.5.3 Disclosures 69
4.5.4 Data availability 69
CHAPTER 5. ARTICLE 3: MAGNETIC PURCELL ENHANCEMENT IN A NANOANTENNA-SPHERICAL BRAGG RESONATOR COUPLED SYSTEM 70
5.1 Introduction 70
5.2 Methods 72
5.2.1 Magnetic field 73
5.2.2 Decay rate 73
5.3 Results and Discussion 74
5.3.1 Electromagnetic field enhancement and coupling 78
5.3.2 Decay rate enhancement and spatial dependence 80
5.4 Conclusions 83
5.5 Funding, acknowledgments, and disclosures 84
5.5.1 Funding 84
5.5.2 Acknowledgments 84
5.5.3 Disclosures 84

5.5.4 Data availability 84

CHAPTER 6. ARTICLE 4: HIGH-Q TAMM PLASMON-LIKE RESONANCE IN SPHERICAL BRAGG MICROCAVITY RESONATORS 85

6.1 Introduction 85

6.2 Theory of light scattering by multilayered spherical plasmonic nanoparticles 87

6.3 Results and discussion 90

6.4 Conclusion 100

6.5 Funding, acknowledgments, and disclosures 100

6.5.1 Funding 100

6.5.2 Acknowledgments 101

6.5.3 Disclosures 101

6.5.4 Data availability 101

CHAPTER 7. GENERAL DISCUSSION 102

7.1 Characterization of Spherical Bragg Resonators 102

7.2 Spherical Bragg Resonator for lasing 103

7.3 Nanoantenna-Spherical Bragg Resonator coupled system 104

7.4 Tamm plasmonic Spherical Bragg Resonator 106

CHAPTER 8. CONCLUSION AND RECOMMENDATIONS 108

REFERENCES 111

APPENDICES 129

LIST OF FIGURES

Figure 1-1 Photonic crystals in (a) one, (b) two, and (c) three dimensions. The periodicity Λ of the different dielectric constants along one or more axes is represented by green nL and grey nH regions in the diagram. 1

Figure 1-2 Photonic crystals structures (a) hollow disk, (b) hollow optical fiber, and (c) spherical Bragg resonator. Figure adapted with permission from [20, 21]. 3

Figure 2-1 (a) Schematic representation of a SBR excited by a plane wave. (b) Cross section of a SBR where nj represents the refractive index, rj is the radius of the shells and $t_{H,L,}$ is the optical thickness of the alternating high nH and low refractive indices nL layers. The homogenous and isotropic host medium refractive index is denoted by $nJ + 1$. 9

Figure 2-2 Spatial distribution of the normalized electromagnetic field in a 6-layer spherical Bragg resonator. (a) Total electric field $E2E02$ and (b) total magnetic field $H2H02$ on the (x, y) plane for l=1 at a wavelength of $\lambda \approx 1536\, nm$. (c) Total electric field $E2E02$ and (d) total magnetic field $H2H02$ on the (y, z) plane for l=5 at a wavelength of $\lambda \approx 1872\, nm$. 10

Figure 2-3 Reflectivity R of a Spherical Bragg Resonator with 24 layers. Figure taken with permission from [28]. (b) Corresponding normalized intensity profile H_ϕ field component, calculated using Spherical space Bessel-Legendre-Fourier (BLF) at the eigenfrequency $f = 188\, THz$. Figure taken with permission from [34]. 12

Figure 2-4 Schematic representation of the expansion coefficients ApL and BpL estimation by matching the fields across the adjacent shell interfaces j and $j + 1$. 13

Figure 2-5 Diagram illustrating a reactor chamber with a microsphere: (1) glass microsphere, (2) quartz fibre, (3) circular quartz substrate, (4) layer deposited on microsphere, (5) layer deposited on substrate, (6) plasma discharge, and (7) electrodes. Figure taken with permission from [41]. 16

Figure 2-6 (a) Structure of the SBRR: (1) glass microsphere and (2) quartz fibre. (b) Reflection spectra collected at points I, II, III and normalized with respect to the maximum reflection coefficient. Figure taken with permission from [41]. 17

Figure 2-7 (a) Representation of the electric dipolar (ED) and magnetic dipolar (MD) resonant modes induced in a high refractive index dielectric sphere by a plane wave excitation. The ED mode arises from the collective polarization of the nanoantenna material, leading to the generation of a magnetic current loop. On the other hand, the MD mode originates from an electric displacement current loop, resulting in the creation of a magnetic dipole moment. (b) contributions of the electric dipole (ED), magnetic dipole (MD), and magnetic quadrupole (MQ) resonances to the total scattering from a $260\ nm$ Si sphere. 27

Figure 2-8 Total scattering efficiency as a function of incident plane wave wavelength and radius of a Si nanosphere. 28

Figure 2-9 (a) Schematic representation of surface plasmon resonance in plasmonic nanoparticles. (b) Extinction spectra of gold nanoparticles of different sizes.....31

Figure 3-1 (a) Schematic of a Spherical Bragg Resonator excited by a plane wave. (b) Cross section of a Spherical Bragg Resonator ri represents the radius of the spheroid and Λj is some design factor.....37

Figure 3-2 (a) Experimental and calculated reflectance spectrum at the center of an SBR with $nl = 10$ plotted in solid red and black dotted lines, respectively. Experimental transmitted power measured near the SBR surface was plotted in a solid blue line. All spectra are normalized to the maximum reflection coefficient. The SBR band gap's center is fixed at $fB = 11\ GHz,$ and the core radius is $rcore = \lambda B4nair$. (b) Calculated poles and zeros of the SBR scattering matrix for two different core radii $rcore = \lambda B2nair$ and $rcore = \lambda B4nair$ represented as square and diamond symbols, respectively. The pole-zero map frequencies are normalized by $f0\ = 1\ GHz.$.....41

Figure 3-3 (a) Spatial distribution of the normalized electric field intensities of a 10-layer SBR with $rcore = \lambda B2nair$ as a function of the frequency. (b) Calculated total, perpendicular, and parallel decay rate components of a dipole at $f \approx 9.55\ GHz$, circular symbol, and $f \approx 11.35\ GHz$ triangular symbol as a function of the position along the SBR core. (c) Reflectance measurement at different points along the SBR core radius. (d) Reflectance measured at $f \approx 9.55\ GHz$ and $f \approx 11.35\ GHz$ at different points of the SBR core.....43

Figure 3-4 (a) Calculated total scattering efficiencies Qsca for a 10-layer SBR up to order twelve of the multipole electric and magnetic contributions. (b) Spatial distribution of the normalized electric field intensities of a 10-layer SBR with $rcore = \lambda B4nair$ as a function of the frequency, the PLA layers are represented by white lines. (c) Scattering measurements of a 10-layer SBR for the S and P polarization.....45

Figure 3-5 (a) SBR fabrication by 3D printing in PLA. Different sizes of 3D-printed. (b) Scattering and (c) reflectance measurement setup. 48

Figure 3-6 Calculated maps of the Spl matrix component in the complex frequency plane for (a) TE1, (b) TM1, (c) TE2 and (d) TM2 in 10-layer SBR air-PLA with a Bragg frequency of 10 GHz and a core radius of $rcore = \lambda B2nair$.....50

Figure 3-7 Spatial distribution of the normalized magnetic field intensities of a 10-layer SBR with (a) $rcore = \lambda B2nair$ and (b) $rcore = \lambda B4nair$ as a function of the frequency, the PLA layers are represented by white lines.....51

Figure 3-8 Measured $S11$ parameters of SBRs with a different number of layers, (a) $nl = 10$ and (d) $nl = 6$, at the core of the structure. 51

Figure 4-1 Schematic of an Er^{3+} core-doped Spherical Bragg Resonator with Si/SiO_2 multilayers. 54

Figure 4-2 Calculated (a) Purcell factor, (b) quality factor and (c) modal volume for a spherical Bragg resonators with a different number of layers at the resonant wavelength $\lambda \approx 1536\, nm$. 58

Figure 4-3 Scattering efficiencies for a 12-layer spherical Bragg resonator for five multipoles (a) electric, (b) magnetic and (c) total modes. 60

Figure 4-4 Spatial distribution of the normalized magnitude for (a) total electric field $E2E02$ and (b) total magnetic field $H2H02$ on the (x, y) plane for l=1 at $\lambda \approx 1536\, nm$ and (c) total electric field $E2E02$ and (d) total magnetic field $H2H02$ on the (y, z) plane for l=5 at $\lambda \approx 1794\, nm$ for a 12-layer spherical Bragg resonator. 61

Figure 4-5 (a) Scattering, (c) extinction and (d) absorption efficiency dependency on gain factor for a 12-layer Er^{3+} core-doped Spherical Bragg Resonator. (b) FWHM (red square) and maximum scattering efficiency (black circles) dependency on gain factor. 63

Figure 4-6 Scattering efficiencies of 12-layer Spherical Bragg Resonator for TE1 (a) and TM1 (b). Maps of the Spl matrix component in the complex frequency plane for TE1 (c) and TM1 (d). 64

Figure 4-7 (a) Maps of the Spl matrix component in the complex frequency plane for TE1 in a 12-layer Er^{3+} core-doped Spherical Bragg Resonator. (b) Pole (blue) and zeros (orange) analysis of S-matrix scattering dependency on gain factor, gamma. 65

Figure 4-8 Gain threshold and Er^{3+} core-doped concentration for lasing in a Spherical Bragg Resonator as a function of the number of layers. 66

Figure 5-1 (a) Cross section of a SiO_2/Si core-shell spherical nanoantenna of total radius R and inner radius ri excited by a plane wave. (b) Schematic representation of the electric dipolar (ED) and magnetic dipolar (MD) modes induced by the plane wave excitation. The ED mode results from the communal polarization of the nanoantenna material, which induces a magnetic current loop. The MD mode results from of an electric displacement current loop that generates a magnetic dipole moment. 72

Figure 5-2 (a) Total scattering efficiency as a function of the radius of a Si nanosphere and the wavelength of the incident plane wave. (b) Contribution to the total scattering of a $208\ nm$ Si sphere from the electric dipole (ED), magnetic dipole (MD), and magnetic quadrupole (MQ) resonances, indicated as white vertical dashed line in (a). (c) Illustration of the evolution of a Si sphere of diameter $D = 144\ nm$ into a SiO_2/Si core-shell spherical nanoantenna of inner radius ri varying from $0\ nm$ to $90\ nm$. (d) Calculated total scattering efficiency of the SiO_2/Si core-shell spherical nanoantenna of diameter $D = 144\ nm$ as a function of wavelength and inner radius, the star indicates an MD resonance at $\lambda \approx 590\ nm$. 76

Figure 5-3 (a) Scattering efficiencies (*Qsca*) and absorption efficiencies (*Qabs*) of a SiO_2/Si core-shell nanosphere-antenna of radius $R = 72\ nm$ and inner radius $ri = 27\ nm$. The inset figures illustrate the spatial distribution of the normalized magnitude for total electric field

$E2E02$ at the ED resonance $\lambda \approx 455\,nm$ and total magnetic field $H2H02$ at the MD resonance $\lambda \approx 590\,nm$ on the (x, y) plane. (b) Radiative decay rate (pink line) and non-radiative decay rate (dashed cyan line) for an emitting MD located at the center of the SiO_2/Si core-shell nanosphere-antenna. Quantum efficiency for a magnetic dipolar emitter with 100% intrinsic quantum efficiency (yellow line). 77

Figure 5-4 (a) Schematic of a SiO_2/Si nanoantenna-SBR coupled system. (b) Scattering efficiencies of a 2-, 4- and 6-layer spherical Bragg resonator for five electric and magnetic multipole modes. TM1 represents the magnetic resonant dipole mode, and the higher-order modes are labeled TM2, TM3, and TM4. (c) Calculated quality factor for a spherical Bragg resonator with different number of layers, n_l, at magnetic dipole resonance wavelength $\lambda \approx 590\,nm$. (d) Normalized magnitude of the total magnetic field $H2H02$ of a 4-layer SiO_2/Si nanoantenna-SBR coupled system in the (x, y), (x, z) and (z, y) planes at $\lambda \approx 590\,nm$. The white circles represent the SiO_2/Si layers boundary. 79

Figure 5-5 (a) Purcell enhancement of a magnetic dipole emitter in the center of a SiO_2/Si nanoantenna-SBR with a different number of layers coupled system at $\lambda \approx 590\,nm$ with core refractive index $ncore = 1.95$ and $ncore = 1.45$. (b) Decay rate enhancement as a function of the number of layers of a SiO_2/Si spherical Bragg resonator and the wavelength of the MD emitter.....81

Figure 5-6 (a) Radiative decay rate enhancement of a 4-layer SiO_2/Si spherical Bragg resonator as a function of wavelength. (b) Perpendicular component, parallel component, and total decay rate at $\lambda \approx 590\,nm$ with respect to the x position of the MD emitter along the x-axis. The center of the SBR is set at $x = 0$.....82

Figure 6-1 (a) Calculated Au/SiO_2 core-shell nanosphere absorbance with spacer cavity shell thickness $tcavity = 239\,nm$ and different Au radius $rcore$. (Inserted) Schematic view of the Au/SiO_2 core-shell nanosphere. Normalized electric field intensity $E2E02$ in (b) with $\lambda \approx 535\,nm$ and (c) $\lambda \approx 950\,nm$. 88

Figure 6-2 (a) Schematic view of the proposed Tamm plasmon-like resonance supporting structure, composed of a TiO_2/SiO_2 SBR with an Au/SiO_2 core-shell metal nanosphere structure in the core. (b) Calculated absorbance of the Tamm plasmon-like resonance supporting structure of

Au radius $rcore = 20\,nm$, spacer cavity shell thickness $tcavity = 239\,nm$, and Bragg wavelength $\lambda B \approx 950\,nm$ excited by a plane wave varying the number of the SBR layers from 10 to 30. (c) Wavelength dependence of the maximum absorption with the number of SBR layers. 91

Figure 6-3 Maps of the Spl matrix component of order $l = 1$ and $l = 2$ in the complex frequency plane for TE (a,b) and TM (c,d) polarization. The Tamm plasmon-like resonance supporting structure comprises an Au core with radius $rcore = 20\,nm$ and a SiO_2 spacer cavity shell thickness $tcavity = 239\,nm$, surrounded by a 30-layer TiO_2/SiO_2 SBR with Bragg wavelength $\lambda B \approx 950\,nm$. The circumferences signal the structure's two lowest-order modes, TE1 and TM2. 93

Figure 6-4 Radiative decay rate enhancement of an electric dipole placed in the cavity (spacer) shell of the 30-layer TiO_2/SiO_2 SBR at $r = 22\,nm$ from the surface of the Au core nanosphere. (a) Perpendicular and parallel components of the radiative and nonradiative decay rates up to other $l = 5$ and $l = 20$ are plotted as solid and dotted lines, respectively. (b) Dipolar $l = 1$ and (c) quadrupolar $l = 2$ contribution to perpendicular and parallel components of the radiative decay rate enhancement. 94

Figure 6-5 (a) Perpendicular, parallel, and total radiative and nonradiative decay rate enhancement dependency on the dipole distance from the Au nanosphere surface r at $\lambda \approx 930\,nm$. (b) Radiative decay rate enhancement of an electric dipole in the spacer shell of the metal-SBR structure at $r = 60\,nm$ from the surface of the Au nanosphere. 95

Figure 6-6 (a) Decay rate enhancement as a function of the number of layers of the TiO_2/SiO_2 SBR with Au radius core $rcore = 20\,nm$, spacer cavity shell thickness $tcavity = 239\,nm$, and Bragg wavelength $\lambda B \approx 950\,nm$. The dipolar electric and magnetic resonances are labeled by TE1 and TM1, respectively. (b) Calculated quality factor for a spherical Bragg resonator with a different number of layers at TE1 $\approx 913\,nm$. 96

Figure 6-7 (a) The calculated absorbance of the metal-SBR structure with an Au radius $rcore = 20\,nm$, $N = 30$, and Bragg wavelength $\lambda B \approx 950\,nm$, varying the spacer cavity shell thickness from $tcavity = 289\,nm$ to $tcavity = 339\,nm$ and (b) for different Bragg wavelengths λB and spacer cavity shell thickness $tcavity = 239\,nm$. 97

Figure 6-8 Calculated electric field intensity distribution of the metal-SBR structure with an Au radius $rcore = 20\,nm$, $N = 30$, Bragg wavelength $\lambda B \approx 950\,nm$, and spacer cavity shell thickness $tcavity = 239\,nm$ at $\lambda = 911\,nm$. Inserted figure: Zoom around the Au nanoparticle, the vertical dotted lines denote the layers interface.....99

LIST OF SYMBOLS AND ABBREVIATIONS

SBR	Spherical Bragg Resonator
2D	two-dimensional
3D	three-dimensional
PBG	Photonic band gap
TPP	Tamm plasmonic polariton
PWEM	Plane wave expansion method
FDTD	Finite difference time domain
FEM	Finite element method
PECV	Plasma-enhanced chemical vapor deposition
RF-PECV	Radiofrequency plasma-enhanced chemical vapor deposition
PC	Photonic crystal
MNP	Metal nanoparticles
LDOS	Local density of states
QDs	Quantum dots
SPR	Surface plasmon resonances
LSP	Localized surface plasmon
SPR	Surface plasmon resonances
DBR	Distributed Bragg reflectors
FWHM	Full width half maximum
NIR	Near-infrared
SPR	Surface plasmon resonance

LIST OF APPENDICES

Appendix A LIST OF PUBLICATION 129

CHAPTER 1. INTRODUCTION

In materials science, a crystalline solid is characterized by the periodic arrangement of atoms or molecules. This regular atomic arrangement gives rise to a periodic potential profile that dictates the behavior of electrons within the material. In the context of semiconductors, this atomic arrangement plays a crucial role in defining the energy bands accessible to electrons, resulting in a distinct separation between the conduction and valence bands known as the band gap [1].

Likewise, in the field of optics, the concept of a photonic crystal emerges by introducing periodicity in either the refractive index or the dielectric function of a material. In the late 1980s, E. Yablonovitch showed that it was possible to open a band gap for photons by alternating different dielectric materials periodically, which marked the emergence of the photonic crystal concept [2]. Additionally, S. John's interest in Anderson's localization contributed to the realization of two-dimensional photonic crystals in the mid-1990s, resulting in a flourishing field of research. Similar to how the atomic arrangement influences the electronic band structure in crystals, the periodic refractive index or dielectric function in a photonic crystal governs light propagation, resulting in a range of allowed and forbidden optical modes [3]. Figure 1-1 showcases examples of one-dimensional (1D), two-dimensional (2D), and three-dimensional (3D) photonic crystals. A photonic crystal is considered to have a complete gap in the photonic band if it can effectively inhibit the propagation of electromagnetic waves, regardless of polarization, direction, or source [4].

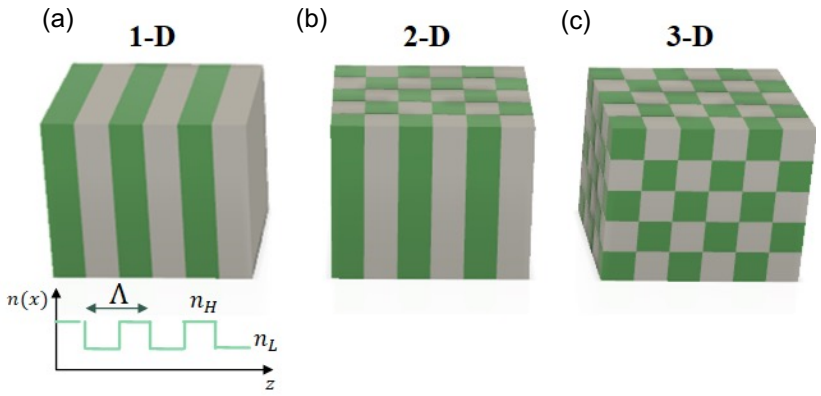

Figure 1-1 Photonic crystals in (a) one, (b) two, and (c) three dimensions. The periodicity Λ of the different dielectric constants along one or more axes is represented by green n_L and grey n_H regions in the diagram.

By harnessing the unique properties of photonic crystals, it is possible to manipulate and control the flow of light, enabling a broad range of applications such as waveguiding, optical filtering and light confinement [4, 5]. The systematic introduction of periodicity in the refractive index or dielectric function provides a powerful tool for tailoring and engineering light-matter interactions at the nanoscale, offering exciting prospects for developing novel photonic devices and technologies [6].

Introducing defects in the periodic structure of photonic crystals has significantly expanded their design criteria and applications. For instance, a single cell removal, also known as a *"point defect"*, can create a photonic nano-cavity that can trap electromagnetic radiation. Similarly, removing a column of unit cells in the crystal, known as a *"line defect"*, can create a waveguide that enables the transmission of electromagnetic radiation only along the defect line. The combination of these *"line defects"* and *"point defects"* has led to developing photonic crystals for applications from integrated lasers to information processing and sensing in Lab-on-a-Chip systems [7-9].

In recent years, there has been a surge of interest in exploring photonic structures that exhibit three-dimensional band gaps [2, 3]. The quest for achieving a photonic band gap in three dimensions began with Yablonovitch's proposal of a 3D array of spherical holes embedded within a dielectric material [2]. Despite the resonant nature of these spherical cavities, they fell short of demonstrating a band gap as initially envisioned [2]. Furthermore, a three-dimensional photonic band gap was realized by developing a theoretical framework [10] that aligned with experimental findings [11]. However, it required the fabrication of complex and specialized structures. This breakthrough has spurred an astonishing array of novel photonic structures, creating innovative optical fibers such as two-dimensional photonic crystal fibers [12, 13] and three-dimensional periodic structures like opals [10].

Researchers have explored diverse approaches, including wood-pile structures [14] and the engineering of complex artificial "crystalline" materials [15], to mimic and extend the capabilities of these photonic structures. Hollow-core photonic crystal fibers, mainly, have garnered extensive attention [16], demonstrating their potential for various applications. Furthermore, high-contrast optical fibers with onion-like structures have shown promise in efficiently transmitting high-power 10-micron radiation [17].

Significant progress has been made in developing photonic structures with unconventional geometries in recent years, Figure 1-2 (a) and (b). One example is the proposal of periodic concentric cylinders with a common axis in free space. This creates a two-dimensional (x, y) crystalline structure with propagation direction invariance along the z-axis. This unique structure, known as a leaky mode structure, has attracted considerable attention [18]. In addition to the leaky mode structure, the cylindrical geometry has also been explored for designing "onion skin" concentric cylindrical waveguides, which exhibit transverse resonant confinement and enable efficient mode propagation along the waveguide axis [19]. However, it is essential to note that all three-dimensional structures, including the aforementioned cylindrical configurations, possess a limitation arising from their periodicity defined in Cartesian coordinates (x, y, z).

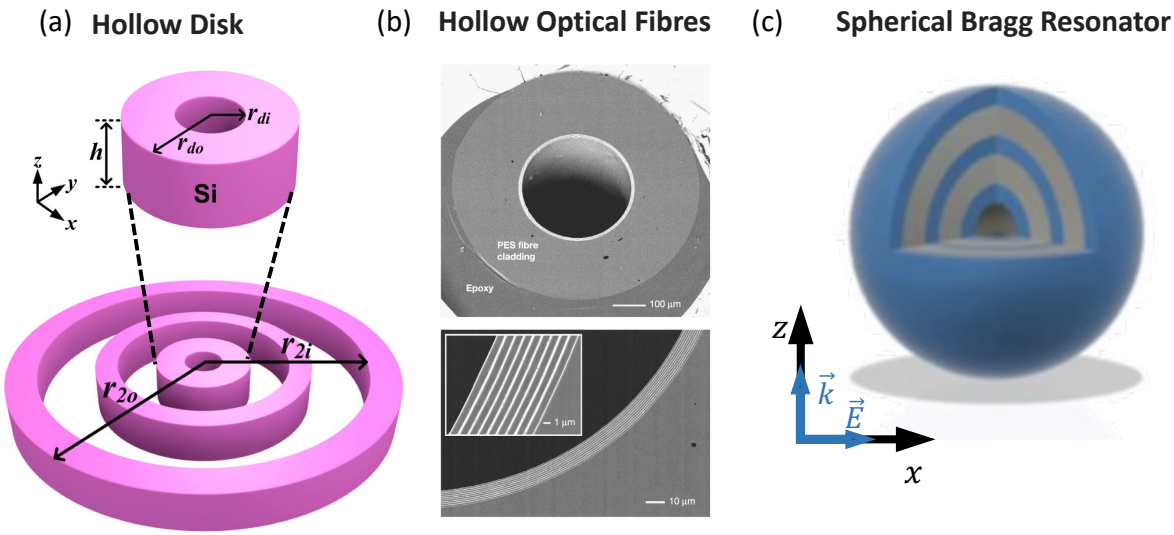

Figure 1-2 Photonic crystals structures (a) hollow disk, (b) hollow optical fiber, and (c) spherical Bragg resonator. Figure adapted with permission from [20, 21].

A fascinating class of three-dimensional photonic crystals is the radially periodic structure in spherical coordinates, where spheres with a common center location are arranged, Figure 1-2 (c). These structures, known as multilayered spheres, offer unique optical properties and have shown great potential in various applications [22]. In a multilayered sphere, alternating layers with high and low refractive indices are precisely designed with an optical thickness equal to a quarter wavelength. This specific arrangement can enable the confinement of photons within the core sphere in a three-dimensional manner, forming a Spherical Bragg Resonator (SBR) [23, 24]. The

study and utilization of SBRs represent a rapidly evolving field of research that continues to unveil new possibilities for photonics and optoelectronic applications. These advancements hold great potential in integrated photonics, quantum optics, optical computing, and biosensing. The main objective of this thesis is to explore various design and material systems further to enhance the performance and functionalities of SBR-based devices.

1.1 Motivation and problem identification

Spherical Bragg reflectors have emerged as a promising candidate for creating photonic microcavities. The use of alternating low- and high-refractive-index material concentric shells in a spherical Bragg reflector ensures perfect rotational symmetry in three dimensions, resulting in strong confinement of light in all directions and a photonic band gap (PBG) irrespective of the direction of light propagation [23, 24]. The ability to create a perfect omnidirectional PBG, combined with strong confinement of light, makes Spherical Bragg Resonators an attractive option for developing high-quality factor microcavities [23, 24].

Despite the success of lithography in creating 2D photonic crystals and resonator structures, manufacturing 3D solid-state microcavities using this technique remains challenging [25-27]. Researchers have attempted to overcome this limitation by utilizing chemical synthesis and a combination of etching and chemical vapor deposition. Nonetheless, the absence of a dependable fabrication method has constrained the comprehensive experimental investigation of spherical Bragg resonators (SBRs) and hindered the comprehension of their optical properties and potential applications in emerging technologies.

Spherical Bragg reflectors have garnered considerable attention from various researchers due to their immense potential in a wide range of applications. Specifically, they have been proposed as promising candidates for optical sensing, optical communication, and nanoscale laser technology. However, a significant challenge persists in the lack of reliable studies that elucidate the optimal conditions for leveraging their unique properties in areas such as lasing and amplification, modification of decay rates, and even enhancing the performance of plasmonic structures. This gap in knowledge hinders a comprehensive understanding of the potential applications and limits the practical implementation of spherical Bragg reflectors in these critical areas.

This Ph.D. research aims to investigate and characterize Spherical Bragg Resonators (SBRs) comprehensively. The primary focus will be modeling and optimizing novel SBR-based systems to control dipolar electric and magnetic emitters' decay rates effectively. In addition, this research will provide valuable insights into the design and performance of SBR structures, ultimately contributing to advancements in on-chip resonators, magneto-optical polarization conversion, and other potential applications.

1.2 Objectives

Considering the abovementioned challenges, we have established four objectives for the described Ph.D., outlined below.

1. Designing and fabricating Spherical Bragg Resonators (SBRs) using 3D printing technology.

The first objective of this Thesis is to employ 3D printing technology in the production of SBRs for both experimental exploration and numerical validation of their performance. The use of 3D printing to fabricate SBRs presents a versatile and readily available approach, enhancing the range of applications of these resonators in practical devices.

2. Demonstrate optical amplification and lasing for Er^{3+}-doped Si/SiO_2 SBRs.

SBRs featuring omnidirectional bandgaps exhibit resonant modes characterized by high-quality factor values and minimal modal volume. This objective aims to demonstrate the potential for optical amplification and the attainment of threshold gain for lasing in SBRs by engineering the Er^{3+} ion concentration and the structure modes.

3. Design and optimize SBR to enhance magnetic fields in spherical all-dielectric nanoantennas, boosting quantum emitters magnetic transitions.

All-dielectric Si nanoantenna has previously demonstrated electric and magnetic resonances, offering unique possibilities for manipulating light at the nanoscale. This objective focuses on engineering magnetic dipole nanoantenna resonance coupling with the SBR defect mode to enhance the modal magnetic field.

4. Design and demonstrate a novel Tamm plasmon-like resonance supporting structure by coupling an Au/SiO_2 core-shell metal nanosphere structure with a SiO_2/TiO_2 SBR.

The metal films in Tamm structures suffer from optical losses, which negatively impact the resonance Q-factor. This objective investigates the near-infrared scattering properties of the SBR Tamm plasmon-like system and provide a promising approach for generating high-Q Tamm plasmonic polariton (TPP) like modes.

1.3 Organization of the thesis

This thesis is composed of eight chapters. The first chapter serves as an extensive literature review focusing on Spherical Bragg Resonators (SBRs). It begins by providing a comprehensive analysis of the theoretical bases of SBRs, with particular emphasis on the transfer matrix method, which forms the basis of the research conducted in this thesis. Various fabrication methods proposed for SBRs are also discussed in detail. Subsequently, the chapter delves into a detailed overview of the key subjects investigated during the research. Specifically, it highlights the applications where SBRs exhibit the potential to enhance existing functionalities or introduce novel capabilities.

After that, the thesis presents four articles, each focusing on one of the four objectives outlined in the thesis. These articles provide in-depth analysis and investigations into specific Spherical Bragg Resonators (SBRs) aspects, including their design, fabrication, characterization, and applications.

Article 1 focuses on the experimental exploration and numerical validation of Spherical Bragg Resonators (SBRs) produced through 3D printing technology. The paper examines the dependence of reflection and transmission coefficients, analyzes the density of photonic states within the SBRs through eigenfrequency calculations, and investigates the impact of source position on electromagnetic wave energy within the resonator. It also explores the scattering efficiencies of multipole electric and magnetic contributions in a 10-layer SBR and compares them with scattering measurements for different polarizations.

Article 2 presents a theoretical investigation of Si/SiO_2 Spherical Bragg Resonators (SBRs) with varying numbers of layers. The research extensively examines the impact of modifying the Er^{3+} ion concentration, serving as a gain media in the SBR core. By establishing the relationship between the Er^{3+} ion concentration and the structure modes, the article demonstrates the

possibilities for engineering optical amplification and achieving threshold gain for lasing within SBRs.

Article 3 proposes the utilization of Spherical Bragg Resonators (SBR) to enhance magnetic fields in all-dielectric nanoantennas. The modal magnetic field is significantly enhanced by coupling the magnetic dipole resonance with the SBR defect mode. A demonstration of the potential of SBRs to significantly improve the performance of Si/SiO_2 core-shell nanoantennas is present.

Article 4 proposes a novel Tamm plasmon-like resonance supporting structure combining an Au/SiO_2 core-shell metal nanosphere with a SiO_2/TiO_2 SBR. The study focuses on the near-infrared scattering properties of the SBR Tamm plasmon system. Also, an analysis of the influence of the number of SBR layers, Bragg wavelength, and defect cavity layer thickness in the TPP modes is presented.

After the presentation of the four papers, a comprehensive discussion will be conducted to encompass this thesis's overall findings and contributions. At last, a concluding chapter will provide a concise summary of the thesis.

CHAPTER 2. LITERATURE REVIEW

This chapter provides an extensive literature review on Spherical Bragg Resonators (SBR). It begins by providing an in-depth analysis of the theory behind SBRs, emphasizing the transfer matrix method, which is the fundamental method employed throughout this thesis. In addition, the various SBR fabrication methods proposed are discussed. Then, the last section leads into an in-detail overview of the more important subjects investigated during my research. This section highlights those applications where SBRs have the potential to improve existing functionalities or introduce novel capabilities.

2.1 Spherical Bragg resonator

A spherical Bragg resonator is a photonic structure composed of J concentric spherical shells with alternating high n_H and low refractive indices n_L, as illustrated in Figure 2-1. These shells have an optical thickness, $t_{H,L,}$ of about one-quarter wavelength (Equation 2-1) that generate constructive interference among waves reflected from the interfaces [28, 29]. Due to the radial symmetry of the SBR, an omnidirectional band gap is formed. The band gap is the range of frequencies where the resonator inhibits outward propagation of electromagnetic waves. The wavelength, λ_B, at which the SBR behaves as an omnidirectional Bragg reflector is known as the center of the bandgap and is determined by the thickness, $t_{H,L}$.

$$r_{j+1} - r_j = t_{H,L} = \frac{\lambda_B}{4n_{H,L}}. \qquad 2\text{-}1$$

The innermost shell represents the sphere's core and is the first shell, $j = 1$. In contrast, the outermost shell is the host medium, represented by the $(j + 1)$-th shell. The outer radius of the j-th shell is indicated by r_j. Each j shell is assumed to be homogeneous and isotropic, with scalar permittivity ε_j and permeability μ_j. The refractive index of each shell is determined by the square root of the ratio of its permittivity and permeability, denoted by $n_j = \sqrt{\varepsilon_j \mu_j}$.

In this Thesis we assume that the SBR is subjected to a harmonic electromagnetic plane wave, with a vacuum wavelength of λ, the corresponding wave vector in the j-th shell is calculated as $k_j = n_j\omega/c = 2\pi n_j/\lambda$, where c represents the speed of light in vacuum, and ω denotes the frequency of the electromagnetic wave.

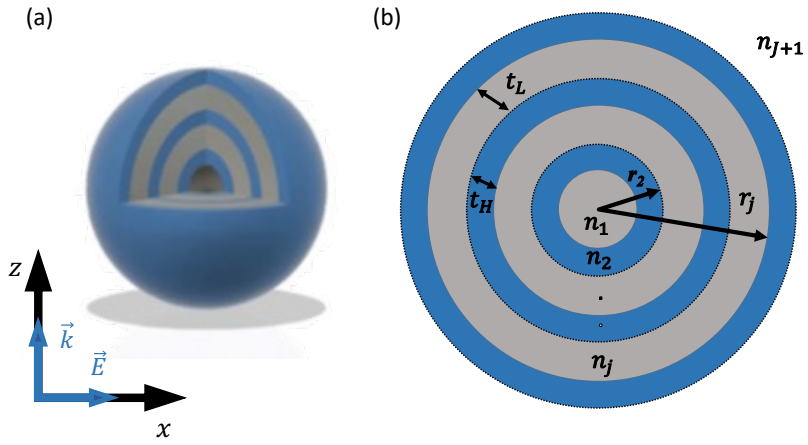

Figure 2-1 (a) Schematic representation of a SBR excited by a plane wave. (b) Cross section of a SBR where n_j represents the refractive index, r_j is the radius of the shells and $t_{H,L,}$ is the optical thickness of the alternating high n_H and low refractive indices n_L layers. The homogenous and isotropic host medium refractive index is denoted by n_{J+1}.

Using spherical coordinates, the solution to the Maxwell equations can be express for the j-th concentric dielectric layer as a combination of various multipole components, each distinguished by their angular quantum numbers l and m. Particularly, each transverse electric (TE) and transverse magnetic (TM) polarization component, p of the electric field, can be represented as a sum of spherical harmonics multiplied by corresponding coefficients, as outlined in [30]:

$$\vec{E}(j,\vec{r}) = \sum_{pL}\left[A_{pL}(j)\vec{F}_{pL}(k_j,\vec{r}) + B_{pL}(j)\vec{G}_{pL}(k_j,\vec{r})\right] \quad 2\text{-}2$$

here the orbital, l, and magnetic angular momenta, m, are represented by $L = l, m$. The expansion coefficients are $A_{pL}(j)$ and $B_{pL}(j)$. In addition, $\vec{F}_{pL}(k_j,\vec{r})$ and $\vec{G}_{pL}(k_j,\vec{r})$ represent the vector multipoles [30, 31]. The expansion coefficients $A_{pL}(j)$ and $B_{pL}(j)$ can be determined using a recursive algorithm by equating the tangential components of the electromagnetic field at each boundary of the respective layers [31, 32]. As will be described in Section 2.2.1. This multipole expansion allows for a comprehensive analysis of the resonant modes exhibited by the SBR, as well as their interaction with the surrounding host medium. The modes can be classified into two distinct types: core modes and cladding modes.

The core modes, like Fabry-Perot modes, have relatively small angular quantum numbers l (as defined by Equation 2-3) and are confined within the core of the resonator. In contrast, the cladding

modes resemble whispering gallery modes in ring resonators and possess larger angular quantum numbers $l \approx n_{eff}L/\lambda$, where n_{eff} is the effective refractive index and L is the round trip length [33]. These modes are distributed across the dielectric shells and are strongly affected by the thickness and refractive indices of the layers.

$$l \leq \frac{2\pi n_{core} r_{core}}{\lambda} \qquad 2\text{-}3$$

As example, Figure 2-2 illustrates the spatial distribution of the normalized magnitude of the total electric field $|E|^2/|E_0|^2$ and the total magnetic field $|H|^2/|H_0|^2$ in a 6-layer SiO_2/TiO_2 SBR at two different wavelengths. It can be observed that the field distribution of the core mode ($l = 1$, dipolar mode) TE1-TM1 is predominantly confined within the core of the SBR. On the other hand, the electromagnetic fields associated with the cladding mode ($l = 5$) TE5-TM5 are spread across the cladding layers.

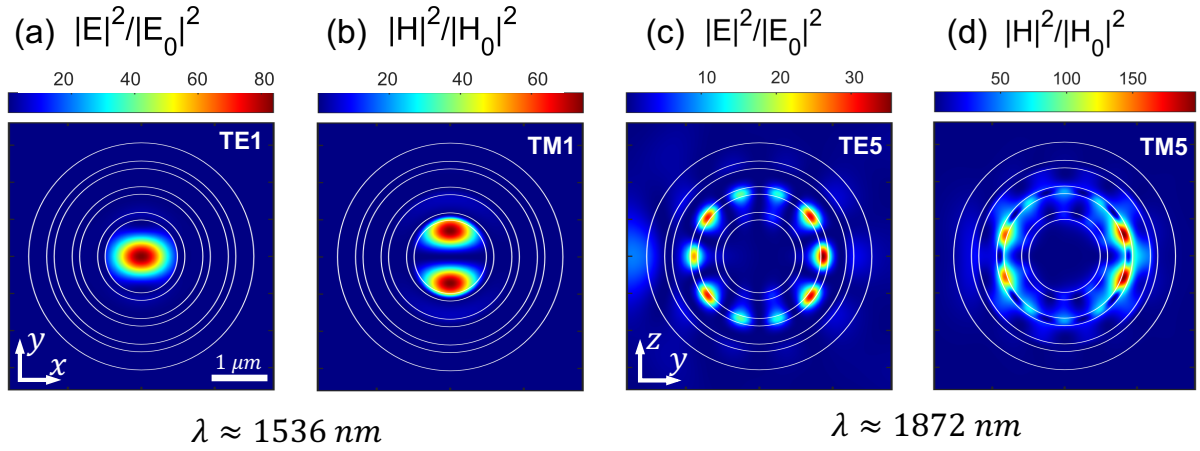

Figure 2-2 Spatial distribution of the normalized electromagnetic field in a 6-layer spherical Bragg resonator. (a) Total electric field $|E|^2/|E_0|^2$ and (b) total magnetic field $|H|^2/|H_0|^2$ on the (x, y) plane for *l*=1 at a wavelength of $\lambda \approx 1536\,nm$. (c) Total electric field $|E|^2/|E_0|^2$ and (d) total magnetic field $|H|^2/|H_0|^2$ on the (y, z) plane for *l*=5 at a wavelength of $\lambda \approx 1872\,nm$.

Understanding the different types of resonant modes and their characteristics is critical for designing and optimizing SBRs for various applications such as sensing, filtering, and lasing. Furthermore, the ability to control and manipulate these modes can lead to the development of novel photonic devices with unique functionalities.

2.2 Modelling techniques

Various numerical and computational techniques have been developed to investigate and solve complex electromagnetic problems, such as light scattering, guiding, localization, and propagation in photonic crystal structures. These methods comprise the Plane Wave Expansion Method (PWEM), the Finite Difference Time Domain (FDTD) technique, and the Finite Element Method (FEM) [21-25]. While FDTD and FEM are versatile approaches that directly discretize and solve Maxwell's equations, applicable to diverse dielectric structures, they demand substantial computational resources in terms of memory and time. On the other hand, PWEM primarily evaluates the band structure of propagating waves within photonic crystals. It is important to note that PWEM is subject to symmetry restrictions and is particularly well-suited for structures exhibiting a translationally symmetric lattice. To calculate resonant modes of photonic crystals containing defects, a supercell PWEM method that uses larger unit cells is needed, which further increases the computational demand. Additionally, the Spherical space Bessel-Legendre-Fourier numerical model has been developed for lossy materials or dielectric structures of arbitrary geometry, providing resonance state frequencies and field profiles [34]. The reliability of these techniques has been confirmed by comparing their computational results with those pioneer works published by G. Burlak et al. [28]. In their study, an analysis of a microsphere coated with spherical Bragg shells composed of 24 layers was performed, as shown in Figure 2-3.

Analytical solutions of Maxwell's equations provide a powerful tool for studying electromagnetic waves in Spherical Bragg Resonators (SBRs). Specifically, the properties of single and multilayered spherical structures had been acquired using the scattering matrix method [20]. Despite this, the recursive transfer-matrix algorithm developed by A. Moroz [14] has become the most commonly used method in recent years due to its simplicity, reliability, and computational efficiency [15]. This algorithm offers a general solution for fundamental cross-sections, orientation-averaged electric and magnetic field intensities, and the radiative decay rate of a dipole at any position in a multilayer sphere. By combining and manipulating transfer matrices, this algorithm has successfully addressed various light scattering problems in multilayer spheres [15-17].

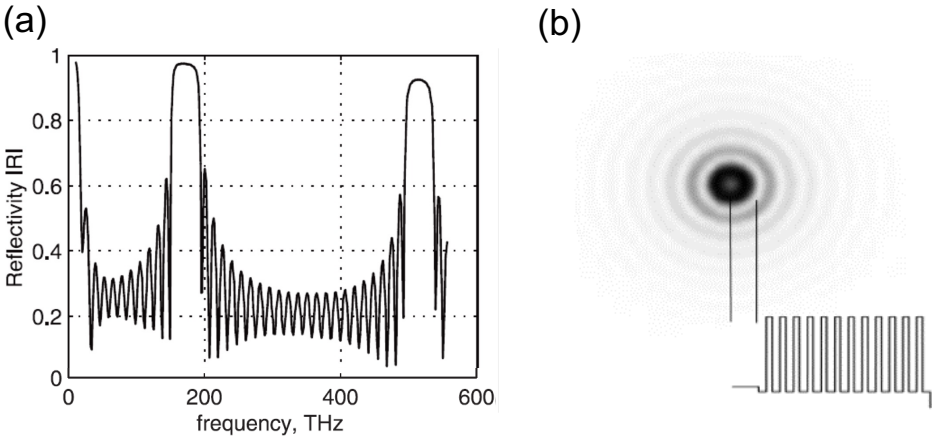

Figure 2-3 Reflectivity R of a Spherical Bragg Resonator with 24 layers. Figure taken with permission from [28]. (b) Corresponding normalized intensity profile H_ϕ field component, calculated using Spherical space Bessel-Legendre-Fourier (BLF) at the eigenfrequency $f = 188\ THz$. Figure taken with permission from [34].

Since this robust and powerful recursive transfer-matrix algorithm is adopted in our thesis, an exhaustive and detailed description is provided in the following subsection.

2.2.1 Recursive Transfer-Matrix method

The reliability and computational efficiency of the recursive transfer-matrix algorithm developed by A. Moroz [30] have made it the preferred method for many researchers in recent years [35-37]. In this method the electromagnetic fields within any shell are described by the stationary macroscopic Maxwell's equations:

$$\vec{E} = \frac{ic}{\omega\varepsilon}\left(\Delta \times \vec{H}\right) \qquad 2\text{-}4$$

$$\vec{H} = -\frac{ic}{\omega\mu}\left(\Delta \times \vec{E}\right) \qquad 2\text{-}5$$

where the permittivity ε and permeability μ are scalar quantities. The general solution of the Maxwell's equation for the electromagnetic field in the j-th shell is expressed as:

$$\vec{E}_{TE}(\vec{r}) = \sum_L\left[A_{TEL}(j)\vec{F}_{TEL}\left(k_j,\vec{r}\right) + B_{TEL}(j)\vec{G}_{TEL}\left(k_j,\vec{r}\right)\right] \qquad 2\text{-}6$$

$$\vec{E}_{TM}(\vec{r}) = \sum_L\left[A_{TML}(j)\vec{F}_{TML}\left(k_j,\vec{r}\right) + B_{TML}(j)\vec{G}_{TML}\left(k_j,\vec{r}\right)\right] \qquad 2\text{-}7$$

$$\vec{H}_{TE}(\vec{r}) = -i\frac{\varepsilon_n}{\mu_n}\sum_L\left[A_{TEL}(j)\vec{F}_{TML}(k_j,\vec{r}) + B_{TEL}(n)\vec{G}_{TML}(k_j,\vec{r})\right] \quad 2\text{-}8$$

$$\vec{H}_{TM}(\vec{r}) = -i\frac{\varepsilon_n}{\mu_n}\sum_L\left[A_{TML}(j)\vec{F}_{TEL}(k_j,\vec{r}) + B_{TML}(j)\vec{G}_{TEL}(k_j,\vec{r})\right] \quad 2\text{-}9$$

where $\vec{F}_{pL}(k_j,\vec{r})$ and $\vec{G}_{pL}(k_j,\vec{r})$ are vector multipoles that correspond to different linear combinations of spherical Bessel function and are well defined in [30, 37]. While the expansion coefficients A_{pL} and B_{pL} are obtained by matching the fields across the shell interfaces, as shown in Figure 2-4.

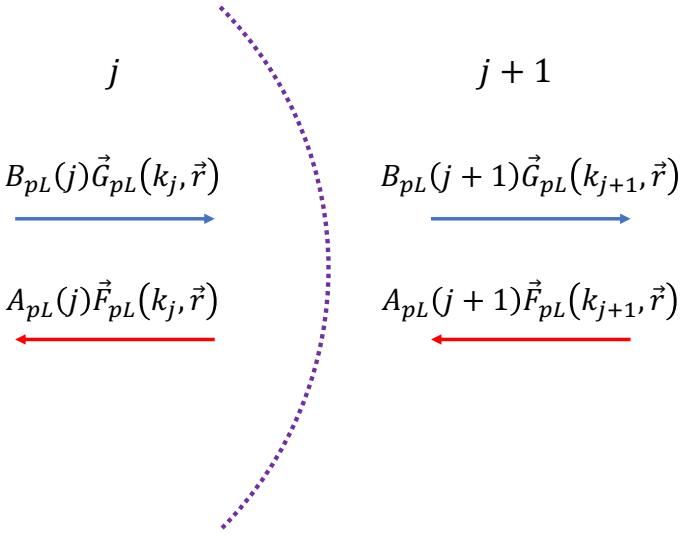

Figure 2-4 Schematic representation of the expansion coefficients A_{pL} and B_{pL} estimation by matching the fields across the adjacent shell interfaces j and $j+1$.

The 2×2 backward $T_{pl}^{+}(j)$ and forward $T_{pl}^{-}(j)$ transfer matrices defined by Moroz [30] relate the expansion coefficients A_{pL} and B_{pL} between adjacent regions, Equations 2-10 and 2-11:

$$\begin{pmatrix} A_{pL}(j+1) \\ B_{pL}(j+1) \end{pmatrix} = T_{pl}^{+}(j)\begin{pmatrix} A_{pL}(j) \\ B_{pL}(j) \end{pmatrix} \quad 2\text{-}10$$

$$\begin{pmatrix} A_{pL}(j) \\ B_{pL}(j) \end{pmatrix} = T_{pl}^{-}(j)\begin{pmatrix} A_{pL}(j+1) \\ B_{pL}(j+1) \end{pmatrix}. \quad 2\text{-}11$$

The transfer matrices (Equation 2-12 to 2-15) are unambiguously defined by ensuring the continuity of the tangential components of the electric field ($\vec{E}$) and magnetic field ($\vec{H}$) across the interfaces of the j-th shell.

$$T_{TMl}^{-}(j) = -i\begin{pmatrix} \tilde{n}\zeta_l'(x)\psi_l(\tilde{x}) - \tilde{\mu}\zeta_l(\tilde{x})\psi_l'(x) & \tilde{n}\zeta_l'(x)\zeta_l(\tilde{x}) - \tilde{\mu}\zeta_l(x)\zeta_l'(\tilde{x}) \\ -\tilde{n}\zeta_l'(x)\psi_l(\tilde{x}) + \tilde{\mu}\zeta_l(\tilde{x})\psi_l'(x) & -\tilde{n}\psi_l'(x)\zeta_l(\tilde{x}) + \tilde{\mu}\psi_l(x)\zeta_l'(\tilde{x}) \end{pmatrix} \quad 2\text{-}12$$

$$T_{TEl}^{-}(j) = -i\begin{pmatrix} \tilde{\mu}\zeta_l'(x)\psi_l(\tilde{x}) - \tilde{n}\zeta_l(\tilde{x})\psi_l'(x) & \tilde{\mu}\zeta_l'(x)\zeta_l(\tilde{x}) - \tilde{n}\zeta_l(x)\zeta_l'(\tilde{x}) \\ -\tilde{\mu}\zeta_l'(x)\psi_l(\tilde{x}) + \tilde{n}\zeta_l(\tilde{x})\psi_l'(x) & -\tilde{\mu}\psi_l'(x)\zeta_l(\tilde{x}) + \tilde{n}\psi_l(x)\zeta_l'(\tilde{x}) \end{pmatrix} \quad 2\text{-}13$$

$$T_{TMl}^{+}(j) = -i\begin{pmatrix} \zeta_l'(\tilde{x})\psi_l(x)/\tilde{n} - \zeta_l(\tilde{x})\psi_l'(x)/\tilde{\mu} & \zeta_l'(\tilde{x})\zeta_l(x)/\tilde{n} - \zeta_l(\tilde{x})\zeta_l'(x)/\tilde{\mu} \\ -\psi_l'(\tilde{x})\psi_l(x)/\tilde{n} - \psi_l(\tilde{x})\psi_l'(x)/\tilde{\mu} & -\psi_l'(\tilde{x})\zeta_l(x)/\tilde{n} - \psi_l(\tilde{x})\zeta_l'(x)/\tilde{\mu} \end{pmatrix} \quad 2\text{-}14$$

$$T_{TEl}^{+}(j) = -i\begin{pmatrix} \zeta_l'(\tilde{x})\psi_l(x)/\tilde{\mu} - \zeta_l(\tilde{x})\psi_l'(x)/\tilde{n} & \zeta_l'(\tilde{x})\zeta_l(x)/\tilde{\mu} - \zeta_l(\tilde{x})\zeta_l'(x)/\tilde{n} \\ -\psi_l'(\tilde{x})\psi_l(x)/\tilde{\mu} - \psi_l(\tilde{x})\psi_l'(x)/\tilde{n} & -\psi_l'(\tilde{x})\zeta_l(x)/\tilde{\mu} - \psi_l(\tilde{x})\zeta_l'(x)/\tilde{n} \end{pmatrix} \quad 2\text{-}15$$

The functions $\psi_l(x) = x\jmath_l(x)$ and $\zeta_l(x) = x\hbar_l^{(1)}(x)$ represent the Riccati-Bessel functions where $\jmath_l$ and $\hbar_l^{(1)}$ are the spherical Bessel functions of the first and third kind. The prime notation indicates the derivative with respect to the argument enclosed in parentheses. Additionally, the variables $x_j = k_j r_j$ and $\tilde{x}_j = x_j/\tilde{n}_j = k_{j+1} r_j$ correspond to the internal and external dimensionless size parameters, respectively. Here, $\tilde{n}_j = n_j/n_{j+1}$ denotes the relative refractive indices, and $\tilde{\mu}_j = \mu_j/\mu_{j+1}$ represents the relative permeabilities.

In general, the expansions coefficients from the sphere core $j = 1$ to the j-th shell (Equation 2-16) and form the surrounding media $J + 1$ to the j-th shell (Equation 2-17) can be obtained from the composite transfer matrices $\mathcal{T}_{pl}(j)$ and $\mathcal{M}_{pl}(j)$.

$$\begin{pmatrix} A_{pL}(j) \\ B_{pL}(j) \end{pmatrix} = \mathcal{T}_{pl}(j)\begin{pmatrix} A_{pL}(1) \\ B_{pL}(1) \end{pmatrix} \quad 2\text{-}16$$

$$\mathcal{M}_{pl}(n)\begin{pmatrix} A_{pL}(J+1) \\ B_{pL}(J+1) \end{pmatrix} = \begin{pmatrix} A_{pL}(j) \\ B_{pL}(j) \end{pmatrix} \quad 2\text{-}17$$

$$\mathcal{T}_{pl}(j) = \prod_{s=j-1}^{1} T_{pl}^{+}(s) \quad 2\text{-}18$$

$$\mathcal{M}_{pl}(j) = \prod_{s=j-1}^{1} T_{pl}^{-}(s) \quad 2\text{-}19$$

Thus, the pair of expansion coefficients $A_{pL}(j)$ and $B_{pL}(j)$ assigned to each shell, including the host medium (represented as the $J + 1$-th shell), is adequate to uniquely determine the electromagnetic field both inside and outside of a multilayered sphere. This determination is achieved by enforcing two essential regularity conditions.

The first regularity condition concerns the behavior of the solution at the origin of the sphere, ensuring that it remains well-behaved and finite $B_{TEL}(1) = B_{TML}(1) \equiv 0$. The second condition applies when a source is positioned outside the sphere. In this case, the coefficients $A_{pL}(J+1)$ at any given frequency ω correspond to the expansion coefficients of an incident electromagnetic field expressed in spherical coordinates.

The recursive transfer matrix algorithm has been found to be a robust and efficient approach to deal with light scattering phenomena occurring in multilayer spheres. This algorithm offers a complete solution for the fundamental cross sections as well as for the orientation-averaged intensities of the electric and magnetic fields. In addition, it allows calculating the radiative and nonradiative decay rate of a dipole located at any point of a multilayer sphere. A more exhaustive and detailed analysis of the practical application of this algorithm is located within the methodological section of the papers encompassed within this thesis.

2.3 Fabrication techniques

Multiple techniques have been suggested for the fabrication of multilayered spheres. These include the electron-beam deposition method employing ZnS/Na_3AlF_6 [38], multistage emulsion polymerization using polystyrene/poly(trifluoroethyl methacrylate) [39], sol-gel and homogeneous precipitation approaches for synthesizing SiO_2 and Y_2O_3 shells, respectively [40], as well as a combination of etching, plasma-enhanced techniques, and chemical vapor deposition [33, 41, 42]. The soft-matter approach has also been employed to achieve a 3D Bragg cavity using cholesteric liquid crystals [43]. These formations naturally give rise to a spherical microcavity characterized by a radial variation in the refractive index, leading to lasing in these solid-state structures [43].

The fabrication of SBR remains a challenging task even today. However, A. V. Medvedev et al., [41, 42] have recently demonstrated that radiofrequency plasma-enhanced chemical vapor deposition (RF-PECV) seems to be a promising technique for depositing thin, homogeneous layers with precise chemical composition and thickness control on a microscopic spherical particle. In this work, they report the fabrication of two types of SBR for near-infrared applications using radiofrequency plasma-enhanced chemical vapor deposition (RF-PECVD) at 13.56 MHz [41, 42]. The following section will describe these fabrication processes in more detail.

2.3.1 PECVD for SBRRs fabrication

The materials of choice were hydrogenated amorphous silicon carbide (*a*-$Si_{1-x}C_x$:H) and amorphous silicon oxide (a-SiO_2). Alternating *a*-$Si_{1-x}C_x$: H and a-SiO_2 layers were deposited on a 0.26 mm diameter silicate-sodium-calcium-silicate glass microsphere. The microsphere was glued with a silicone sealant to the end of a 20 mm long quartz fiber. The other end of the fiber was attached to the center of the lower flat electrode and oriented vertically with respect to the electrode surface (Figure 2-5) [41].

The alternation of the layers was given by changing the gas fluxes. In the *a*-$Si_{1-x}C_x$: H reservoir, the gas flux ratio CH4/[CH4 + SiH4] was maintained at a level of 0.1, that belongs to a composition with x = 0.1. In the reactor, the operational pressure ranged from 0.1 to 0.2 Torr. The radiation frequency was set at 17 MHz, while the high-frequency power was maintained between 0.03 and 0.1 W/cm². The substrate temperature varied within 200 to 250°C, and the collective gas flow rate reached 5 to 10 sccm. When cultivating alpha-phase silicon dioxide (α-SiO_2) layers, the silane-to-oxygen flux ratio was approximately 1:1 [41].

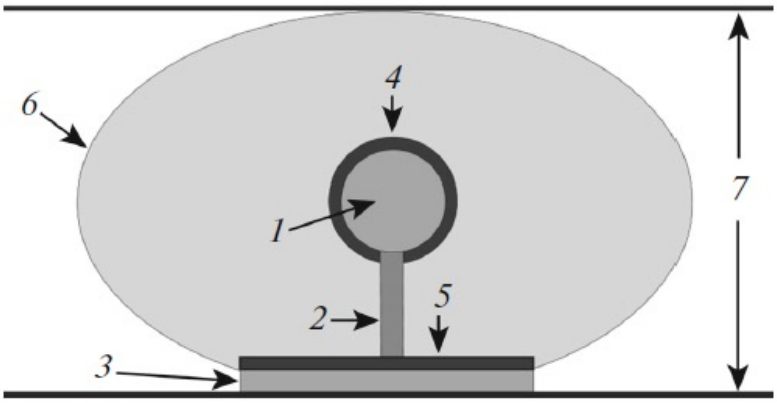

Figure 2-5 Diagram illustrating a reactor chamber with a microsphere: (1) glass microsphere, (2) quartz fibre, (3) circular quartz substrate, (4) layer deposited on microsphere, (5) layer deposited on substrate, (6) plasma discharge, and (7) electrodes. Figure taken with permission from [41].

An asymmetrical electrode configuration was employed in a PECVD setup, where the lower electrode was grounded. The separation between the flat electrodes was set at 50 mm. In order to enhance the uniformity of layer deposition across the interelectrode space, a consistent temperature

distribution was established by heating both the grounded lower electrode and the high-frequency top electrode simultaneously [41, 42].

Furthermore, an initial correlation was established between the deposition rate of a layer at a specific point on a vertically mounted quartz slab, positioned centrally with respect to the lower electrode and coinciding with the microsphere's location within the discharge region. This correlation was made with the deposition rate on a quartz rod placed on the lower flat electrode. The layer thicknesses were determined by analyzing interference patterns in the reflection spectra. Moreover, the thicknesses of the layers deposited on the microsphere were continuously monitored through in situ interferometry, comparing their growth rates and thicknesses with those of flat layers applied to a horizontal quartz slab on the electrode [41, 42].

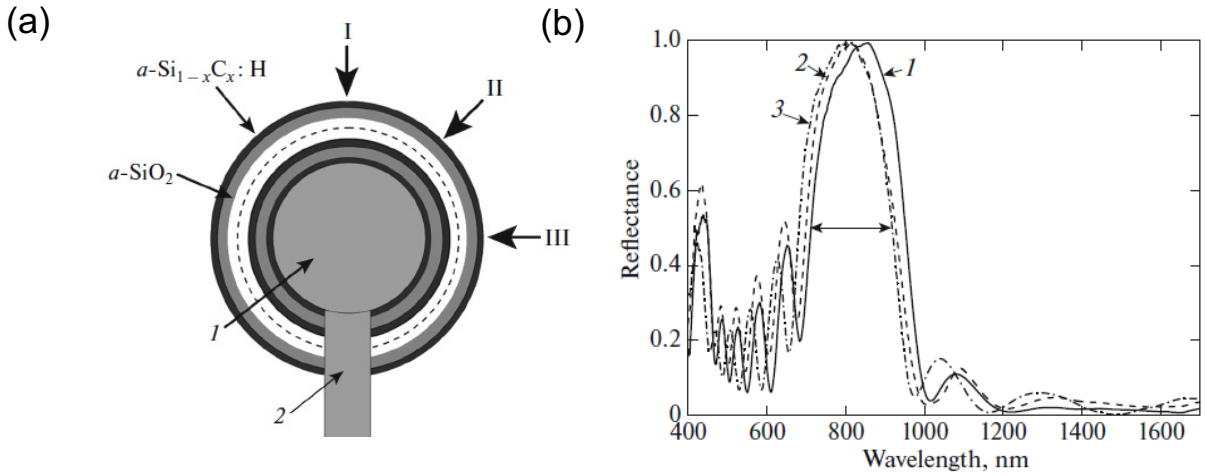

Figure 2-6 (a) Structure of the SBRR: (1) glass microsphere and (2) quartz fibre. (b) Reflection spectra collected at points I, II, III and normalized with respect to the maximum reflection coefficient. Figure taken with permission from [41].

Using this method, it was possible to fabricate an SBRR with a core diameter of 0.26 mm and 11 alternating layers of *a*-$Si_{1-x}C_x$: H (83 nm thick) and a-SiO_2 (141 nm thick) (Figure 2-6). This layer thickness was chosen such that the center of the Bragg reflection band was in the near-infrared spectral range at a wavelength of λ_0 = 820 nm [41].

2.4 Active nanophotonic applications

In the following section, a comprehensive exploration is performed to provide an overview of the research areas associated with the applications proposed and investigated in this thesis. This in-depth review focuses on areas where spherical Bragg resonators (SBRs) promise to enhance existing functionalities or introduce new capabilities. Among others, these include fields such as optical sensing, light manipulation, energy harvesting, and integrated photonics.

2.4.1 Spontaneous emission engineering

In 1946, Purcell proposed that spontaneous emission was not exclusively a property of the emitter but also its surroundings [44]. Specifically, the presence of a resonant cavity at the emitter's frequency can increase its spontaneous emission rate, a phenomenon now referred to as the Purcell effect [45, 46]. This proposal sparked interest in quantum electrodynamics, leading to numerous experiments over the subsequent decades [47, 48].

One such experiment was conducted by Goy et al. in 1983, where they observed a shortening of the spontaneous emission rate of Rydberg atoms placed inside cavities [49]. In 1987, Yablonovitch suggested applying concepts of quantum electrodynamics in cavity design to create more efficient optoelectronic processes [50]. More recently, quantum electrodynamics has been applied to quantum dots inside cavities, where the control of spontaneous emission has been observed and utilized to create single-photon sources through micropillar cavities [51-53].

To attain a substantial enhancement in emission rate (Γ/Γ_0), it is essential to employ an optical resonator capable of confining light within compact dimensions and preserving it over an extended duration. Nevertheless, these two criteria exhibit a certain level of contradiction, as achieving tighter confinement tends to result in elevated losses. Thus, research into emission modification primarily focuses on developing resonators that optimize this trade-off. A formula introduced by Purcell shows that the Purcell factor, the ratio between modified Γ and free-space emission rates Γ_0, is [33, 54]:

$$\mathrm{F}_P = \frac{\Gamma}{\Gamma_0} = \frac{3}{4\pi^2}\frac{Q}{\mathrm{V}_{eff}}\left(\frac{\lambda_0}{n_c}\right)^3 \qquad 2\text{-}20$$

where λ_0 represents the transition wavelength, Q is the quality factor of the cavity mode, and V_{eff} is its volume. This condition holds under two main circumstances: first, when the cavity's resonance linewidth is broader than the emission linewidth of the active element, and second, when the dipole is precisely aligned with the polarization of the cavity mode and accurately positioned at the maximum field within this mode [55, 56].

The modal volume V, also known as the effective volume or effective mode area, is a parameter that describes the ability of a cavity to confine the electromagnetic field [57]. Essentially, it represents the volume that the field would occupy if it were uniformly distributed and equal to its maximum value.

$$\iiint \left|\vec{E}(\vec{r})\right|^2 d^3\vec{r} = \mathrm{V}\left|\vec{E}(\vec{r})\right|^2_{max} \tag{2-21}$$

or:

$$V = \frac{\iiint \left|\vec{E}(\vec{r})\right|^2 d^3\vec{r}}{\left|\vec{E}(\vec{r})\right|^2_{max}} \tag{2-22}$$

The quality factor, Q, is a measure of the ability of an electromagnetic cavity to store energy [58]. It is defined for any resonator in the limit of weakly damped oscillations as:

$$Q = \frac{2\pi(Energy\ storage)}{(Dissipated\ energy\ per\ cycle)} \tag{2-23}$$

In the context of a cavity, let τ_p represent the characteristic lifetime of a photon. The decay of the energy stored within the cavity over time follows an exponential pattern, where τ_p denotes the characteristic damping time associated with this decay process.

If we define $\xi(t)$ as the wave that is stored within the cavity, we can express the intensity I as follows:

$$\mathrm{I}_{storage} \propto e^{-t/\tau_p} \propto |\xi(t)|^2 \tag{2-24}$$

Hence:

$$|\xi(t)| \propto e^{-t/2\tau_p} e^{i\omega_0 t} \tag{2-25}$$

In Fourier space, our wave can be written as:

$$\xi(\omega) = \int_0^{+\infty} e^{-t/2\tau_p} e^{i\omega_0 t} e^{-i\omega t} dt \quad 2\text{-}26$$

or

$$\xi(\omega) = \frac{1}{\frac{1}{2\tau_p} + i(\omega_0 - \omega)} \quad 2\text{-}27$$

The intensity profile of our wave, which is directly proportional to the square magnitude of $\xi(\omega)$, exhibits a Lorentzian distribution. This Lorentzian profile is centered at ω_0 and has a width of $\Delta\omega = 1/\tau_p$. The relationship between the width and the inverse of the pulse duration is established as follows:

$$|\xi(\omega)|^2 = \frac{1}{\frac{1}{4{\tau_p}^2} + (\omega_0 - \omega)^2} \quad 2\text{-}28$$

Hence, when a significant portion of the energy is dissipated within a time interval τ_p, only a fraction $\frac{T}{\tau_p} = \frac{2\pi}{\omega}\Delta\omega$ of the stored energy is lost over a complete period $T = \frac{2\pi}{\omega}$. Consequently, we can express the quantity Q (as given by Equation 2-21) in the following manner:

$$Q = \frac{2\pi(Energy\ storage)}{(Energy\ storage)\frac{2\pi}{\omega}\Delta\omega} \quad 2\text{-}29$$

$$Q = \frac{\omega}{\Delta\omega}. \quad 2\text{-}30$$

In the quest for advanced methods of controlling and manipulating light emission, photonic crystal (PC) microcavities have emerged as the most promising resonators [47, 48]. PC microcavities are unique structures that modulate the refractive index periodically on a scale comparable to the wavelength of light, enabling fascinating optical phenomena. This periodic modulation gives rise to a stopband, also known as a photonic bandgap, wherein specific frequencies of light are prohibited from propagating [17, 59]. The suppression of light density of states (LDOS) within the stopband results in a reduction of emission [50], presenting exciting opportunities for emission modification and light confinement [60].

Early demonstrations of this phenomenon were observed in *woodpile* PC structures, which were fabricated using a complex wafer-fusion technique [61]. Concurrently, *inverse-opal* PC structures were independently formed through a self-assembly technique [62], further validating the potential of PC microcavities for emission control. In the inverse-opal structures, emission rates were

reduced within the stopband, but intriguingly, they increased at the stopband's edge. This effect indicates a redistribution of the LDOS from within the stopband to the band edge, highlighting the unique properties of PC microcavities [3].

Introducing localized defects in the PC lattice underlines an essential aspect of emission modification in these microcavities. In the presence of strong disorder, localized photonic states form within the stopband, resulting in defect cavities [63]. These defect cavities act as optical cavities, where the surrounding PC behaves as a mirror, confining light in all directions. Thus, investigating these defect cavities has become a focal point of research in emission modification using PCs [60, 64-66].

Among various photonic crystal (PC) microcavity designs, the L3 PC microcavity is one of the most widely used configurations. It is constructed by removing three adjacent holes along a row within a hexagonal lattice and modifying the geometry of nearby holes to mitigate abrupt edge transitions, thereby suppressing undesired scattering, and improving optical confinement [67, 68]. Another design strategy involves the W1 defect waveguide, created by removing an entire row of holes in the hexagonal lattice. This configuration supports light propagation along the line defect, making it useful for waveguiding applications [69]. Enhancing the quality factor (Q) of these microcavities is critical for applications that require strong light-matter interactions, and this can be achieved through structural modifications such as introducing heterostructures [70, 71].

A key aspect of optimizing PC microcavities for defect modes is the precise tuning of emitter frequency and spatial positioning within the cavity. Frequency matching between the cavity mode and the emitter can be controlled through various methods, including thermal tuning [72] or with the external electric fields [73]. Furthermore, the spatial positioning of emitters relative to the cavity mode is critical, and advanced techniques has been proposed [74-76].

While three-dimensional PCs with engineered defects present significant fabrication challenges, researchers have successfully explored the potential of defect cavities in two-dimensional PC structures [63, 77]. PC cavities have achieved remarkably high-quality factors through carefully engineered designs, reaching values as high as 10^4 [66, 72]. However, the fundamental limitations imposed by the diffraction limit define the minimum achievable mode volume of the cavity,

approximately equal to $0.1(\lambda_0/n)^3$ [78-80], with λ_0 representing the free-space wavelength associated with the transition and n denotes the refractive index of the medium within the cavity.

An alternative avenue for emission modification emerged with the use of metal nanoparticles (MNPs). Unlike PCs, MNPs are not subject to the diffraction limit as light confinement arises from coupling to plasmons in the metal, allowing for smaller mode volumes on the order of $10^{-6}(\lambda_0/n)^3$ [81, 82]. Nevertheless, strong confinement also introduced significant optical losses, resulting in lower quality factors for MNPs [83, 84].

In this Thesis, we study a novel class of resonators known as spherical Bragg resonators (SBRs). Our research in Article 1 experimentally demonstrates how SBRs can act as omnidirectional cavities, effectively modifying spontaneous emission processes by altering the density of electromagnetic states compared to free space. The following chapters present our findings on the engineering of spontaneous electromagnetic emission processes using SBRs. In Article 2, we explore the realm of optical amplification and lasing, highlighting the transformative role that SBRs can play in advancing photonics technologies. In Article 3, we delve into the application of SBRs as dielectric nanoantennas, showcasing their capabilities in enhancing light-matter interactions. Article 4 presents a novel Tamm plasmon-like resonance supporting structure composed of an Au/SiO_2 core-shell metal nanosphere encased by a TiO_2/SiO_2 Spherical Bragg Resonator (SBR). The cavity between the metal core and the SBR supports high-Q Tamm plasmon-like modes.

2.4.2 Loss compensation and amplification

Nanophotonics, a rapidly evolving field at the intersection of nanotechnology and photonics, has opened up exciting possibilities for manipulating light at the nanoscale [85, 86]. In this section, we delve into a critical aspect of nanophotonics: nanophotonic losses, which significantly impact the efficiency and performance of nanoscale optical systems.

Two fundamental types of nanophotonic losses demand our attention: material losses and radiative losses. Material losses arise from energy dissipation processes within nanoscale materials, encompassing phenomena such as the generation of phonons, non-radiative processes like Auger recombination or defect-mediated relaxation [85, 87]. These mechanisms convert absorbed photon

energy into different forms, leading to a decrease in the overall optical efficiency of the nanoscale system.

Radiative losses, on the other hand, occur when electromagnetic energy escapes the confined volume of the nanostructure, dispersing into the far-field region. This escape takes place through processes like emission or scattering of photons outside the desired localized area. A common source of radiative losses is the existence of leaky modes, which result from imperfections or irregularities in the nanoscale structure, causing unwanted light leakage [88]. Another source is radiation damping, wherein an oscillating dipole in the nanoscale structure emits energy in the form of electromagnetic radiation [89].

To address these challenges and enhance nanophotonic systems, researchers have successfully integrated active materials or gain media across various nanophotonic platforms, including nanoparticles, photonic crystals, plasmonic waveguides, and metamaterials. Incorporating active materials has proven to be a highly effective strategy for compensating for losses and improving light-matter interactions and emission properties [85, 90].

Active materials, such as semiconductor nanocrystals (quantum dots) and doped dielectrics, have gained significant attention as key components in nanophotonic devices due to their capacity to achieve optically or electrically induced population inversion. Semiconductor nanocrystals offer the advantage of size-tunable emission properties, allowing for precise control over the emission wavelength. This is crucial for lasers, light-emitting diodes (LEDs) applications, and biomedical imaging [91-93]. These materials can exhibit high quantum efficiency and provide robust emission stability, making them suitable for integration into photonic circuits where miniaturization and performance are critical [94].

Doped dielectrics, on the other hand, introduce additional energy levels within the bandgap of the host material, which facilitates population inversion and stimulated emission processes. For instance, rare-earth doped dielectrics such as erbium-doped silica fibers have been extensively utilized in optical amplifiers, compensating for material losses and enabling efficient light amplification [85]. These materials are particularly valuable in fiber-optic communication systems, which enhance signal strength over long distances, and in integrated photonic circuits, where compact, on-chip amplification is required [95, 96]. The ability to achieve narrow line widths and

high gain makes doped dielectrics attractive for various nanophotonic applications, including lasers and sensors [27, 97].

Ongoing research in active materials focuses on enhancing these media's performance, efficiency, and stability by exploring novel material compositions and doping strategies. For example, incorporating co-dopants can improve energy transfer efficiency and reduce quenching effects, which are critical for maintaining high performance in high-density doping regimes [98]. Additionally, new fabrication techniques, such as ion implantation and molecular beam epitaxy, are being developed to precisely control the spatial distribution of dopants, further optimizing light-matter interactions [99]. These advancements are driving significant progress in nanophotonic, enabling the development of more efficient, compact, and tunable devices [27].

The focus of Article 2 is on the integration of active materials into the target photonic structure of this thesis, SBR, seeking to harness their potential for achieving enhanced light confinement, reduced propagation losses, and improved device efficiency. Moreover, we analyze the behavior of a gain medium in the non-lasing regime, where classical electrodynamics can be employed without delving into the complex quantum dynamics of the ground and excited states. This enables us to approximate the gain medium as a dielectric material with a complex refractive index, where real part, which determines the phase delay experienced by light passing through the medium, and an imaginary part, responsible for the absorption or amplification of the light. In the case of a gain medium, the negative imaginary part of the refractive index signifies an amplifying effect, compensating for the material losses and resulting in a net gain [100, 101].

$$n_{core} = n_o + i\gamma \tag{2-31}$$

Advancements in nanophotonic have led to a deeper understanding of material properties crucial for tailoring and optimizing optical devices. One such parameter of paramount importance is the gain factor (γ), which characterizes a material's ability to either amplify ($\gamma < 0$) or absorb ($\gamma > 0$) an electromagnetic field. In this Thesis, we explore the intricate relationship between the gain factor and the material gain parameter (g), represented by $4\pi\gamma/\lambda$ $[cm^{-1}]$, where λ denotes the free-space wavelength [85].

When the system is undercompensated, it exhibits behavior akin to typical dielectric materials but with notable distinctions. Stronger electromagnetic fields envelop the structure, and narrower

resonances are observed. Conversely, an overcompensated system transforms into an optical amplifier, showcasing its potential for amplification at frequencies beyond its resonances. Remarkably, a laser-like behavior manifests when losses are fully compensated at frequencies close to resonance [85, 101]. To describe the post-threshold operation effectively, the consideration of a nonlinear permittivity function becomes imperative [102].

The performance of single-frequency lasers is characterized by the full width at half maximum of their power spectral density (linewidth). In the Schawlow-Townes approximation, increasing the cavity length and pump power can effectively reduce the linewidth, enhancing the laser's spectral purity [85, 86].

This comprehensive modeling approach is a powerful tool in our research, allowing us to predict and characterize the optical behavior of gain media under various conditions, such as varying material parameters. For the first time to our knowledge, the versatility of this model allows us to demonstrate the ability to design optical amplification and threshold gain for lasing in SBRs, as detailed in Article 2.

2.4.3 Resonant scattering of dielectric nanosphere

Over the last decade, significant research efforts have been directed toward exploiting the Purcell enhancement to manipulate electric dipole transitions in light-matter interactions. However, relatively less attention has been given to manipulating magnetic dipole and higher-order optical transitions. The interaction Hamiltonian $\mathcal{H}$ between light and matter in photoexcitation and relaxation processes can be precisely described using a multipolar expansion of the electric ($\vec{E}$) and magnetic ($\vec{B}$) fields [103]. This expansion involves electric dipole moment ($\vec{p}$), magnetic dipole moment ($\vec{m}$), and electric quadrupole moment ($\vec{q}$), represented as:

$$\mathcal{H} = -\vec{p} \cdot \vec{E} - \vec{m} \cdot \vec{B} - [\vec{q}\nabla]\vec{E} \ldots \qquad 2\text{-}32$$

The optical transition governed by the second term on the right-hand side, corresponding to the magnetic dipole transition, is typically much weaker than the first term, representing electric dipole transitions [104]. Only in cases where electric dipole transitions are prohibited does the second term dominate the emission process.

Like the widely studied Purcell effect, which influences electric dipole transitions, local photonic environments can also be utilized to control magnetic dipole transitions, giving rise to the magnetic Purcell effect [104]. To exploit this phenomenon, researchers have explored the utilization of optical cavities featuring metallic mirrors and plasmonic nanostructures that exhibit magnetic resonances. The aim is to control and enhance magnetic dipole transitions in rare earth ions like Eu^{3+} [105] and Er^{3+} [106]. However, a notable limitation arises from the inherent absorption losses of noble metals within the visible range. These losses result in significant quenching of nearby emitters, thereby restricting the enhancement achievable for magnetic dipole transitions.

Mie-type dielectric nanoantennas have garnered considerable attention as a promising alternative to address this challenge. As we will demonstrate later, dielectric nanostructures with a high refractive index and a size of $100\,nm$ or larger exhibit electric and magnetic multipolar Mie resonances that is not associated with significant non-radiative losses in the visible and infrared spectral range [107]. These structures function as low-loss resonators for electric Purcell enhancement and hold great potential for magnetic Purcell enhancement. Both theoretical [107-109] and experimental [110, 111] approaches have been taken to understand the behavior of these structures. As, it was well established by Mie et al. in 1908, the electric and magnetic resonant modes of a sphere with diameter d_p and refractive index n subrounded by a medium of refractive index n_m are determinate by the following expressions [112]:

$$a_n = \frac{m\Psi_n(mx)\Psi_n'(x) - \Psi_n(x)\Psi_n'(mx)}{m\Psi_n(mx)\xi_n'(x) - \xi_n(x)\Psi_n'(mx)} \quad 2\text{-}33$$

$$b_n = \frac{\Psi_n(mx)\Psi_n'(x) - m\Psi_n(x)\Psi_n'(mx)}{\Psi_n(mx)\xi_n'(x) - m\xi_n(x)\Psi_n'(mx)} \quad 2\text{-}34$$

where Ψ_n and ξ_n are Riccati-Bessel functions.

$$m = n/n_m \quad 2\text{-}35$$

$$x = \pi d_p n_m/\lambda \quad 2\text{-}36$$

The expansion coefficients a_n and b_n correspond to the scattering amplitudes of the electric dipole (ED) and magnetic dipole (MD) modes. We can calculate the electric field at any point surrounding the sphere with these coefficients. However, for convenience, it is common to express the overall response using the extinction, scattering, and absorption efficiencies given by the following expressions [113], respectively.

$$Q_{ext} = \frac{2}{x^2}\sum_{n=1}^{\infty}(2n+1)Re\{a_n + b_n\} \quad 2\text{-}37$$

$$Q_{sca} = \frac{2}{x^2}\sum_{\infty}^{n=1}(2n+1)(|a_n|^2 + |b_n|^2) \quad 2\text{-}38$$

$$Q_{abs} = Q_{ext} - Q_{sca} \quad 2\text{-}39$$

A more general method for multilayered spheres has been proposed by Moroz et al. [30]. This fast matrix transfer method, introduced in Section 2.2.1, was utilized to efficiently handle the complexities of the spherical multilayered structure objective of the study of this thesis.

Figure 2-7 illustrates the distinct modes induced by plane wave excitation in a schematic representation. In Figure 2-7 (a), we observe the electric dipolar (ED) and magnetic dipolar (MD) modes. The ED mode arises from the collective polarization of the nanoantenna material, leading to the generation of a magnetic current loop. On the other hand, the MD mode originates from an electric displacement current loop, resulting in the creation of a magnetic dipole moment. In addition, Figure 2-7 (b) shows the contributions of the electric dipole (ED), magnetic dipole (MD), and magnetic quadrupole (MQ) resonances to the total scattering from a 260 nm Si sphere. These resonances play significant roles in shaping the scattering behavior of the nanoantenna and hold importance in the overall interaction with incident light.

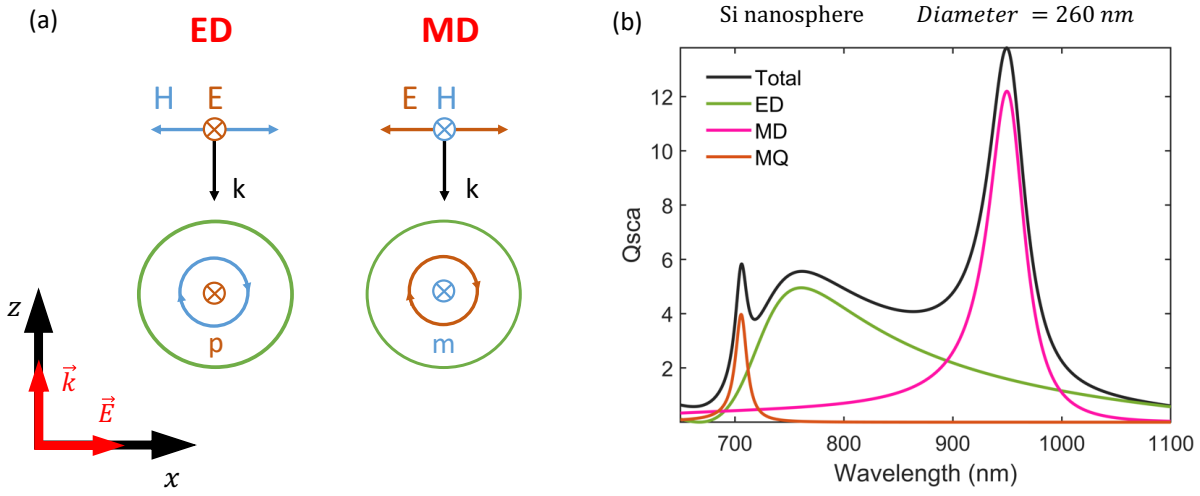

Figure 2-7 (a) Representation of the electric dipolar (ED) and magnetic dipolar (MD) resonant modes induced in a high refractive index dielectric sphere by a plane wave excitation. The ED mode arises from the collective polarization of the nanoantenna material, leading to the generation of a magnetic current loop. On the other hand, the MD mode originates from an electric

displacement current loop, resulting in the creation of a magnetic dipole moment. (b) contributions of the electric dipole (ED), magnetic dipole (MD), and magnetic quadrupole (MQ) resonances to the total scattering from a 260 nm Si sphere.

Analytical solutions for the resonances supported by nanospheres made of silicon (Si), considering a growing range of radii from 60 nm to 130 nm, are examined as follows. Figure 2-8 displays the total scattering efficiency ($Qsca$) calculated using Equation 2-38 as a function of the Si nanosphere's radius and the wavelength of the incident plane wave, revealing the electric and magnetic modes sustained by these nanospheres with a high refractive index. With increasing dimensions of the Si nanosphere, both the electric dipole (ED) and magnetic dipole (MD) modes experience a redshift, and nanoresonator-supported modes of higher order emerge. This shift is attributed to a more significant segment of the displacement current loop that persists within the Si nanosphere as the radius increases. Moreover, as the volume and polarizability of the nanosphere grow, the scattering efficiency and the intensity of the resonant mode peaks increase accordingly. The pure Mie resonances in silicon nanoparticles (Si NPs) can be further tailored by manipulating various structural parameters, such as altering the particle shape to ellipsoids [114], choosing specific substrates [115], or forming complex configurations like dimers and oligomers [116].

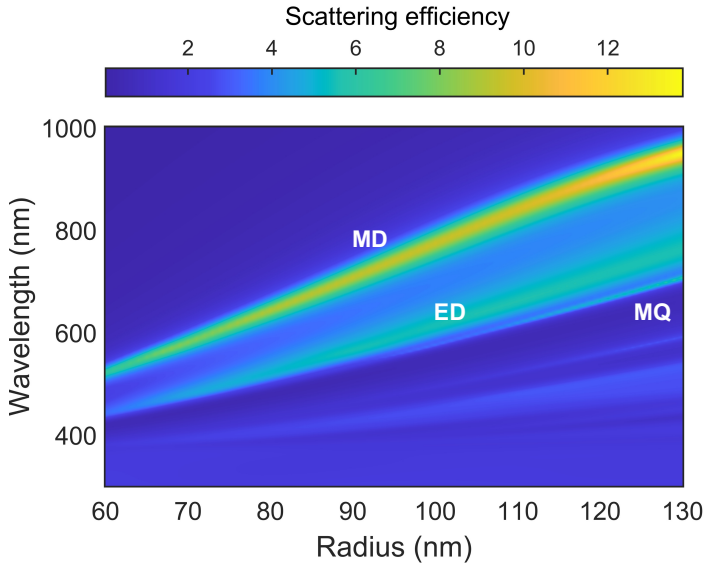

Figure 2-8 Total scattering efficiency as a function of incident plane wave wavelength and radius of a Si nanosphere.

The study of dielectric nanoparticle resonances continues to captivate the attention of researchers in physics, materials science, and engineering due to their exceptional capability to manipulate light with minimal energy loss [89, 103, 115]. When optical emitters such as dye molecules and two-dimensional materials are placed near resonant nanoantennas, coherent interactions between the excitons of the emitters and the resonant modes of the nanoantennas can occur [117]. This phenomenon, known as resonance coupling, has become a focal point of research because it can advance fundamental understanding and enable applications in nanophotonics, including quantum information processing, exciton-polariton lasing, and all-optical switching [118-120].

Experimental studies have demonstrated that silicon nanospheres placed on a monolayer of WS_2 can exhibit Fano interference, characterized by unidirectional light scattering and tunability through temperature control [121]. The investigation of resonance coupling has also been extended to nonspherical geometries, such as silicon nanodisks coupled with dye aggregates. In these configurations, the electric dipole (ED) and magnetic dipole (MD) resonances in silicon nanodisks can be independently manipulated, allowing for distinct excitonic coupling at each resonance mode [122]. Moreover, complex dielectric nanoresonators, like silicon nano grooves, have been employed to generate unidirectional Fano resonances when combined with molecular excitations [123].

Researchers have recently demonstrated the capability of dielectric spheres [110], dimers [124], and air/Si 6-ring circular gratings [125] to control magnetic dipole emission and achieve high magnetic Purcell factors. However, they have also discovered that the reported Purcell factor values are highly sensitive to the orientation and location of the magnetic dipole.

In Article 3, we delve into the promising domain of enhancing magnetic fields in fully dielectric spherical nanoantennas by leveraging Spherical Bragg Resonators (SBRs). Our focus is on boosting the magnetic transitions of quantum emitters. Notably, SBRs possess an omnidirectional nature and exhibit significantly high magnetic Purcell factor values while displaying minimal dependence on emitter polarization and position. This work explores the potential of SBRs as a powerful tool to advance magnetic field enhancement and pave the way for exciting applications in quantum optics and beyond.

2.4.4 Tamm plasmonic polaritons

As previously discussed, extensive research has been conducted on the interplay between metal nanostructures and resonant light, offering a potential solution to surpass the diffraction limit in photonic crystal cavities. This interaction has achieved optical intensity manipulation at deep-subwavelength scales like never before [126, 127]. The key mechanism behind this phenomenon is surface plasmon resonances (SPRs). These resonances, result from the collective oscillations of conduction electrons of charges q and mass m, leading to the accumulation of a density n of induced charges at the metal surface and significant local field enhancements [126, 128], as depicted in Figure 2.9 (a). The plasmons generated within a nanoparticle can be likened to a mass-spring harmonic oscillator driven by resonant light waves. These plasmons oscillate as a simple dipole aligned parallel to the electric field of the incident electromagnetic radiation [129]. For the excitation of Localized Surface Plasmon (LSP), the incident light must possess a frequency that resonates with the plasmonic oscillation [130].

The complex dielectric constant of a metal nanoparticle is given by [126]:

$$\varepsilon(\omega) = \varepsilon'(\omega) + i\varepsilon''(\omega) = 1 - \frac{\omega_p^2}{\omega^2 + i\frac{\omega}{\tau}} \qquad 2\text{-}40$$

where $\omega_p^2 = nq^2/m\varepsilon_0$ is the plasmon frequency and $\varepsilon'(\omega)$ and $\varepsilon''(\omega)$ are the real and the imaginary parts, respectively:

$$\varepsilon'(\omega) = 1 - \frac{\omega_p^2\tau^2}{1+\omega^2\tau^2} \qquad 2\text{-}41$$

$$\varepsilon''(\omega) = \frac{\omega_p^2\tau}{\omega(1+\omega^2\tau^2)}\,. \qquad 2\text{-}42$$

The real and imaginary parts of the dielectric constant of a metal are fundamental factors that influence two critical aspects of plasmonic behavior: the position of the surface plasmon resonance (SPR) and the bandwidth of the plasmonic oscillations. These losses, which govern the persistence of plasmonic oscillations, originate from a variety of sources. Prominent factors encompass radiative damping, confinement of the electron gas, structural irregularities, and thermal losses in metals [131]. Among these sources, intra-band transitions stand out as the primary cause of loss in many plasmonic systems, particularly in the case of gold nanoparticles (Au NPs) [132]. These

intra-band transitions involve single-particle excitations from occupied valence bands to unoccupied levels within the conduction band.

In the pursuit of efficient and stable plasmonic systems, the choice of metal becomes paramount. Gold, a well-known plasmonic material, boasts several advantages over other metals like silver and copper. Apart from exhibiting strong SPR bands in the visible region, gold demonstrates superior biocompatibility, chemical stability, and higher resistance to surface oxidation and dissolution in liquid environments over time [132].

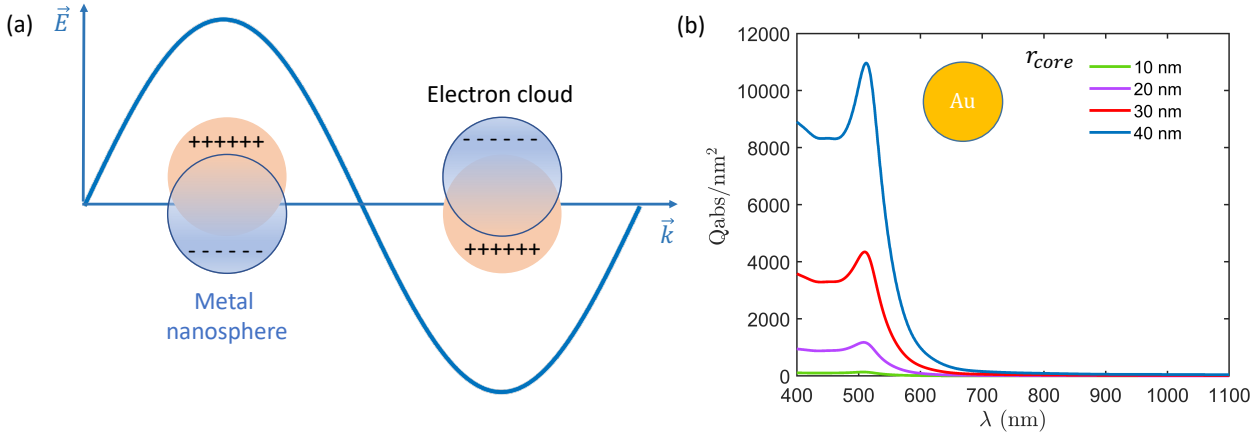

Figure 2-9 (a) Schematic representation of surface plasmon resonance in plasmonic nanoparticles. (b) Extinction spectra of gold nanoparticles of different sizes.

Localized Surface Plasmon (LSP) excitation is a crucial aspect in the study of nanophotonics. LSP excitation occurs when incident light resonates with the plasmonic oscillation, requiring a specific frequency alignment [133, 134]. Several factors play a significant role in determining the LSP frequency, including the dielectric constant of the surrounding medium and the size, shape, and composition of the nanoparticles [127]. Notably, gold nanoparticles (Au NPs) exhibit a distinctive Surface Plasmon Resonance (SPR) band around 520 nm in the visible spectrum. The behavior of this SPR band is strongly influenced by the size of the Au NPs, as depicted in Figure 2.9 (b).

Remarkably, the SPR band of Au NPs with sizes smaller than $10\,nm$ undergoes substantial damping. This damping effect can be attributed to the increased rate of electron-surface collisions in smaller particles, leading to significant phase changes [132]. On the other hand, larger particle sizes result in a redshift of the SPR wavelength along with an increase in intensity. Particles

exceeding $100\,nm$ in size exhibit noticeable band broadening, primarily due to the dominant contributions from higher-order electron oscillations [132].

On the other hand, Tamm plasmons (TPs) have emerged as a captivating and promising class of nanoplasmonic structures, offering many unique properties and practical applications. By coupling localized surface plasmon resonances (LSPRs) in a metal and surface electromagnetic waves in a Bragg reflector, Tamm plasmon polaritons (TPPs) manifest as a confined hybrid plasmon mode at the interface between these two structures [135, 136]. The confined nature of TPPs grants them remarkable field enhancement capabilities and renders them remarkably sensitive to environmental changes. As a result, TPPs have garnered considerable interest across numerous scientific disciplines and technological domains that include the realm of perfect absorbers, filters, nanoscale lasers, bistable switches, sensors, thermal emitters, solar photovoltaic cells, photodetectors, and photo-catalysis [137-141].

Photonic crystals (PCs) have emerged as promising platforms for harnessing high-quality plasmon resonances, opening up new possibilities for advancing photonic and optoelectronic devices [142]. Among the various PC configurations investigated for Tamm plasmon research, distributed Bragg reflectors (DBRs) have gained widespread attention due to their superior performance. DBRs consist of alternating layers with high and low refractive indices, and their optical thickness approximates one-quarter wavelength [143-145].

Different studies have demonstrated the potential of Tamm plasmons in developing innovative light sources. For example, in 2013, researchers successfully created laterally confined lasers by limiting the contact between the metal and DBR to micro-discs, achieving diameters as small as 4 μm [146]. In 2015, it was shown that slightly modifying the geometry of the metal-DBR interface to a rectangular contact area could produce laser emission with a linear polarization aligned with the rectangle's shape [147]. Beyond lasing applications, Tamm plasmons have been employed in surface mode control to couple with surface plasmons, develop single-photon sources, and create compact quantum-box sources for optical telecommunications [148-150].

Recent experimental investigations by *Yang et al*. have demonstrated that augmenting the metal layer thickness beneath the DBR structure leads to significantly higher Q-factors when compared to conventional thin metal layers atop a DBR [151]. Moreover, the incorporation of a defect layer

within the DBR arrangement has enabled the observation of Tamm plasmon polaritons (TPPs) with an impressively narrow full-width half-maximum (FWHM) of approximately $2\,nm$ and an exceptional Q-factor of 778 in the near-infrared (NIR) region [152].

Nevertheless, the optical losses incurred in the metal films hinder the practical realization of Tamm structures, adversely impacting the achievable resonance Q-factors. Despite the remarkable advancements witnessed in 1D and 2D Tamm structures, exploring proper 3D Tamm structures holds immense promise for yielding even more remarkable outcomes.

This Thesis addresses this research gap in Article 4, wherein we propose a novel 3D Tamm structure comprising a core-shell SiO_2/Au nanoparticle and a Spherical Bragg Resonator. This innovative design operates in the NIR region, strategically mitigating the absorption losses typically experienced by Au. By exploring the unique properties of this 3D Tamm structure, we seek to contribute to the growing body of knowledge on advanced plasmonic systems and their potential applications.

CHAPTER 3. ARTICLE 1: EXPERIMENTAL CHARACTERIZATION OF SPHERICAL BRAGG RESONATORS FOR ELECTROMAGNETIC EMISSION ENGINEERING AT MICROWAVE FREQUENCIES

Yalina García-Puente, Jean-Jacques Laurin, and Raman Kashyap

Published in: Scientific Reports, November 22, 2023

This work reports experimental investigation and numerical validation of millimeter-sized Spherical Bragg Resonators (SBRs) fabricated using 3D printing technology. The frequency dependencies of the reflection and transmission coefficients were analyzed, and eigenfrequency values were calculated to examine the density of photonic states in air/PLA-polylactide SBRs, showing the appearance of an eigenmode and an increase in the local density of states in the core of a defect cavity. A decay rate enhancement of $\sim 10^2$ was obtained for a dipole placed in the core of the defect SBR. The study also investigated the influence of the source position on the resonator's electromagnetic wave energy. Scattering efficiencies up to order twelve of the multipole electric and magnetic contribution in a 10-layer SBR were calculated to validate the presence of the resonant modes observed in the scattering measurements performed for parallel and perpendicular polarizations. The results demonstrate that SBRs can act as omnidirectional cavities to enhance or inhibit spontaneous emission processes by modifying the density of electromagnetic states compared to free space. This finding highlights the potential of SBRs engineering spontaneous electromagnetic emission processes in various applications, including dielectric nanoantennas, optoelectronics devices, and quantum information, across the entire electromagnetic spectrum.

3.1 Introduction

Over the last few years, the interest in photonic structures with three-dimensional (3D) band gaps created by periodic scattering [2, 3, 153] at optical and longer wavelengths has increased drastically. E. Yablonovitch [154] proposed a 3D collection of spherical holes within a dielectric to attempt creating a photonic band gap. Although the spheres were resonant cavities, they failed to exhibit a band gap, as described in [154]. Meanwhile, hollow core photonic crystal fibers have been extensively used [155], or other “onion skin’’ high contrast optical fiber has also found use in high power transmission of 10-micron radiation [156]. In the cylindrical geometry, “onion skin”

concentric cylindrical layers waveguides have also been demonstrated for mode propagation direction with transverse resonant confinement [157]. The other type of 3D photonic crystals is radial periodic structures, developed in spherical coordinates in the form of spheres with a mutual arrangement of the centers of the multilayer sphere [22, 28, 29]. When the optical thickness of the layers is about a quarter wavelength, the multilayer sphere of alternately high and low refractive index can confine photons within its core. This type of structure is known as Spherical Bragg Resonator (SBR) [23, 24]. The unique property of these SBRs is that the 3D wave function is enclosed in the structure, which could be used to control spontaneous emission [46, 48], to develop a single-photon source [158] or threshold-less lasers [33, 159].

Previous studies have explored the light scattering of SBRs using various theoretical methods [28, 30, 160], such as the plane-wave [161] and finite-difference time-domain methods [162]. More recently, the development of a numerical mode-solving technique called spherical Bessel-Legendre-Fourier space has allowed resonance state frequencies and field profiles to be obtained for any lossy material or dielectric structure with arbitrary characteristics [34]. However, the recursive transfer matrix method developed by A. Moroz [30] has become the most widely used matrix formulation for modeling multilayer spheres. This method offers an analytical solution for the radiative decay rate of a radiating dipole located at any position within a multilayer sphere, its scattering efficiencies, and electromagnetic energy distribution [30, 31, 37]. The accuracy of this method for modeling different spherical multilayer plasmonic structures has been demonstrated in previous works [37, 163, 164]. In particular, we have already used the algorithm to study the engineering quantum dipolar electric or magnetic transitions in the presence of SBR [165]. Moreover, we have explored the potential of SBR to improve the performance of dielectric nanoantennas and for optical amplification and lasing [165].

Currently, the production of SBR is mainly based on conventional techniques requiring clean-room technology, including electron-beam deposition of ZnS/Na_3AlF_6 [38], multistage emulsion polymerization of polystyrene/poly(trifluoroethyl methacrylate) [39], sol–gel and homogeneous precipitation techniques to prepare SiO_2 and Y_2O_3 shells, respectively [40], etching and plasma-enhanced combined with chemical-vapour deposition [33, 41, 42]. A. V. Medvedev et al. [41, 42] fabricated two types of SBR for near-infrared applications. These comprise alternating quarter-wave layers of amorphous hydrogenated silicon carbide (a-$Si_{1-x}C_x$: H), and amorphous silicon

oxide (a-SiO_2) placed over erbium ions doped and undoped glass microspheres [41, 42]. Nevertheless, there is no fully established technique to replicate the deposition of thin layers with homogeneous chemical composition onto a microscopic spherical particle. This lack of a reliable fabrication method has limited the exhaustive experimental characterization of SBRs and their potential applications that have been theoretically envisioned [165].

Dielectric resonators have played an indispensable role in microwave technology due to their renowned ability to provide exceptionally high spectral purity and precise frequency stability [166, 167]. They are essential components in various applications, including microwave sources and filters. The extensive literature on spherical and hollow core resonators underscores their significance, given their capacity to support whispering-gallery modes characterized by extraordinarily high-quality factors (Q-factors) [168-170]. Spherical Bragg Resonators, however, represent a novel development that has opened the door to achieving Q-factors in the microwave domain that can attain or even exceed one million [171-173]. Traditionally, dielectric resonators have been crafted from a diverse range of ceramics and materials. For instance, constructing a Teflon-free space resonator demonstrated a Q-factor of 22 000, primarily limited by the dielectric losses of Teflon [174]. It is worth highlighting that the use of lower-loss materials, such as sapphire, and the strategic incorporation of additional layers have made it possible to achieve higher Q-factors, as documented in the existing literature [172, 174]. Over the past few decades, 3D printing has attracted attention as a versatile and low-cost manufacturing tool for a wide range of applications [175, 176]. The spatial resolution of the 3D printing allows the fabrication of the photonics structure in the microwave frequency range [177-179].

This paper focuses on an experimental investigation and numerical validation of the performance of Spherical Bragg Resonators (SBRs) produced using 3D printing technology. In our study, we examine the dependence of the reflection and transmission coefficients. Furthermore, we calculate the eigenfrequency values to analyze the density of photonic states within the SBRs. We also explore the source position's impact on the resonator's electromagnetic wave energy. Additionally, we determine the scattering efficiencies of the multipole electric and magnetic contribution in a 10-layer SBR up to order twelve ($l = 12$) and compare them with the scattering measurements for parallel and perpendicular polarizations. The findings demonstrate that SBRs can function as a cavity, modifying the density of electromagnetic states compared to free space and enhancing or

inhibiting spontaneous emission processes. The manuscript underlines the potential of SBRs for precisely controlling spontaneous electromagnetic emission processes in various applications, including dielectric nanoantennas, optoelectronics devices, and quantum information systems, covering the entire electromagnetic spectrum. 3D printing technology in SBR fabrication offers a scalable and accessible method for producing these resonators, further expanding their potential for practical applications.

3.2 Results and discussion

Figure 3-1 (a) shows the schematic representation of the investigated spherical Bragg resonator (SBR). This SBR consists of an air spherical core, surrounded by concentric dielectric PLA shells. The multilayered spheres is illuminated by a planar electromagnetic wave and the surrounding medium is air. Figure 3-1 (b) illustrates N-concentric spheroids with each spheroid spaced by a radius increment, $r_{i+1} = r_i + \Lambda_j/2$, where r_{i+1} is the radius of the next outer spheroid, Λ_j is one design factor, i.e. wavelength, selected for each spheroid, with $0 \leq i \leq N$ and $1 \leq j \leq N$. The phase-matching condition for resonance k_B is given by:

$$2n_{eff}\Lambda_p = \lambda_B \tag{4-1}$$

where, n_{eff} is the effective refractive index, and $\Lambda_p = 2(r_{i+1} - r_i)$. Here we have assumed that there is no dependence of the propagation constant with the azimuthal angles, θ and φ.

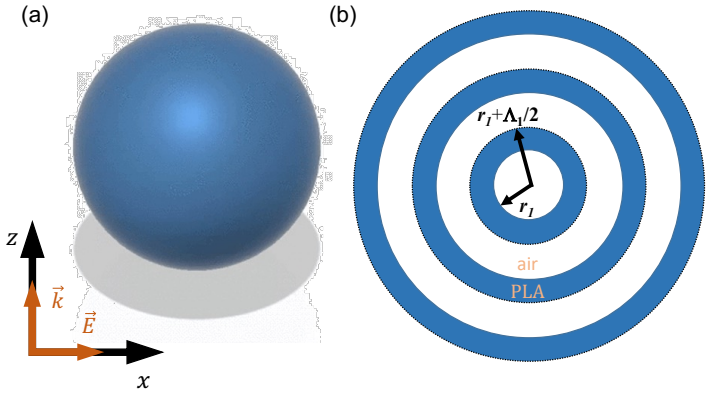

Figure 3-1 (a) Schematic of a Spherical Bragg Resonator excited by a plane wave. (b) Cross section of a Spherical Bragg Resonator r_i represents the radius of the spheroid and Λ_j is some design factor.

In our study, the thickness of each shell $(r_{i+1} - r_i)$ is fixed at about one-quarter of a wavelength $(\lambda_B/4n_i)$, which results in constructive interference of waves reflected from each interface, creating a frequency range known as the band gap, where electromagnetic waves cannot propagate outward from the resonator. The SBR has a spherical symmetry in the radial direction of light propagation, forming an omnidirectional band gap. The wavelength at which the SBR acts as an omnidirectional Bragg reflector is defined as the center of the band gap, denoted as λ_B.

3.2.1 Reflectance spectra and local density of states

Photonic bandgap in 3D-printed PLA-polylactide (PLA) [180] SBRs were studied by placing a dipole antenna at the center of the 3D photonic crystal. The methodology section includes a schematic representation of the SBRs considered in this work. Reflectance measurements shown in Figure 3.2 (a) and (d) were taken for air/PLA spherical Bragg resonators with varying layer numbers, $n_l = 10$ and $n_l = 6$. These resonators have Mie size parameters of $2\pi R/\lambda_B = 14.16$ and 9.12, and an air core radius of $r_{core} = \lambda_B/4n_{core}$ with Bragg frequency $f_B = c/\lambda_B = 25\ GHz$, where c is the speed of the light and R the outermost radio. In both cases, we obtained frequency ranges where the reflectance is maximal, corresponding to the photonic stopband. The results revealed that the periodic layering of alternating air and PLA materials in the SBR led to partial reflection of the incident electromagnetic wave at each spherical boundary. The constructive interference of the reflected waves at a frequency approximately four times the optical thickness of the concentric spherical shells resulted in the concentric spherical layers acting as mirrors. Therefore, the increase in coatings resulted in higher maximum reflectance. This observation can be attributed to the fact that more air/PLA spherical layers led to more significant constructive interference of the reflected waves, which enhanced the reflectance. Due to the 3D printer constraints, our study was limited to SBRs with $n_l = 10$ and $n_l = 6$. However, based on observations in the planar case [156], when the reflector contains more than $n_l = 10$ layers, it is anticipated that radiation within this wavelength range would be unable to propagate outward from the resonant structure.

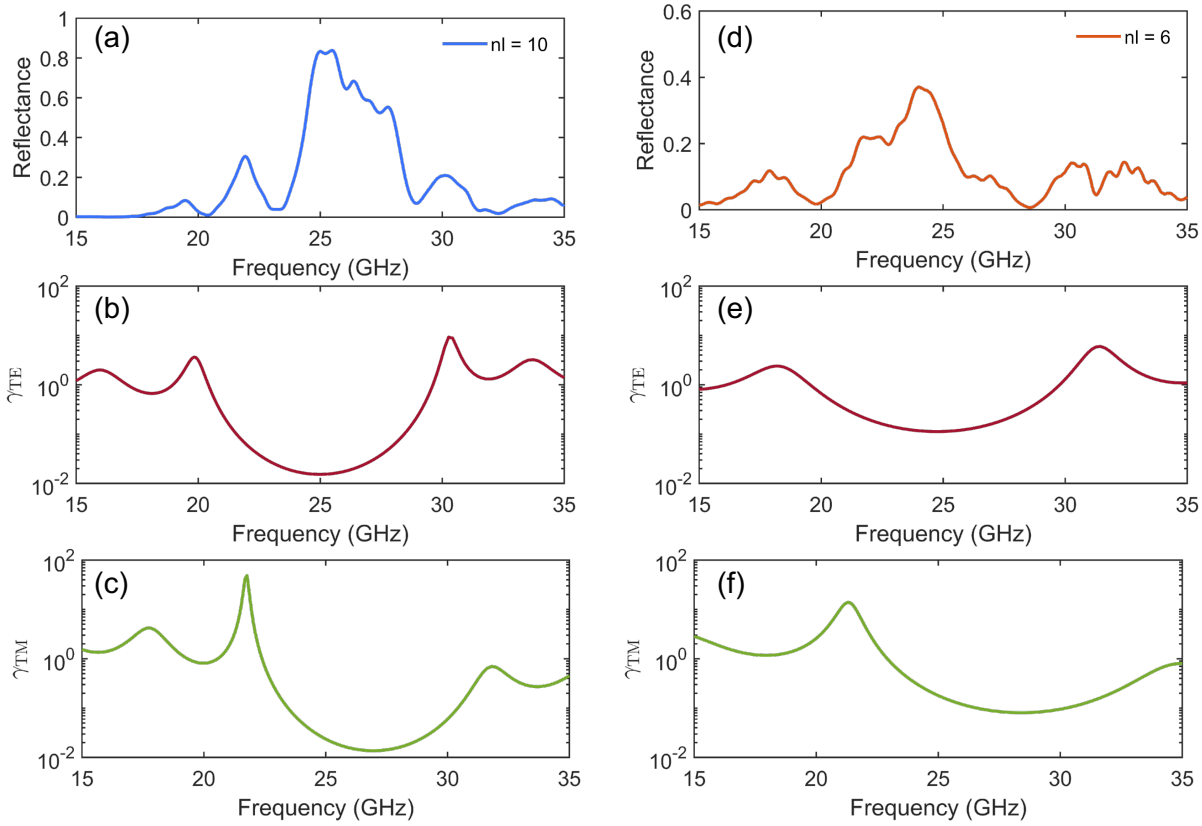

Figure 3.2 Measured reflectance spectrum of SBRs with a different number of layers, (a) $n_l = 10$ and (d) $n_l = 6$, at the core of the structure. Calculated dipolar spontaneous emission decay rate γ for the transversal electric (b) and (e) and transversal magnetic (c) and (f) polarizations. In both geometries, the SBR band gap's center is fixed at $f_B = 25\ GHz$, and the core radius is $r_{core} = \lambda_B/4n_{air}$.

Recent studies have explored various photonic structures, including *woodpile* and *inverse opal*, and demonstrated that the local density of photonic states increases within the eigenmodes of the cavity and at the boundaries of the photonic bandgap [181-183]. Our study focuses primarily on the decay rate of the spontaneous emission of an active atom placed at the core of the SBRs, which is proportional to the local density of states [77]. Specifically, we calculated a dipole's spontaneous emission decay rate for transverse electric (γ_{TE}) and transverse magnetic (γ_{TM}) polarizations.

To better understand the relationship between the photonic bandgap and dipolar emission behavior, we studied the spectral distribution of the radiative decay computed for SBRs with band gap's center fixed at $f_B = 25\ GHz$, $n_l = 10$ and $n_l = 6$, and the core radius $r_{core} = \lambda_B/4n_{air}$. The

calculated dipolar spontaneous emission decay rate is shown in Figure 3.2 (b) and (e) for the TE polarization and in Figure 3.2 (c) and (f) for the TM polarization. As noted, the states' density decreases to zero within the photonic bandgap region, resulting in emission suppression. However, at the edges of the forbidden bandgap, the density of states increases substantially, leading to an increase in dipolar emission at the corresponding wavelengths. In the next section, we will analyze how defects in the resonator create eigenmodes in the core of the cavity and, consequently, an increase in the local density of states. Our results suggest that these structures permit control and enhance light-matter interactions in various applications, including sensing and energy harvesting.

3.2.2 Geometrical and spatial dependence of the resonant modes

Figure 3-2 (a) displays the reflection (R) and transmission (T) spectrum measured for a 10-layer air/PLA SBR with a core radius of $r_{core} = \lambda_B/4n_{air}$. The reflection spectrum was recorded from the center of the SBR, showing an omnidirectional bandgap centered at around 11 GHz. To measure the transmitted power, a horn antenna was placed near the surface of the SBR. The recorded reflectance spectrum reveals that the maximum reflectance position coincides with the minimum of the transmitted power recorded.

To confirm the validity of our experimental results, we conducted a numerical comparison of the measured reflection spectrum of the SBR (Figure 3-2 (a), black dotted line). As has been demonstrated before [175], the SBR reflection coefficient is influenced by the polarization of the spherical wave (TE and TM) and its angular modal number (l) while being independent of the azimuthal modal number (m). Therefore, the omnidirectional photonic bandgap overlaps all partial bandgaps for the spherical waves of all polarizations with all angular modal numbers. Upon comparison of the experimental and numerical reflection spectra, we found that the maximum values of both spectra coincide. However, the measured bandgap width was narrower than the predicted values. Additionally, we observed some high reflection near 8 GHz, which can be attributed to the presence of spherical modes of higher order with different angular modal numbers when the core radius approaches the order of the wavelength used, as has been previously discussed by other researchers [160, 184].

As previously mentioned, the density of photonic states experiences a significant increase within the eigenmodes of the cavity and at the boundaries of the photonic bandgap. Different methods

have been proposed to calculate the eigenmode of resonant structures [185, 186], in these works we applied a Weierstrass factorization [187] to the scattering matrix elements of a 10-layer SBR. The notable advantage of this semi-analytical approach lies in its ability to yield the eigenfrequencies of our structure independently for each order rather than as a composite of the supported resonances. Importantly, it straightforwardly achieves this without requiring additional fitting parameters or coupling factors, as is often the case with coupled oscillator models [177]. In Figure 3-2 (b) and (c), the calculated poles and zeros of the SBR scattering matrix for two different core radii ($\lambda_0/2n_{air}$ and $\lambda_0/4\,n_{air}$) are represented by square and diamond symbols, respectively. The pole-zero map frequencies for the TE and TM polarizations are normalized by $f_0 = 1\,GHz$. By performing the factorization, we obtained the singularities of the SBRs. The zeros correspond to perfect absorption, while the poles represent the eigenfrequency.

The results show no eigenmodes in the bandgap region of the SBR with a core radius of $r_{core} = \lambda_B/4n_{air}$. This agrees with suppressing the decay rate in the bandgap region previously observed in Figure 3.2. However, a localized photonic state can be created within the bandgap in the presence of a disorder, like a localized defect in an SBR with a core radius of $r_{core} = \lambda_B/2n_{air}$. For this case, the SBR acts as a defect optical cavity in which the surrounding spherical layers act as a mirror in all directions. These have been the primary research focus in photonic crystal emission modification [47, 48]. For instance, we have previously proposed a defect Er^{3+} core doped Si/SiO_2 SBR for optical amplification and lasing [165].

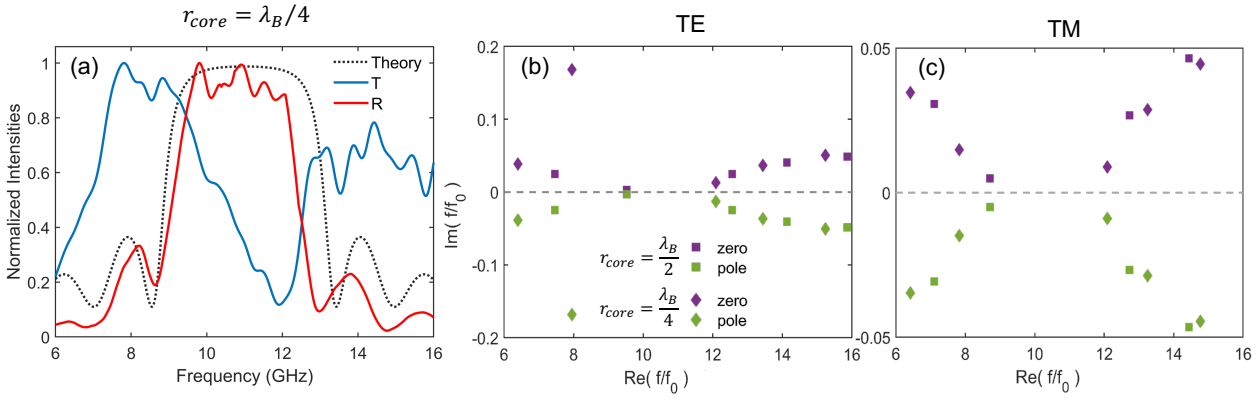

Figure 3-2 (a) Experimental and calculated reflectance spectrum at the center of an SBR with $n_l = 10$ plotted in solid red and black dotted lines, respectively. Experimental transmitted power

measured near the SBR surface was plotted in a solid blue line. All spectra are normalized to the maximum reflection coefficient. The SBR band gap's center is fixed at $f_B = 11\ GHz$, and the core radius is $r_{core} = \lambda_B/4n_{air}$. (b) Calculated poles and zeros of the SBR scattering matrix for two different core radii $r_{core} = \lambda_B/2n_{air}$ and $r_{core} = \lambda_B/4n_{air}$ represented as square and diamond symbols, respectively. The pole-zero map frequencies are normalized by $f_0 = 1\ GHz$.

One essential part of our study of the SBR performance was to investigate the electromagnetic field localization inside the multilayer spheres. The radial distribution of the normalized electromagnetic energy for a defect 10-layer air/PLA SBR with $r_{core} = \lambda_B/2n_{air}$ as a function of frequency is shown in Figure 3-3 (a). As can be seen, the map depicts the location of the electric field within the different layers marked by white lines. A maximum value is observed at the defect mode of the resonator system ($f \approx 9.55\ GHz$) in concordance with the eigenfrequency value depicted in Figure 3-6 (a). The maxima located in the core are the main modes and are of the Fabry–Pérot type and those located in the layers are of the whispering gallery mode type and are of higher order.

On the other hand, we calculated the total perpendicular and parallel decay rate components of a dipole at $f \approx 9.55\ GHz$ (circular symbol) and $f \approx 11.35\ GHz$ (triangular symbol) as a function of the position along the SBR core, as shown in Figure 3-3 (b). These frequencies can be identified as maximum electromagnetic energy in the SBR core (see Figure 3-3 (a)) and correspond to two distinct eigenfrequencies, the independently estimated order or angular quantum numbers $l = 1$ and $l = 2$. Further details are in Figure 3-6 (a) and (c). We observed that the decay rate for the dipole at the main resonant frequency or defect mode frequency ($f \approx 9.55\ GHz$) is several orders of magnitude higher than that of a dipole outside at the edge of the bandgap ($f \approx 11.35\ GHz$). However, the decay rates become closer as the dipole is moved away from the center. Additionally, we observed a divergence of the transverse and perpendicular components due to the breaking of the spherical symmetry when we moved out of the center of the core. The minor shift in the decay rate of the dipole at the principal resonant frequency is worth noting, which provides us with flexibility when designing practical devices.

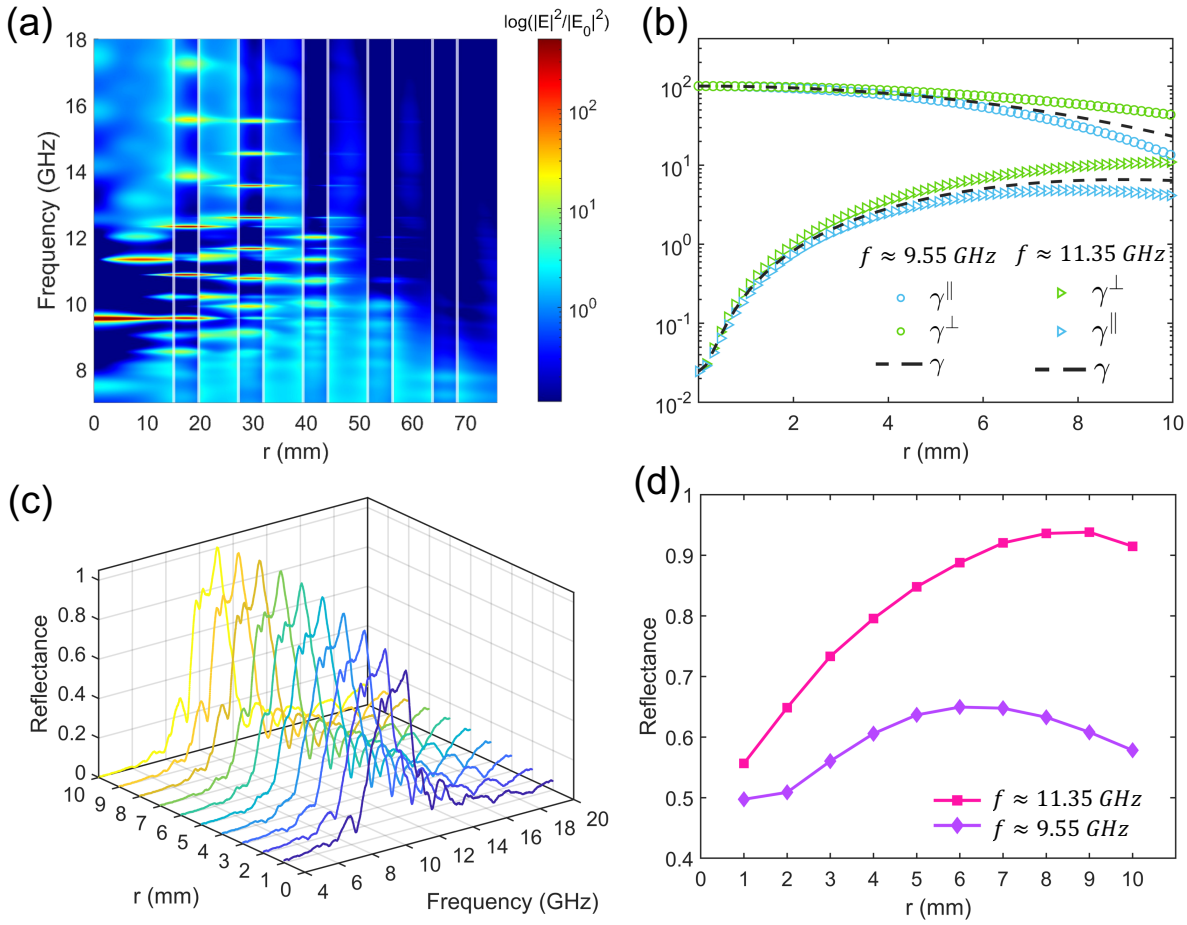

Figure 3-3 (a) Spatial distribution of the normalized electric field intensities of a 10-layer SBR with $r_{core} = \lambda_B/2n_{air}$ as a function of the frequency. (b) Calculated total, perpendicular, and parallel decay rate components of a dipole at $f \approx 9.55\,GHz$, circular symbol, and $f \approx 11.35\,GHz$ triangular symbol as a function of the position along the SBR core. (c) Reflectance measurement at different points along the SBR core radius. (d) Reflectance measured at $f \approx 9.55\,GHz$ and $f \approx 11.35\,GHz$ at different points of the SBR core.

Furthermore, to support the theoretical results discussed above, we experimentally investigated the reflectance properties of a 10-layer SBR air-PLA with a Bragg frequency of 10 GHz and a core radius of $r_{core} = \lambda_B/2n_{air}$. It represents the portion of the reflected electromagnetic wave energy relative to the total energy of the incident electromagnetic wave. The reflectance measurements were made at different points along the core radius from 10 mm (near the inner PLA layer) to 1 mm (around the core center), and the results are shown in Figure 3-3 (c). As expected, an

omnidirectional stopband was obtained due to the constructive interference of the reflected waves at each boundary of the spherical shell. However, we observed that when the antenna was near the center, the maximum reflectance was less than one due to the transmission of electromagnetic energy to the outermost layers and the surrounding medium.

In addition to the omnidirectional stopband, we observed eigenmodes in the SBR. Figure 3-2 (b) and (c) showed the calculated poles and zeros of the SBR scattering matrix, indicating one defect mode inside the cavity band gap and another eigenmode at the edge of the band gap. We measured the reflectance intensity at the eigenfrequencies $f = 9.55\,GHz$ GHz and $f = 11.35\,GHz$ at different points along the radius of the SBR core, as shown in Figure 3-3 (d). Interestingly, we observed peaks in the reflectance intensity at these frequencies, which corresponded to the modes observed in the electromagnetic energy map. Furthermore, we observed that the reflectance intensity tended to increase as we moved away from the center of the SBR core. This trend was more noticeable at the frequency of $f = 11.35\,GHz$, which is consistent with the behavior of the decay rate observed before. This behavior may be because this mode is mostly located in the core of the SBR close to the PLA layer.

3.2.3 Theoretical and experimental scattering

This study uses theoretical calculations and experimental measurements to investigate the resonant modes of a 10-layer SBR with a core radius $r_{core} = \lambda_B/4n_{air}$. Theoretical calculations based on T-matrix coefficients show that the SBR exhibits resonant modes of the whispering gallery type, reflected in the calculated total scattering efficiencies (Q_{sca}) shown in Figure 3-4. The peaks in the Q_{sca} correspond to the resonant modes of the SBR and provide valuable information about its electromagnetic properties.

To further investigate the resonant modes, we analyze the spatial distribution of the electric field intensities as a function of frequency, as shown in Figure 3-4 (b). The results show that the electric field intensities are maximal at the resonant modes' frequency. In particular, three maxima can be identified in the outermost layer of the SBR, corresponding to resonant modes of the whispering gallery type. These results agree with the calculated scattering efficiencies.

In order to validate the theoretical calculations, we perform experimental measurements of the scattering from the SBR using far-field monostatic measurements. The results, shown in Figure 3-4 (c), confirm the presence of the resonant modes and the corresponding maxima in the scattering measurements. The SBR was excited by a P-polarized (parallel) and S-polarized (perpendicular) plane wave, and the results were similar in both cases, indicating the spherical symmetry of the SBR. The study of whispering gallery modes in the outermost layers of the SBR has important implications for potential applications in photonics and electronics. The ability to propagate electromagnetic energy through adjacent SBRs could be used to buffer or delay electromagnetic pulses more efficiently than with more conventional coupled resonators.

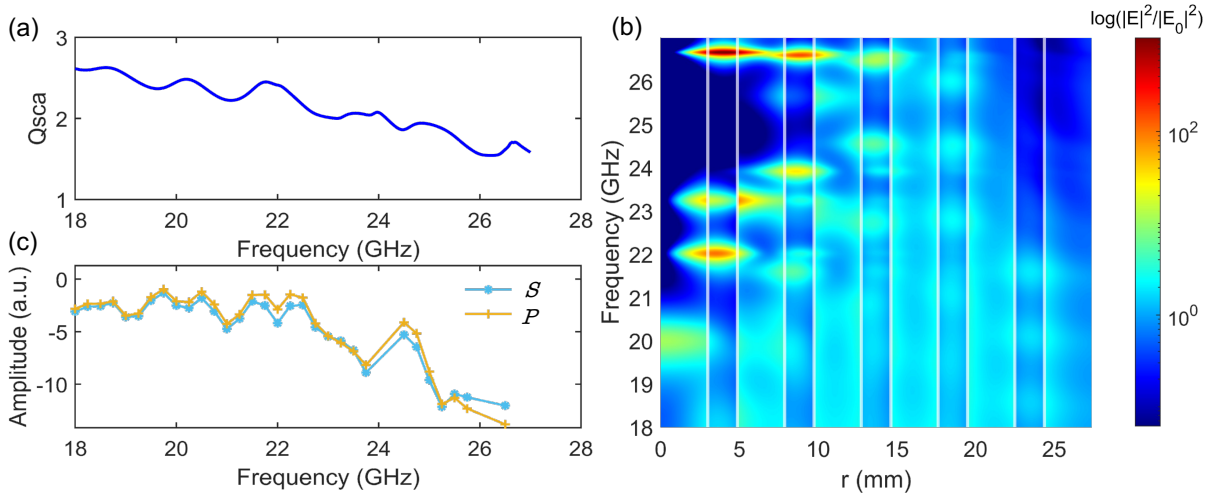

Figure 3-4 (a) Calculated total scattering efficiencies Q_{sca} for a 10-layer SBR up to order twelve of the multipole electric and magnetic contributions. (b) Spatial distribution of the normalized electric field intensities of a 10-layer SBR with $r_{core} = \lambda_B/4\, n_{air}$ as a function of the frequency, the PLA layers are represented by white lines. (c) Scattering measurements of a 10-layer SBR for the S and P polarization.

This work provides valuable insights into the electromagnetic properties of SBRs. The SBR can be scaled from nanometers to millimeters simply by changing the absolute dimension, making it possible to use it as a resonant cavity across the electromagnetic spectrum, particularly at optical, microwave, and, potentially, acoustic frequencies. In a broader sense, the concentric shells can be ellipsoids or any other arbitrary geometric structure.

The first importance of an SBR is achieving a complete photonic crystal property with a 4π full bandgap, which is challenging to attain in Cartesian systems without significant refractive index

contrast. In contrast, the k-vector varies with direction in Cartesian coordinates, causing dispersion. However, in an SBR, a point source at the center results in all radiation being incident normally on the concentrical spheroidal surfaces, preventing the directional change of the k-vector and suppressing the emission radiation, thus increasing the cavity's radiative lifetime with a high-quality factor. An infinite range of structures with various characteristics can be produced through the creation of local defects or the addition of specific materials like gases and nonlinear or active materials, allowing the implementation of directional loss or disorder. As a result, SBR lasers, masers, or "Rfasers" with true omnidirectional emission could be developed as we previously demonstrated.

3.3 Conclusions

This paper comprehensively investigates millimeter-sized Spherical Bragg Resonators (SBRs) using 3D printing technology. The frequency dependencies of the reflection and transmission coefficients and the density of photonic states in the SBRs were examined through experimental and numerical analysis. Additionally, the influence of the source position on the resonator's electromagnetic wave energy was investigated. The study also determined the scattering efficiencies of the multipole electric and magnetic contributions of a 10-layer SBR, and scattering measurements were taken for parallel and perpendicular polarizations. The results indicate that SBRs can significantly alter the density of electromagnetic states compared to free space, making them useful for enhancing or inhibiting spontaneous emission processes. The potential applications of SBRs include dielectric nanoantennas and optoelectronics devices across the entire electromagnetic spectrum. Overall, this work offers valuable insights into the development of new and innovative technologies based on SBRs, and paves the way for future research in this field.

3.4 Methods

The theoretical analysis of the SBRs studied in this work was performed with a fast transfer-matrix method developed by Moroz et al. [30]. The feasibility of this fast and versatile method to study plasmonic and dielectric multilayered spherical nanostructures has been widely demonstrated. From the T-matrix, the scattering efficiency Q_{sca} at each multipole l and diagonal component p was obtained from the following expression [30, 37]:

$$Q_{sca} = \frac{1}{(rk)^2}\sum_{p,l}(2l+1)\left|T_{pl}\right|^2 \quad 4\text{-}2$$

where r is the radius of the SBR and k is the wave vector.

Also, through the Weierstrass factorization [188] of each transverse electric (TE) and transverse magnetic (TM) component of the S-matrix ($\bar{\bar{S}} \equiv \bar{\bar{I}} + 2\bar{\bar{T}}$, where $\bar{\bar{I}}$ is the identity matrix) is possible to obtain the eigenvalues of the SBRs as we depicted in [165].

The electric field was calculated by the recursive transfer method, as is well described in [31]. While the normalized decay rate of a dipole is given by:

$$\gamma_{\perp} = \frac{3}{2x_d^4}\frac{n_d}{n_h}\sum_l l(l+1)(2l+1)|f_{El}(x_d)|^2 \quad 4\text{-}3$$

$$\gamma_{\parallel} = \frac{3}{4x_d^4}\frac{n_d}{n_h}\sum_l (2l+1)[|f_{Ml}(x_d)|^2 + |f'_{El}(x_d)|^2] \quad 4\text{-}1$$

The symbols "⊥" and "∥" refer to the dipole's perpendicular and parallel orientations (with respect to the z-axis) at position d, respectively. The prime symbol denotes differentiation with respect to the argument. Additionally, n_h denotes the refractive index of the host medium, l represents the angular quantum number, and $f_{\mathrm{El,Ml}}(\mathrm{x_d})$ represents linear combinations of Riccati-Bessel functions. The dimensionless size parameter $\mathrm{x_d}$ is defined as $\mathrm{x_d} = k_{\mathrm{d}} r_{\mathrm{d}}$ where $k_{\mathrm{d}} = 2\pi n_{\mathrm{d}}/\lambda$.

3.4.1 SBR fabrication and experimental measurements

Figure 3-5 (a) shows the SBRs fabrication process using Value PLA-polylactide (PLA) [180] via 3D printing using an Original Prusa i3 MK3 with a resolution of $0.05\ mm$. PLA is characterized by a dielectric constant around 2.75 ± 0.05 and loss tangent $(1.1 \pm 0.2) \times 10^{-2}$ in the microwave range [189]. The process involved depositing a thin rod followed by the outermost semi-spheroid shell, then extending the rod and adding the next inner semi-spheroid. In this study, an air gap was used to imitate the neighboring semi-spheroidal shell, but another material could be deposited to alter the refractive index. The thicknesses of the air and PLA shells were equivalent to a quarter of the optical length $\lambda_B/4\,n_{air}$, where λ_B represents the center of the stop band and n is the refractive index of the air or PLA. As a result, the dimensions and periodicity of the concentric spheres determined the resonance frequencies. The process was repeated until all semi-spheroidal shells were deposited, creating the innermost spheroid and outermost shell, resulting in the final SBR.

This study considers SBRs 3D printed with core radiuses of $\lambda_B/4$ and $\lambda_B/2$, using five and three concentric spherical dielectric PLA layers spaced by air. The center of the stop band was fixed at 10 GHz and 25 GHz.

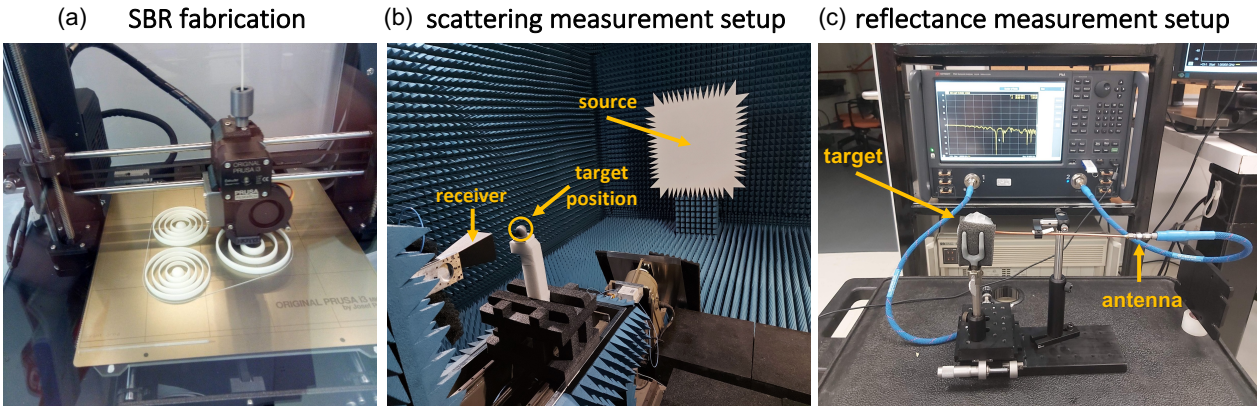

Figure 3-5 (a) SBR fabrication by 3D printing in PLA. Different sizes of 3D-printed. (b) Scattering and (c) reflectance measurement setup.

Keysight's network analyzer N5224B was used to measure the antennas' reflected and transmitted voltage signal. The operating frequencies are from 10 MHz to 43.50 GHz. Port 1 was connected to a coax cable PE-118SR through an SMA-K connector to lead the signal up to the center of the SBR. Measured $|S_{11}|$ parameters of SBRs with a different number of layers ($n_l = 10$ and $n_l = 6$) are shown in Figure 3-8. In addition, the SBR was mounted on a mobile station to adjust the antenna's position with respect to its center, as shown in Figure 3-5 (c). With this configuration, we obtained the magnitude of the reflected voltage signal $|S_{11}|^2$. Port 2 was connected to a horn antenna for the transmission measurements to estimate the magnitude of transmitted signal $|S_{21}|^2$ close to the SBR surface.

To extract the scattered electric field of the SBR from 18 GHz to 26 GHz, we conducted far-field monostatic measurements in an anechoic chamber. Figure 3-5 (b) illustrates our configuration within the anechoic chamber. The SBR under test was positioned on a post, and a plane wave illuminated the target. The setup enables us to measure the amplitude of the scattered electric field. Our measurements covered both polarizations, S and P. The S polarization corresponds to the electric field being perpendicular to the plane containing the SBR, source, and receiver. In contrast, the P polarization corresponds to the case where the electric field is parallel. To switch between

the two polarizations, the source, and receiver were mechanically rotated by 90°. We utilized a robust polyurethane foam as the base material to minimize absorption and achieve the lowest possible refractive index [190].

3.5 Funding

Natural Sciences and Engineering Research Council of Canada (Discovery grants, Strategic Research grants).

3.6 Acknowledgments

R. Kashyap acknowledges financial support for the Canadian NSERC Discovery grants and Strategic Research grants programs.

3.7 Author contributions

Y. G.- Formal Analysis, Investigation, Methodology, Writing – original draft, Modeling using MATLAB; J. L.- Conceptualization, Review & editing; R. K.- Conceptualization, Resources, Supervision, Review & editing.

3.8 Disclosures

The authors declare no conflicts of interest.

3.9 Data availability

Data underlying the results presented in this paper are not publicly available at this time but may be obtained from the authors upon reasonable request.

3.10 Supplementary Information

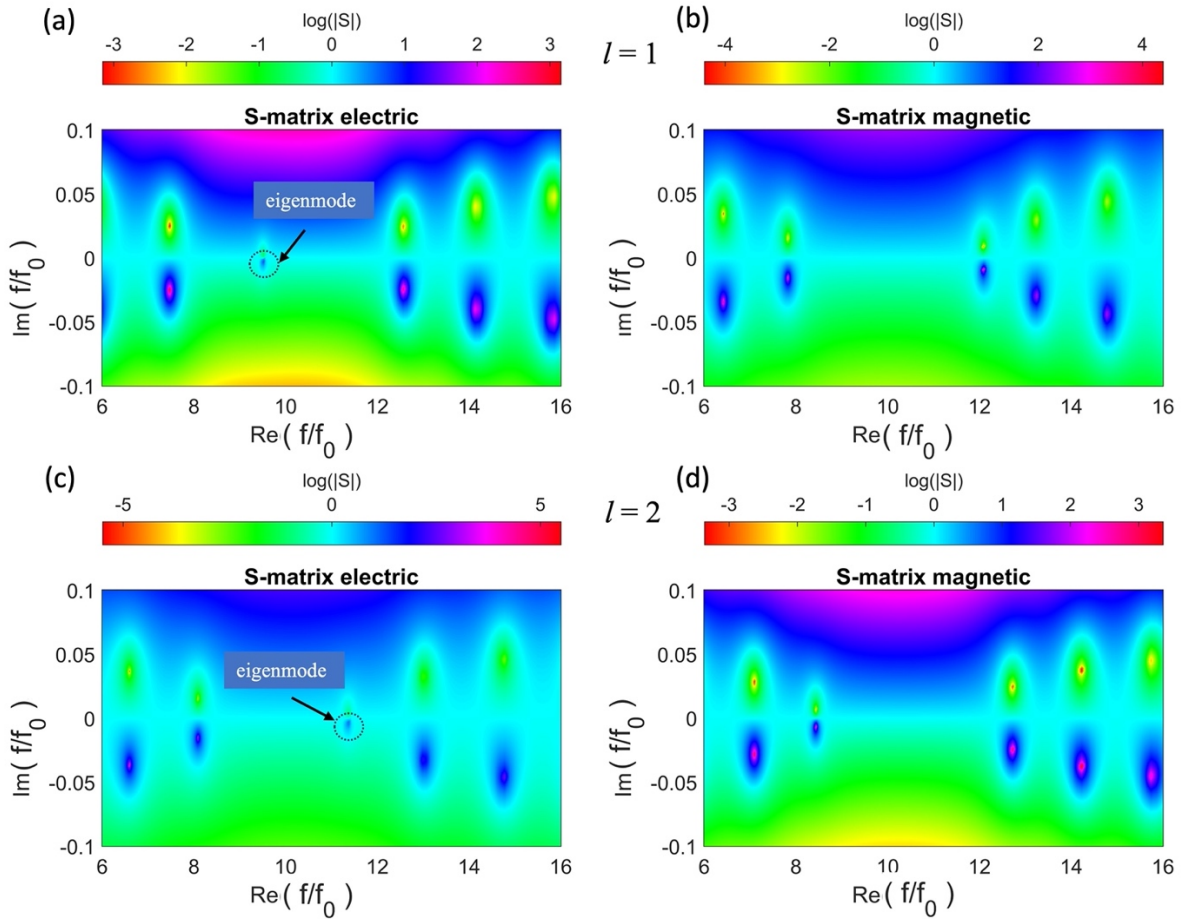

Figure 3-6 Calculated maps of the S_{pl} matrix component in the complex frequency plane for (a) TE1, (b) TM1, (c) TE2 and (d) TM2 in 10-layer SBR air-PLA with a Bragg frequency of 10 GHz and a core radius of $r_{core} = \lambda_B/2n_{air}$.

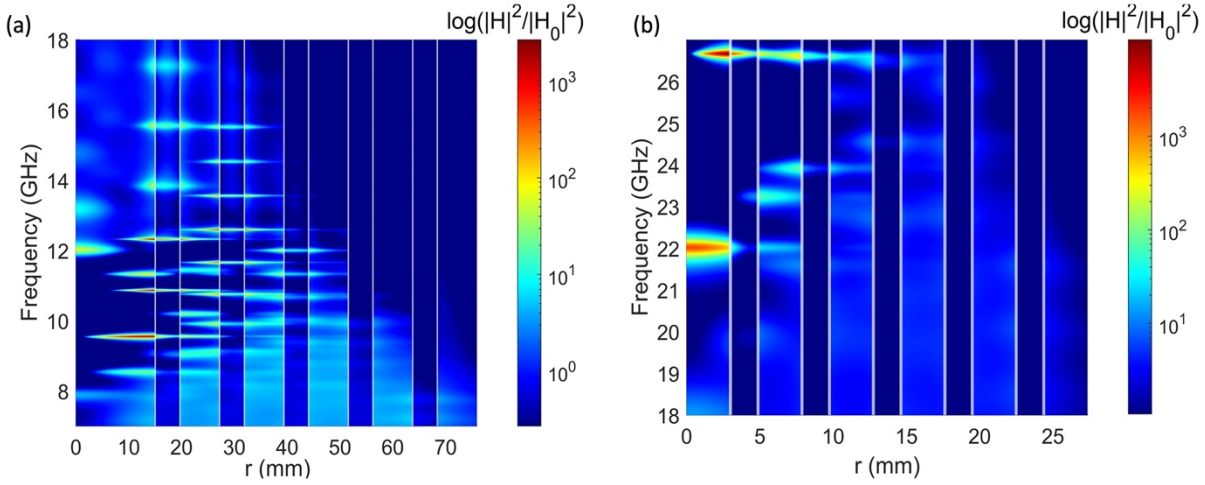

Figure 3-7 Spatial distribution of the normalized magnetic field intensities of a 10-layer SBR with (a) $r_{core} = \lambda_B/2n_{air}$ and (b) $r_{core} = \lambda_B/4\,n_{air}$ as a function of the frequency, the PLA layers are represented by white lines.

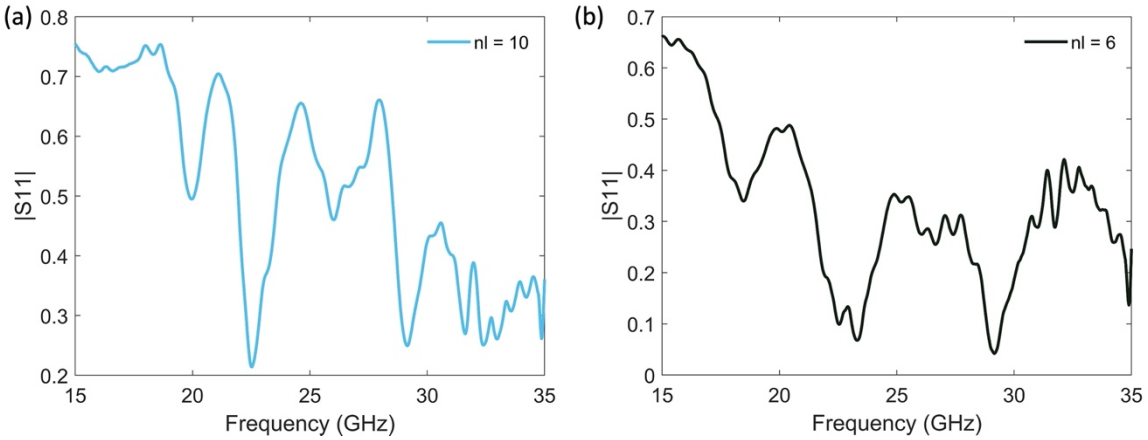

Figure 3-8 Measured $|S_{11}|$ parameters of SBRs with a different number of layers, (a) $n_l = 10$ and (d) $n_l = 6$, at the core of the structure.

CHAPTER 4. ARTICLE 2: SPHERICAL BRAGG RESONATORS FOR LASING APPLICATIONS: A THEORETICAL APPROACH

Yalina García-Puente and Raman Kashyap

Published in: Optics Express, December 19, 2022

This work considers a perfect 3D omnidirectional photonic crystal; Spherical Bragg Resonators (SBR), for lasing applications. We use the recursive transfer matrix method to study scattering in an Er^{3+} doped SBR. We find the threshold gain factor for lasing by scanning poles and zeros of the S-matrix in the complex frequency plane. For a six Si/SiO_2 bilayer SBR, the threshold gain factor corresponds to a dopant density of Er^{3+} of $5.63 \times 10^{20}\ ions/cm^3$. We believe, our work is the first theoretical demonstration of the ability to engineer optical amplification and threshold gain for lasing in SBRs.

4.1 Introduction

Photonic crystals are structures based on a periodic arrangement of dielectric materials. They have been widely used to confine and control light by introducing defects or light emitters inside the photonic bandgap [7, 191]. The dimensions of a photonic crystal are linked to the number of directions in which the refractive index changes. Therefore, an array of concentric spheres constitutes a 3D photonic crystal [22, 28, 29, 180]. Confinement of photons in the core is possible for a multilayer sphere array of alternating high and low refractive indexes with an optical thickness of the layers of about one-quarter wavelength. This structure is a Spherical Bragg Resonator (SBR), also known as the Bragg onion resonator [22, 28, 33]. The SBR has excellent potential as a tridimensional photonic crystal with a high-quality factor Q $\sim 10^6$ and small modal volume V$\sim(\lambda/n)^3$ [23, 24]. These resonators are of great interest for applications that demand a large spontaneous emission factor, like single-photon sources [158] or threshold-less lasers [46, 48].

The light-scattering properties of SBRs have been studied theoretically with different numerical methods and matrix formulations [22, 24, 28]. Furthermore, an efficient numerical model called Spherical space Bessel-Legendre-Fourier has been developed for any lossy material or dielectric structure with arbitrary geometric [34]. This method provides the analyzed structure's resonance state frequencies and field profiles. However, the recursive transfer-matrix algorithm developed by

A. Moroz [30] has been the most widely used in recent years. This algorithm is computationally attractive due to the simplicity of the implementation, reliability, and computational efficiency [37]. Furthermore, the method presents a general solution for fundamental cross-sections, orientation-averaged electric and magnetic field intensities and the radiative decay rate of a dipole placed at any arbitrary position in a multilayer sphere. The algorithm has successfully addressed different light scattering problems in multilayer spheres using proper combinations and manipulations of the transfer matrices [35-37].

On the other hand, incorporating a gain or active media in a resonator opens an avenue for improving existing applications like on-chip resonators for lasing [192] or sensing [193] and even new ones. In addition, the promise of using SBRs for spontaneous emission engineering [29, 48] has also been suggested. However, a comprehensive study of the conditions to achieve such optical amplification by introducing a gain media at the core of these Bragg onion resonators are still missing.

This work presents a theoretical approach to the electromagnetic properties in Si/SiO_2 SBRs with a variable number of layers. We estimated the multipole scattering efficiencies by a recursive transfer matrix method [30, 37]. The Weierstrass factorization [188] of the S-matrix in the complex frequency plane is used to find the perfectly emitting (poles) and absorbing (zeros) structure modes. We exhaustively study how modifying the Er^{3+} ion concentration as a gain media in the SiO_2 core affects the localization of the poles and zeros in the frequency plane. The relationship of Er^{3+} ion concentration and the structure modes are used to engineer optical amplification and threshold gain for lasing in SBRs.

These resonators can be fabricated with precise control of the spherical layers' thickness and chemical composition by plasma-enhanced chemical vapor deposition (PECVD) technique and others [33, 41, 42]. Therefore, we believe this work can be a reference for the future fabrication of SBRs that can be used for threshold-less laser applications.

4.2 Theory of light scattering

The spherical Bragg resonator (SBR) studied is shown schematically in Figure 4-1. This SBR consists of a low refractive index spherical core surrounded by alternating concentric dielectric

shells with different refractive indices. The shells have an optical thickness of about one-quarter wavelength ($\lambda/4$) to produce constructive interference of waves reflected from the interfaces of each surface. This frequency range, where electromagnetic waves are not allowed to propagate outward from the resonator, is known as the band gap. As a result of the spherical symmetry of the SBR in the radial direction of light propagation, an omnidirectional band gap is created. The center of the bandgap, where the SBR acts as an omnidirectional Bragg reflector, is defined by the wavelength, λ_B. The system is illuminated with a plane electromagnetic wave, and the host medium is air. The gain medium is located in the SiO_2 core of the onion resonator.

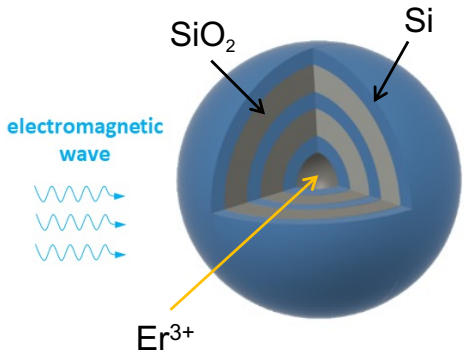

Figure 4-1 Schematic of an Er^{3+} core-doped Spherical Bragg Resonator with Si/SiO_2 multilayers.

The scattering properties of Spherical Bragg Resonator (SBR) can be characterized by the S or T matrices [112]. In our case, we use a rigorous and computationally fast transfer-matrix method, and the well know relation between the T-matrix and the definition of the S-matrix [112] to obtain the appropriate expressions for the S-matrix coefficients:

$$\bar{\bar{S}} \equiv \bar{\bar{I}} + 2\bar{\bar{T}} \qquad 4\text{-}1$$

where $\bar{\bar{I}}$ is the identity matrix.

4.2.1 Decay rate

This transfer matrix can be used to estimate the Purcell factor ($P = \Gamma/\Gamma_0$) in multilayer spheres where the normalized radiative decay rate of a dipole placed at the core center is given by [30]:

$$\frac{\Gamma_\perp}{\Gamma_0} = \frac{3}{2x_d^4}\frac{n_d}{n_h}\sum_l l(l+1)(2l+1)|f_{El}(x_d)|^2 \qquad 4\text{-}2$$

$$\frac{\Gamma_{\parallel}}{\Gamma_0} = \frac{3}{4x_d^4}\frac{n_d}{n_h}\sum_l (2l+1)[|f_{Ml}(x_d)|^2 + |f'_{El}(x_d)|^2] \quad 4\text{-}3$$

Where "⊥" and "∥" correspond to the perpendicular and parallel orientation of the dipole located at position d, n_h is the refractive index of the host medium, l is the angular quantum number, and $f_{\mathrm{El,Ml}}(\mathrm{x_d})$ are linear combinations of Riccati-Bessel functions, while the prime represents the differentiation with respect to the argument. The dimensionless size parameter is defined by $\mathrm{x_d} = k_{\mathrm{d}} r_{\mathrm{d}}$ where $k_{\mathrm{d}} = 2\pi n_{\mathrm{d}}/\lambda$.

In addition, the modal volume V of a multilayer sphere can be calculated from the quality factor $Q = \omega_0/\Delta\omega$ and Purcell factor [33, 54].

$$P = \frac{3}{4\pi^2}\frac{Q}{V}\left(\frac{\lambda_0}{n_c}\right)^3 \quad 4\text{-}4$$

where $\Delta\omega$ is the full width at half maximum of the normalized radiative decay, ω_0 and λ_0 are the mode frequency and wavelength respectively, and n_c is the refractive index of the SBR's core.

4.2.2 Scattering, absorption, and extinction efficiencies

Our structures have a spherical geometry, which can be treated as the deconvolution of electric and magnetic multipoles of order *l*, in spherical coordinates. Therefore, the S-matrix is diagonalized. Consequently, S-matrix fully describes the scattering process for each multipole *l* and diagonal component, *p*. For our calculations, we apply the Weierstrass factorization to each component *p* (Transverse Electric and Transverse Magnetic) to decompose the *S*-matrix [188]:

$$S_{pl}(\omega) = Aexp(iB\omega)\prod_m \frac{\omega-\omega_{pl;m}^{+zero}}{\omega-\omega_{pl;m}^{-pole}} \quad 4\text{-}5$$

$$\omega_{pl;m} = \Re(\omega_{pl;m}) + i\Im(\omega_{pl;m}) \quad 4\text{-}6$$

where A and B are constants and $\omega_m^{+zero/-pole}$ the resonant frequencies with real and imaginary parts denoted by $\Re$ and $\Im$, respectively.

The eigenvalues of the *S*-matrix correspond to two singularities: poles and zeros [194]. The poles represent the eigenmodes, while the zeros are associated with a perfect absorption [194]. The position of poles and zeros allows to describe the scattering properties of the system under consideration [188].

Also, the total scattering, absorption, and extinction efficiencies (denoted by the abbr. subscripts, *sca*, *abs* and *ext*, respectively) can be obtained from the S or T matrices:

$$\Omega_{sca} = \frac{1}{2(rk)^2}\sum_{p,l}(2l+1)\left|S_{pl}-1\right|^2 \quad 4\text{-}7$$

$$\Omega_{abs} = \frac{1}{(2rk)^2}\sum_{p,l}(2l+1)\left|1-S_{pl}\right|^2 \quad 4\text{-}8$$

$$\Omega_{ext} = \frac{1}{(rk)^2}\sum_{p,l}(2l+1)\Re\left(1-S_{pl}\right) \quad 4\text{-}9$$

where k is the wave vector, and r is the radius of the outermost sphere.

4.2.3 Gain media and loss compensation

Many potential applications of optical metamaterials are limited by their intrinsic losses. Active media or gain materials are most commonly used, among other variants, to compensate for optical losses [85]. Thus, the use of semiconductor nanocrystals or doped dielectrics as active media can produce an optically or electrically activated population inversion. The stimulated emission of photons in coherence with the incident radiation will compensate for material losses and produce amplification. In the literature, the gain material is characterized by the material gain parameter g. This value determines the amount of gain material required for loss compensation. For example, the gain factor for loss compensation in silicon materials goes from 1 to 100 cm^{-1} [85] and directly leads to the dopant concentration required for supplying the gain using the gain cross-section data for the dopant. The total extinction coefficient $\Omega_{ext} = \Omega_{sca} + \Omega_{abs}$ will define the capability of the stimulated emission to compensate for the intrinsic optical losses. The system will be operating in an under-compensated regime for $\Omega_{ext} < 0$, a fully compensated regime for $\Omega_{ext} = 0$, or an overcompensated regime for $\Omega_{ext} > 0$ [85, 112].

When there is no lasing, a gain media can be modeled based on classical electrodynamics without considering the quantum dynamics of the ground and excited states. In that case, the system can be assumed as a dielectric with a complex refractive index having a negative imaginary part [100, 101]:

$$n_{core} = n_o + i\gamma \quad 4\text{-}10$$

The parameter γ (gain factor) represents the property of a material to amplify ($\gamma < 0$) or absorb ($\gamma > 0$) an electromagnetic field. Therefore, the material gain parameter g can be represented by $4\pi\gamma/\lambda\ [cm^{-1}]$, where λ is the free-space wavelength [85]. Undercompensated systems behave like typical dielectric materials but with stronger electromagnetic fields surrounding the structure and narrower resonances. The system acts like an optical amplifier when overcompensated at frequencies outside its resonances. A laser-like behavior is observed when losses are fully compensated at frequencies around resonance [85, 101]. Such model correctly predicts the threshold gain and the lasing generation wavelength. For describing the post-threshold operation, a nonlinear permittivity function must be considered [102].

4.3 Results and discussion

The scattering properties of an SBR with the geometry shown in Figure 4-1 were studied. The SBR considered for this study consists of an SiO_2 core ($r_{core} = \lambda/2n_{core} = 491.32\ nm$) surrounded by dielectric Bragg cladding bilayers. Each bilayer constitutes a layer of Si followed by a layer of SiO_2. The layer nearest to the core is Si and has a thickness of $L_{Si} = 101.71\ nm$, followed by a SiO_2 layer with a thickness of $L_{SiO2} = 244.98\ nm$. This geometry was optimized to act as a Bragg reflector with a stopband center at $\lambda_B \approx 1415\ nm$. As we will see later, with this design, the dipolar resonance core mode in the SBR is around the maximum absorption of the erbium cross-section [195]. The calculation was performed using experimental scattering values reported for SiO_2 and Si [196, 197].

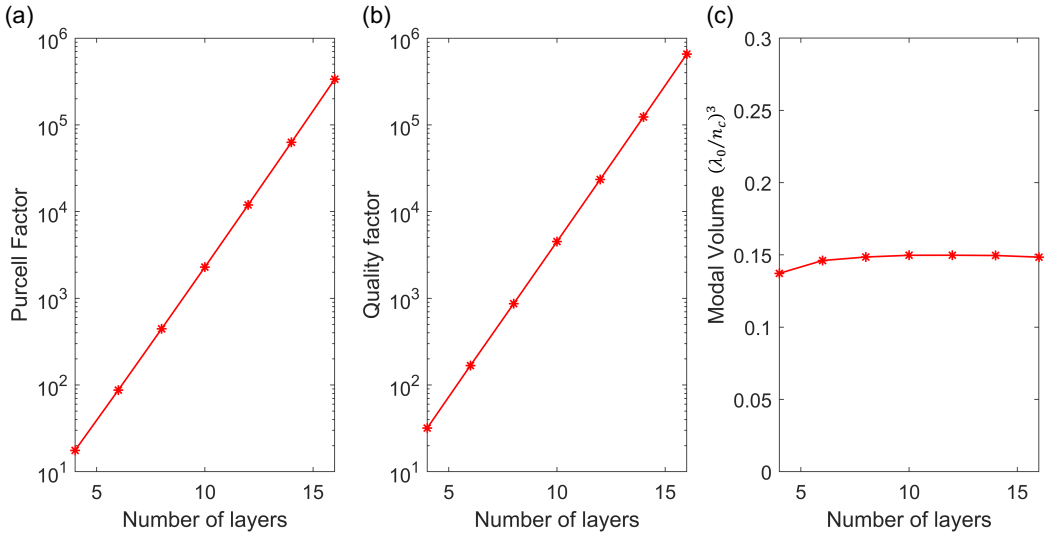

Figure 4-2 Calculated (a) Purcell factor, (b) quality factor and (c) modal volume for a spherical Bragg resonators with a different number of layers at the resonant wavelength $\lambda \approx 1536\, nm$.

The Purcell factor was calculated from Eqs. (2) and (3) at the resonant wavelength (eigenfrequency) of $\lambda \approx 1536\, nm$ for different layer numbers. The results obtained are depicted in Figure 4-2 (a). As can be appreciated, it grows exponentially with increasing layers. This indicates that the normalized spontaneous emission from a dipole placed in the SBR's core can be significantly modified by varying the number of layers.

The modal volume was computed from Eq. (4) with the obtained values of the Purcell factor, and the quality factor $Q = \omega_0/\Delta\omega$. Figure 4-2 (b) and (c) show the quality factor Q and the cavity modal volume, V for SBRs with layer numbers ranging from 4 to 16. Analogous to the Purcell factor, the quality factor shows exponential growth with an increasing number of onion resonator layers. Cavity Q values above 10^4 are obtained for a relatively small number of layers (12). These values are comparable with results obtained for well-known whispering-gallery modes [198]. The modal volume (Figure 4-2 b) remains nearly constant for the range of layers studied, with a value in the order of $(\lambda/n_c)^3$. Our analytically calculated values are in good agreement with those obtained from others numerical methods [199], as well as with those reported for other dielectric materials [36]. This reinforces our choice to use onion resonators based on Bragg reflections as omnidirectional photonic crystals with a high Q and a small modal volume in this study.

4.3.1 Scattering efficiencies and modal analysis

In the following sections, we will study and discuss the scattering properties of a 12-layer Si/SiO_2 SBR. The electromagnetic scattering of the SBR was investigated numerically with the recursive algorithm described in [30, 37]. The total scattering efficiency Ω_{sca}, total extinction efficiency Ω_{ext} and total absorption efficiency Ω_{abs} are calculated from Eqs. (7-9) and the obtained T-matrix coefficients.

The total scattering efficiencies (Ω_{sca}) computed considering the electric TE and magnetic TM multipole contributions, *l*, are exhibited in Figure 4-3 (a) and (b) show the Ω_{sca} for the electrical multipole contribution and the magnetic multipole contribution, respectively. The total scattering spectra (electrical and magnetic multipole contributions up order 5) is displayed in Figure 4-3 (c). The peaks and dips represent the different resonant and anti-resonant modes of the SBR.

These modes can be grouped into core modes and cladding modes. Core modes are of the Fabry-Perot type, and their angular quantum number *l* is relatively small (Equation 4-11). On the other hand, the cladding modes are similar to the whispering gallery modes in ring resonators and have larger angular quantum numbers *l* [33]:

$$l \leq \frac{2\pi n_{core} r_{core}}{\lambda} \qquad 4\text{-}11$$

For our SBR, the resonance frequencies in the cladding layers corresponded to $l = 3$ and 4 and those in the core to angular quantum number $l = 1$. Significant differences are found between the modes located in the core and the cladding layers. The scattering resonances of the cladding mode (TM5 and TE4) are more pronounced in amplitude than those of the core modes (TE1), as can be appreciated in Figure 4-3.

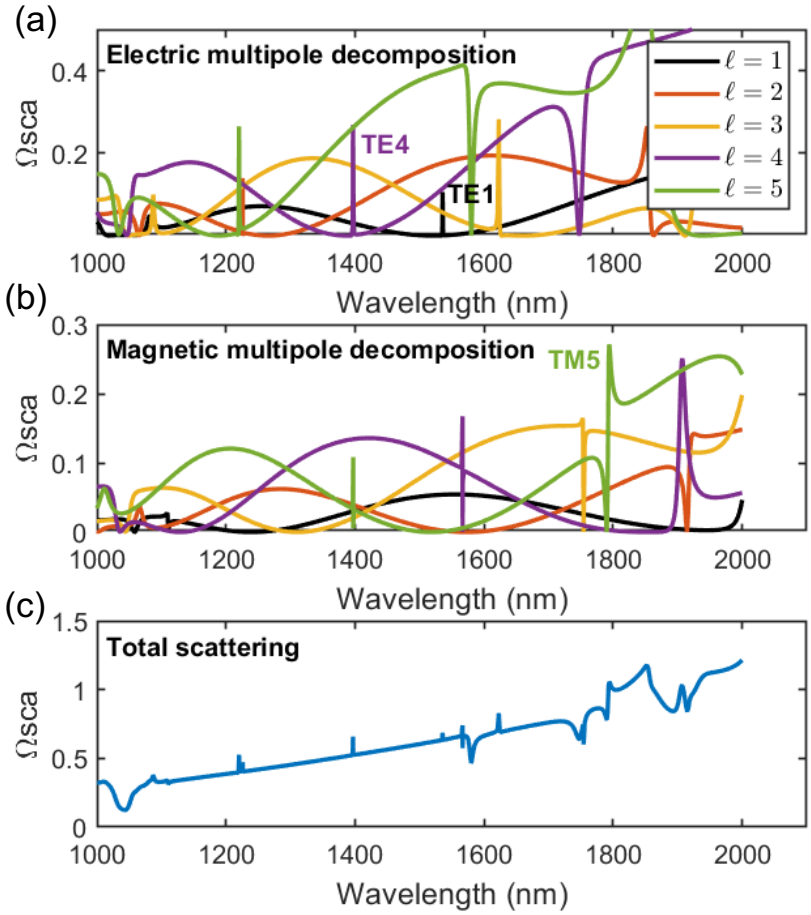

Figure 4-3 Scattering efficiencies for a 12-layer spherical Bragg resonator for five multipoles (a) electric, (b) magnetic and (c) total modes.

To investigate the difference between cladding mode and core mode resonances, we studied the spatial distribution of the normalized magnitude of total electric field $|E|^2/|E_0|^2$ and total magnetic field $|H|^2/|H_0|^2$ of a 12-layer SBR (Figure 4-4). As can be noted, the field distribution of the core mode ($l = 1$, dipolar mode) TE1-TM1 are mostly confined within the SBR's core. Whereas the electromagnetic fields of the cladding mode ($l = 5$) TE5-TM5 are distributed among the cladding layers. In general, the core mode resonances exhibit more complex spectral features.

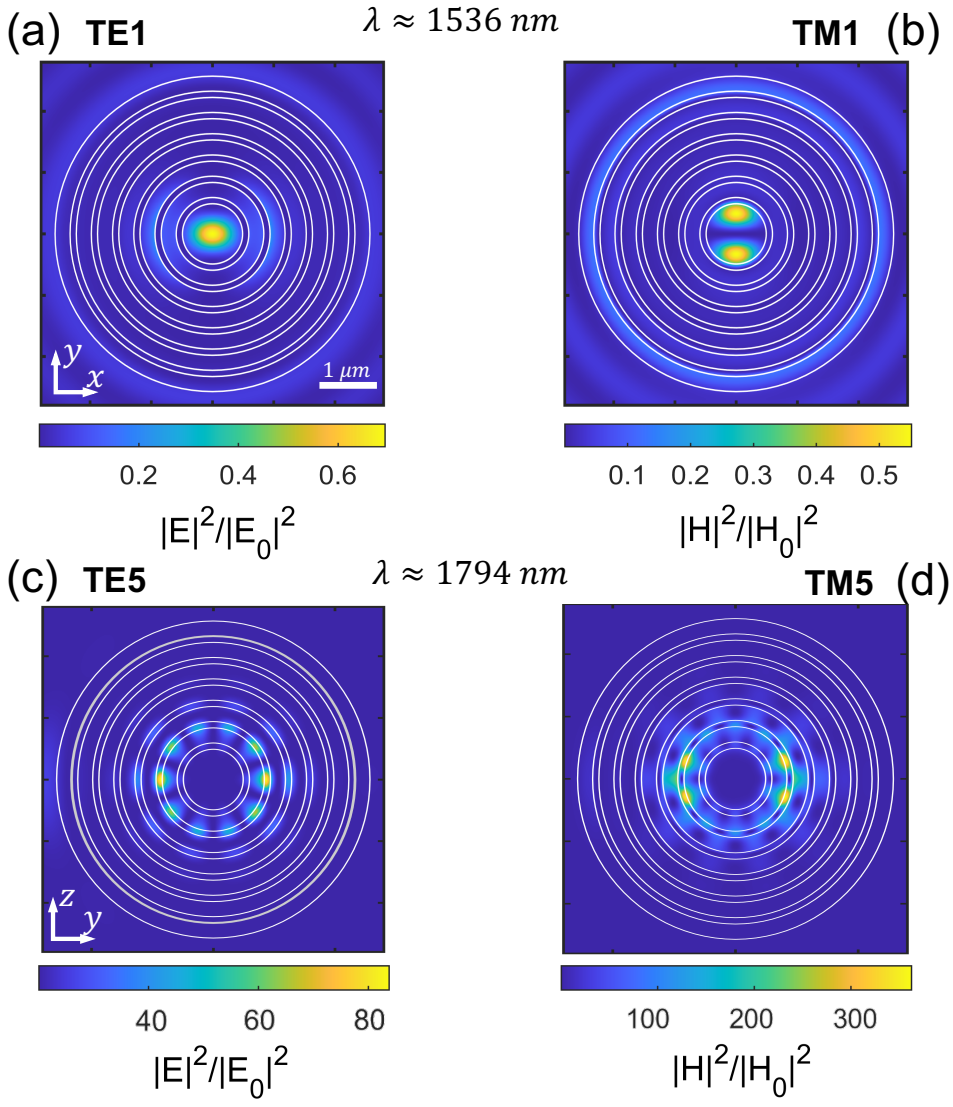

Figure 4-4 Spatial distribution of the normalized magnitude for (a) total electric field $|E|^2/|E_0|^2$ and (b) total magnetic field $|H|^2/|H_0|^2$ on the (x, y) plane for l=1 at $\lambda \approx 1536\ nm$ and (c) total electric field $|E|^2/|E_0|^2$ and (d) total magnetic field $|H|^2/|H_0|^2$ on the (y, z) plane for l=5 at $\lambda \approx 1794\ nm$ for a 12-layer spherical Bragg resonator.

4.3.2 Gain

As discussed above, structures with a small modal volume and a large quality factor are ideally suited for applications that require a large Purcell factor. We previously estimated a modal volume

of $V = 0.15(\lambda_0/n_c)^3$ and a quality factor of $Q = 10^4$ for a 12-layer SBR. This places our SBR as a potential candidate for threshold-less laser applications, as will be discussed next.

We investigated the total scattering efficiencies by adding a gain in the 12-layer SBR core. We used Er^{3+} (g~1–100 cm^{-1}) as a gain medium. In our model, a gain medium can be modeled by adding a negative imaginary part to the refractive index. Figure 4-5 shows the scattering efficiencies for a 12-layer SBR doped in the core with Er^{3+}. The scattering efficiencies (Ω_{sca}) are depicted in Figure 4-5 (a). An enhancement of the scattering efficiency occurs at the core eigenfrequency $\lambda \approx 1536\,nm$ for a gain factor of $\gamma \approx 5.20 \times 10^{-5}$. This significant increase in Ω_{sca} was coupled with a reversal Ω_{ext} and Ω_{abs} to negative values as can be seen in Figure 4-5 (c) and (d). It indicates that the active medium can compensate for radiative and dissipative losses. This is evidence of the suitability of the system to amplify the incoming radiation, creating an outgoing wave with more intensity than the incoming one.

The scattering intensity and full width half maximum (FWHM) were plotted as a function of the gain factor at the core eigenfrequency λ = 1536 nm in Figure 4-5 (b). The relation between scattering intensity and FWHM exhibits a threshold-like gain factor of around $\gamma \approx 5.00 \times 10^{-5}$, Figure 4-5 (b). Below this threshold, the scattering emission intensity was very low, and the line width was wide. Above this threshold, the scattering increased suddenly, and the emission width decreased, indicating the transition of the system from an optical amplifier regime to lasing.

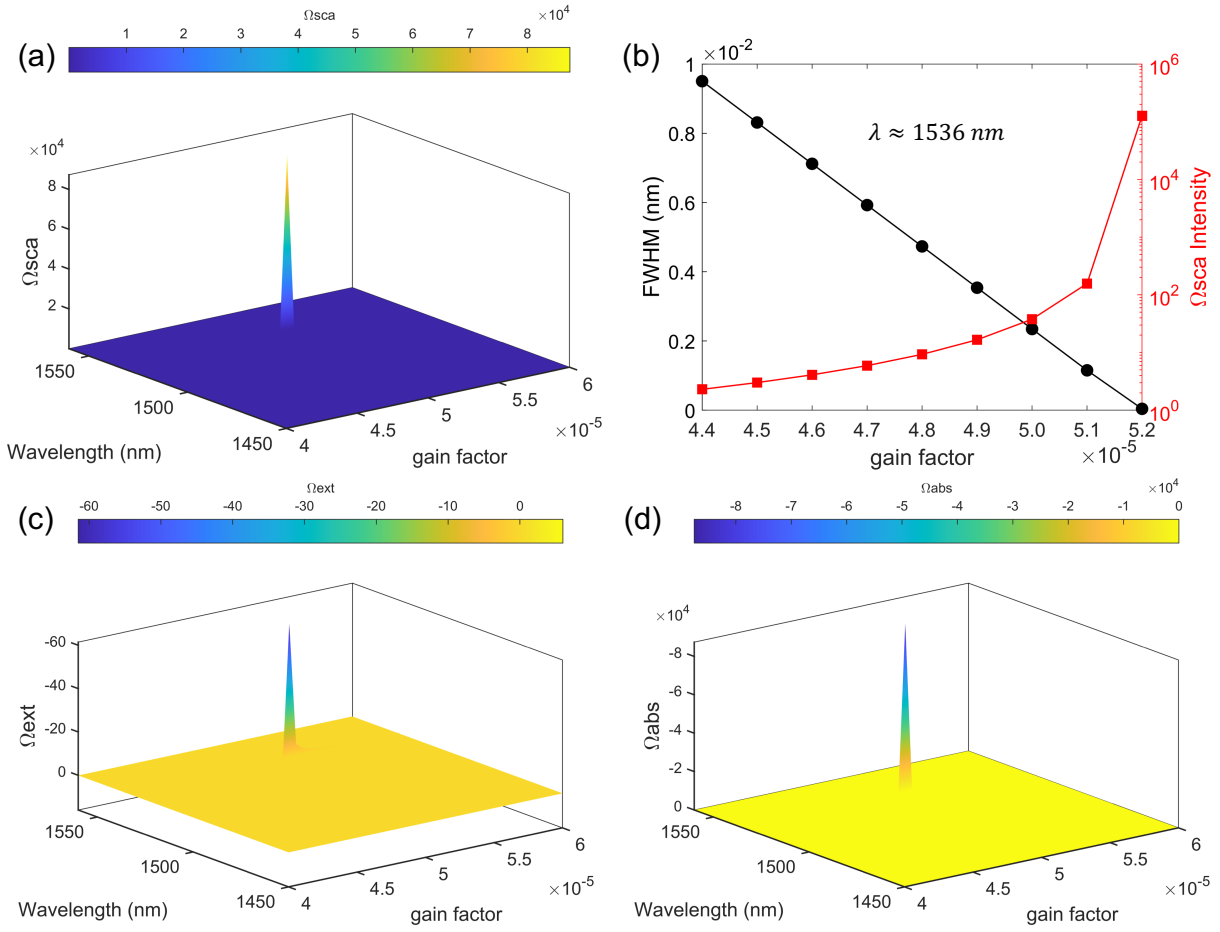

Figure 4-5 (a) Scattering, (c) extinction and (d) absorption efficiency dependency on gain factor for a 12-layer Er^{3+} core-doped Spherical Bragg Resonator. (b) FWHM (red square) and maximum scattering efficiency (black circles) dependency on gain factor.

4.3.3 Pole zero gain threshold

We previously discussed that by studying the scattering efficiencies via the transfer matrix method it is possible to find the gain threshold for which both the net radiation and material losses in an SBR are compensated. Therefore, the lasing regime is achievable. Lasing is associated with the presence of a pole of the S-matrix in the complex frequency plane. If the gain increases, it shifts from the lower complex plane to the real frequency axis [188]. As a function of the total system loss, the distance from the pole to the real axis changes, which defines the mode's Q factor and the decay rate. Consequently, the laser requires the presence of an active medium and a pole to

compensate for both material and radiative losses. This occurs for a high Purcell factor when the feedback regime is reached.

As calculated in section 3.1, TE1 mode has an eigenfrequency λ = 1536 nm. This resonance frequency coincides with the maximum of the Er^{3+} emission cross-section [195]. Figure 4-6 shows the complex S-matrix maps for the electric (c) and magnetic (d) components of the dipole mode. For reference, the scattering efficiencies are shown in Figure 4-6 for TE1 (a) and TM1 (b). In the S-matrix maps for TE1 and TM1, we can follow the singularities, which correspond to the system's eigenvalues. A point-like singularity was found around our eigenfrequency of interest (λ = 1536 nm) for the TE1 mode, as seen in Figure 4-7 (a). Therefore, the presented geometry will act as an omnidirectional resonant cavity for dopants with the same emission frequency as the singularity, such as Er^{3+}.

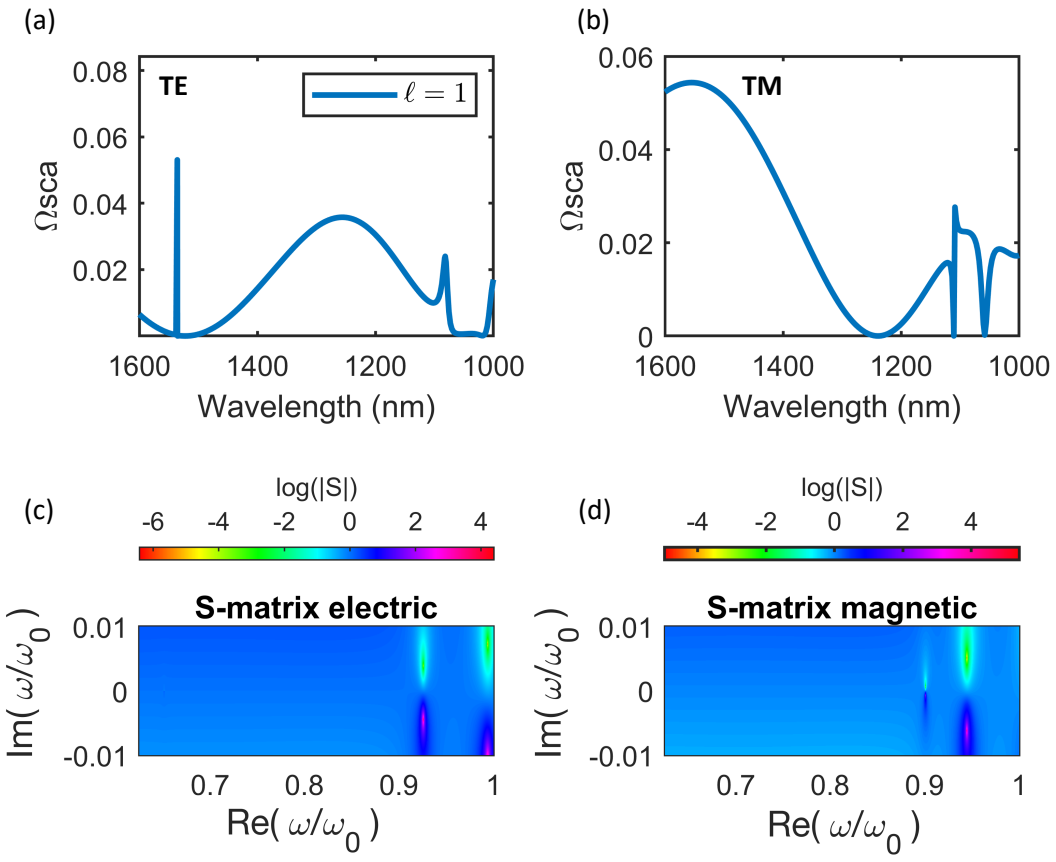

Figure 4-6 Scattering efficiencies of 12-layer Spherical Bragg Resonator for TE1 (a) and TM1 (b). Maps of the S_{pl} matrix component in the complex frequency plane for TE1 (c) and TM1 (d).

Looking closely at the TE1 singularity at $\omega/\omega_0 \approx 0.65$, we can identify zeros and poles, Figure 4-7 (a). The zeros correspond to perfect absorption, and poles represent the system eigenmodes. On the other hand, the addition of a gain media to the system will be reflected in a shift of the zeros and poles. Figure 4-7 (b) shows the imaginary parts of the pole and zeros when a scan over the gain factor is performed. Negative values of the pole's imaginary frequency are observed for small gains factor, while for gain factor values higher than $\gamma \approx 5.00 \times 10^{-5}$, a positive pole's imaginary frequency was achieved. This value is the threshold gain for the amplification regime. Below this value, the scattering emission intensity is low, but above this value, the scattering emission is sharply turned-up at the eigenfrequency $\lambda = 1536$ nm. Therefore, $\gamma \approx 5.00 \times 10^{-5}$ is the minimum gain factor (gain threshold) for lasing emission in a 12-layer Er^{3+} core doped Spherical Bragg Resonator.

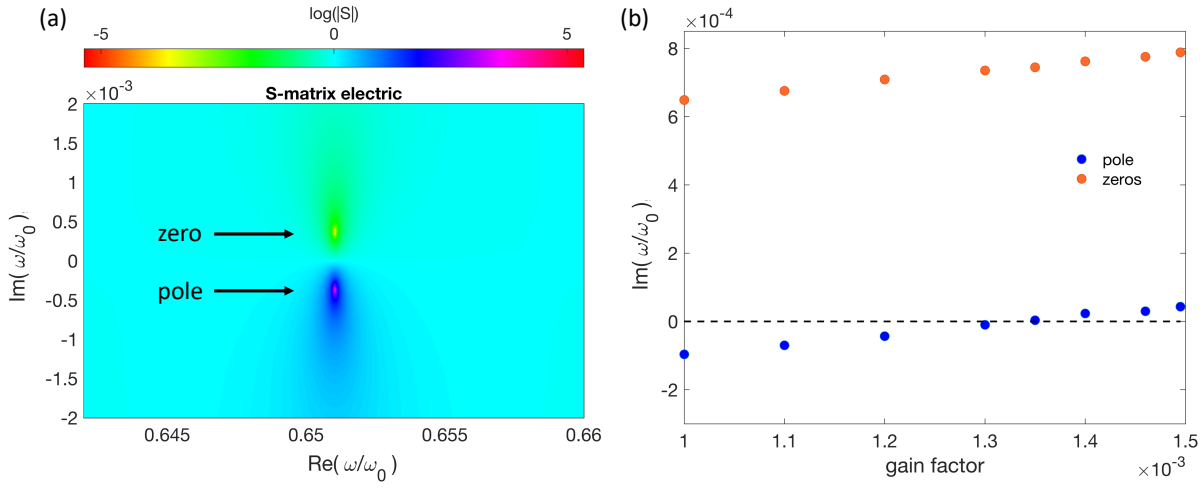

Figure 4-7 (a) Maps of the S_{pl} matrix component in the complex frequency plane for TE1 in a 12-layer Er^{3+} core-doped Spherical Bragg Resonator. (b) Pole (blue) and zeros (orange) analysis of S-matrix scattering dependency on gain factor, gamma.

The gain factor threshold for the lasing regime is highly dependent on the number of SBR layers. This is in agreement with the exponential growth of the Purcell factor observed previously. The gain threshold and Er^{3+} dopant concentration for lasing as a function of the number of layers in the SBR are shown in Figure 4-8. The gain factor depends on the density of the dopant and its cross-section emission [200]. For the case of Er^{3+}, whose emission cross-section is $\sigma = 7.27 \times 10^{-21}\ cm^2$ at $\lambda = 1536$ nm [201], $\sim 1.50 \times 10^{22}\ ions/cm^3$ are required to obtain laser

emission in a 8-layer SBR structure. This value is slightly higher than the Er^{3+} dopant concentration in commercially available Er^{3+} doped silica materials. However, adding two more Si/SiO_2 bilayer (12-layer) makes it possible to achieve a lasing regime with an Er^{3+}doped SiO_2 core concentration of $\sim 5.63 \times 10^{20}\ ions/cm^3$ since the threshold gain factor is reduced to $\gamma \approx 5.00 \times 10^{-5}$.

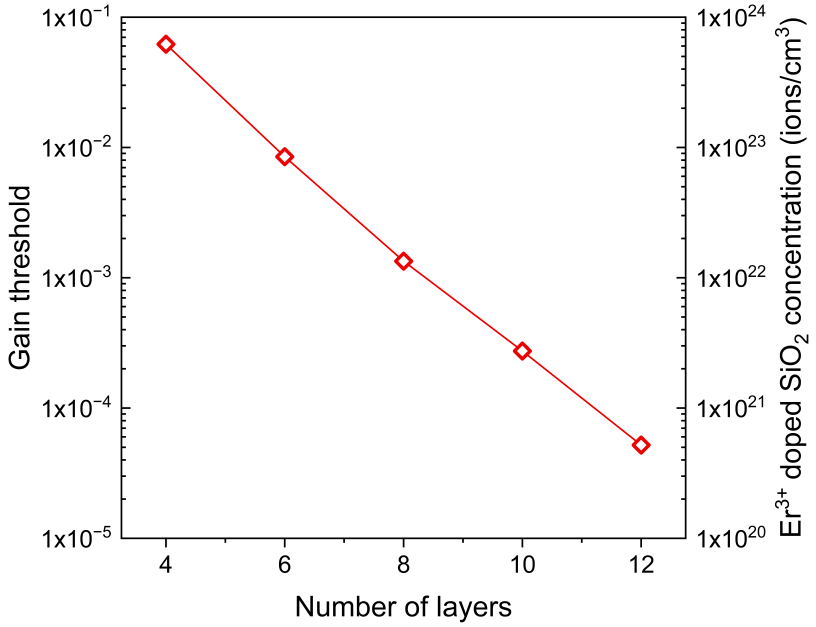

Figure 4-8 Gain threshold and Er^{3+} core-doped concentration for lasing in a Spherical Bragg Resonator as a function of the number of layers.

The dopant density of Er^{3+} in a 12-layer SBR structure is within the typical range [201]. Er^{3+}-doped silica glass-based materials are commercially available with similar dopant densities, such as single and multi-mode optical fibers. Furthermore, SBRs have been fabricated with precise control of the layer's thickness and chemical composition by plasma enhanced chemical vapor deposition (PECVD) technique [33, 41, 42]. In fact, A. V. Medvedev et al. [41] have recently demonstrated the presence of a complete photonic band gap in a non-rare earth doped SBR structure.

We propose an SBR structure with a core made by melting a commercial Er^{3+} ion-doped silica optical fiber. The optical fiber tip radii can be controlled by the etching process. With a 980 nm diode laser, Er^{3+} ions can be excited through the silica fiber with the spherical tip. Depending on the Er^{3+} concentration in the silica doped microsphere, amplification or lasing of the scattered

signal may be obtained. By placing a half-taper fiber close to the surface of the SBR, we can collect the scatter signal and analyze it with an optical spectrum analyzer.

The spontaneous emission of rare earth atoms and quantum dots (QDs) can be suppressed or enhanced by different classes of photonic structures such as woodpiles, concentric cylinders, spherical Bragg resonators, or inverse opals [47, 48]. In our case, the high-quality factor Q and small modal volume V of our SBR significantly influence the emission rate of Er^{3+} atoms in the core. To demonstrate that, we will consider an Er^{3+} emitter located in the center of our structure. As the maximal optical emission of Er^{3+} atoms match with the single mode of the cavity (resonant condition), the emission rate (Γ/Γ_0) is enhanced through the Purcell effect [45, 46]. The lifetime of the Er^{3+} which is the inverse of the emission rate and, in the cavity, contrasts with its value in free space. This modification can be estimated from the Purcell factor of the cavity (P) and is given by the following relation [202, 203]:

$$\frac{1}{\tau_{SBR_{Er^{3+}}}} = \frac{P}{\tau_r} + \frac{1}{\tau_{nr}} \qquad 4\text{-}12$$

Shorter lifetimes raise spontaneous photons, increasing stimulated emission and amplifying spontaneous emissions [85]. In the case of our 12-layer Er^{3+} core doped SBR, the Er^{3+} lifetime decreased from $\tau_r \approx 4\ ms$ in free space [204] to $\tau_{SBR_Er^{3+}} \approx 127\ ns$ seconds in the cavity core. We have considered that the decay rate is purely radiative ($\tau_{nr} \approx 0$), as previously reported theotrically and experimentally in Er^{3+}-doped silica glass with a dopant concentration of $\sim 5.00 \times 10^{20}\ ions/cm^3$ [204]. The enhancement of the emission rate of an Er^{3+} emitter ($\Gamma/\Gamma_0 \sim 10^4$) situated at the core, further confirms the suitability of our proposed SBR geometry for light sources, amplifiers, and lasers.

In contrast, for off-resonance, significant inhibition of the spontaneous emission of an Er^{3+} emitter is produced [46]. Such conditions can be achieved by increasing (or decreasing) the core radius r_{core} by a factor of $(2s+1)/2$, were s is an integer value, resulting in cavity modes different from the Er^{3+} emission wavelength. For example, considering a 12 layers-SBR with a radius of $r_{core}/2$, the lifetime of an Er^{3+} atom will be longer ($\tau_{SBR_Er^{3+}} \approx 25\ s$) than the free space value, inhibiting its spontaneous emission from the SBR core, by a factor of $\Gamma/\Gamma_0 \sim 10^{-4}$. Its effect is essential for optical quantum information processing applications [60, 205, 206]. Similar values of enhancement

and suppression of the spontaneous emission of a dipole emitter embedded in a spherical Bragg resonator have been reported previously [48].

We have found a gain threshold using two different methods: scattering efficiencies and band-with, and pole and zero in the S-matrix map. The pole-zero method provides a better understanding of the amplification regime and confirms the lasing condition. In addition, we discuss the potential of the SBR for light emission control.

4.4 Conclusions

We have investigated the scattering properties of Si/SiO_2 Spherical Bragg Resonators doped in the core with Er^{3+}. The SBR geometry proposed in this work was optimized based on experimentally obtained refractive index values and dopant concentrations. Our onion resonator has a modal volume of $V = 0.15(\lambda_0/n_c)^3$ and a quality factor of $Q = 10^4$ for 6 Si/SiO_2 bilayers highlighting its potential for spontaneous emission engineering. Using the transfer matrix T for the scattering in Er^{3+}-doped Spherical Bragg Resonators, we found an enhancement in the scattering efficiency (Ω_{sca}) for the dipolar core mode (TE1) at λ = 1536 nm and a dopant gain $\gamma \approx 5.20 \times 10^{-5}$. Negative Ω_{ext} and Ω_{abs} were observed for these values, indicating a compensation of radiative and dissipative losses. We find the threshold gain factor for lasing by scanning poles and zeros of the S-matrix in the complex frequency plane. Six Si/SiO_2 bilayers (or 12 layers) were found to be sufficient to reduce the threshold gain factor to $\gamma \approx 5.00 \times 10^{-5}$. This value corresponds to a dopant density of Er^{3+} of $5.63 \times 10^{20}\ ions/cm^3$. Materials with such concentrations are commercially available. On the other hand, the plasma-enhanced chemical vapour deposition (PECVD) technique has been used to obtain core-shell type structures. Therefore, we expect this work to pave the way for future experimental demonstrations of threshold-less lasers based on Spherical Bragg Resonators.

4.5 Funding, acknowledgments, and disclosures

4.5.1 Funding

Natural Sciences and Engineering Research Council of Canada (Discovery grants, Strategic Research grants).

4.5.2 Acknowledgments

R. Kashyap acknowledges financial support for the Canadian NSERC Discovery grants and Strategic Research grants programs.

4.5.3 Disclosures

The authors declare no conflicts of interest.

4.5.4 Data availability

Data underlying the results presented in this paper are not publicly available at this time but may be obtained from the authors upon reasonable request.

CHAPTER 5. ARTICLE 3: MAGNETIC PURCELL ENHANCEMENT IN A NANOANTENNA-SPHERICAL BRAGG RESONATOR COUPLED SYSTEM

Yalina García-Puente and Raman Kashyap

Published in: Annalen der Physik, October 2, 2023

In this work, we proposed a novel approach for enhancing magnetic fields in all-dielectric nanoantennas using Spherical Bragg Resonators (SBR), which can boost quantum emitters' magnetic transitions. A matrix method has been used to optimize the magnetic dipole resonance of a SiO_2/Si core-shell spherical nanoantenna. We studied the radiative and non-radiative decay rate of a Eu^{3+} emitter with a quantum efficiency of ~80%. Our findings revealed that the magnetic dipole nanoantenna resonance coupling with the SBR mode significantly enhances the modal magnetic field. A 4-layer SiO_2/Si SBR results in a Purcell factor of $\sim 5 \times 10^3$, the highest we have found in the literature, to the best of our knowledge. Our work offers a theoretical demonstration of the potential of SBR to improve the performance of dielectric nanoantennas.

5.1 Introduction

Nanophotonic structures composed of all-dielectric nanoresonators with high permittivity and low ohmic losses have recently attracted significant attention [113, 207-210]. One of the main reasons is that they offer a more energy-efficient solution for metamaterial [210, 211], nanoantenna [212], and metasurface [213] applications over the traditional plasmonic approach.

The multipole Mie-type resonance of high refractive index dielectric nanostructures has been extensively studied, theoretically [107-109] and experimentally [110, 111]. In particular, silicon nanoparticles with dimensions around $100\ nm$ or larger present a marked electric and magnetic dipole resonance that is not associated with significant non-radiative losses in the visible and infrared spectral range [107]. The electrical and magnetic resonance of dielectric nanoparticles induced by the incident electric field is due to the oscillations of the polarization charges and the circular displacement of the displacement current, respectively [110, 214]. These nanoresonators have been successfully employed as biosensors and in electrical and magnetic spontaneous emission engineering [105, 215-217].

In past years, different nanoantenna designs have been proposed to favor light-matter interaction. Receiving more attention have been interactions produced by coupling electric dipole transitions with the electromagnetic field since the magnetic dipole emission is usually orders of magnitude weaker in most materials [104]. However, the low losses and high magnetic resonance in the visible range in Si nanoantennas permit reaching a high local density of magnetic states, making the coupling with the magnetic dipolar mode significant [111, 212, 218]. This enhanced magnetic field allows the modification of magnetic transitions in some transition metals, such as Cr^{3+} [219], and lanthanide series ions, like Eu^{3+} [105] and Er^{3+} [106], in which electric dipolar first-order transitions are normally forbidden. Enhancing and controlling this magnetic dipolar emission is crucial, especially in nano-structured systems.

On the other hand, it has been previously demonstrated that the magnetic dipolar emission of quantum emitters can be modified with photonic cavities [21, 125]. In particular, Brûlé *et al.* propose an optimized geometry to control dipolar emitters' electric and magnetic decay rate, a Si hollow disk with a Gd_2O_3 core surrounded by air/Si circular gratings [125]. They report an increase of the magnetic Purcell factor in europium (Eu^{3+}) ions up to $\sim 2 \times 10^3$. However, this air/Si 6-ring circular grating design saturates the maximum achievable value of the magnetic Purcell factor, which is also highly dependent on the orientation of the dipolar emitter.

In this work, we propose using Spherical Bragg Resonators (SBR) to enhance magnetic fields in spherical all-dielectric nanoantennas, boosting quantum emitters magnetic transitions. These photonic resonators with omnidirectional bandgap are characterized by resonant modes with high-quality factor values and small modal volume [33, 36, 48, 180]. Recently, we demonstrated their ability to manipulate electrical quantum emitters for optical amplification and lasing [165]. A transfer matrix method [30, 37] has been used to optimize the magnetic dipole resonance of a Si/SiO_2 core-shell spherical nanoantenna. We studied a dipolar magnetic emitter's radiative and non-radiative decay rates, resulting in a quantum efficiency of ~80%. The coupling of magnetic dipole nanoantenna resonance with the SBR defect mode enhances the modal magnetic field. A 4-layer SBR results in a magnetic Purcell factor enhancement up to $\sim 5 \times 10^3$, the highest we have found in the literature [21, 125], to the best of our knowledge. Our calculations indicate a significant improvement in the performance of Si/SiO_2 core-shell spherical nanoantennas using SBRs structures.

5.2 Methods

The cross-section of the studied SiO_2/Si core-shell spherical nanoantenna is illustrated in Figure 5-1 (a). We indicate the inner radius by r_i, and R is the outer radius. The nanoantenna is placed in the vacuum and illuminated by a plane wave. The electric dipolar (ED) and magnetic dipolar (MD) Mie-type modes induced in the high refractive index dielectric nanoantenna are schematically depicted in Figure 5-1 (b). The ED mode results from the communal polarization of the nanoantenna material, which induces a magnetic current loop. Whereas the MD mode results from an electric displacement current loop that generates a magnetic dipole moment. Experimental scattering values reported for SiO_2 and Si were used for the SiO_2/Si core-shell spherical nanoantenna simulations [196, 197].

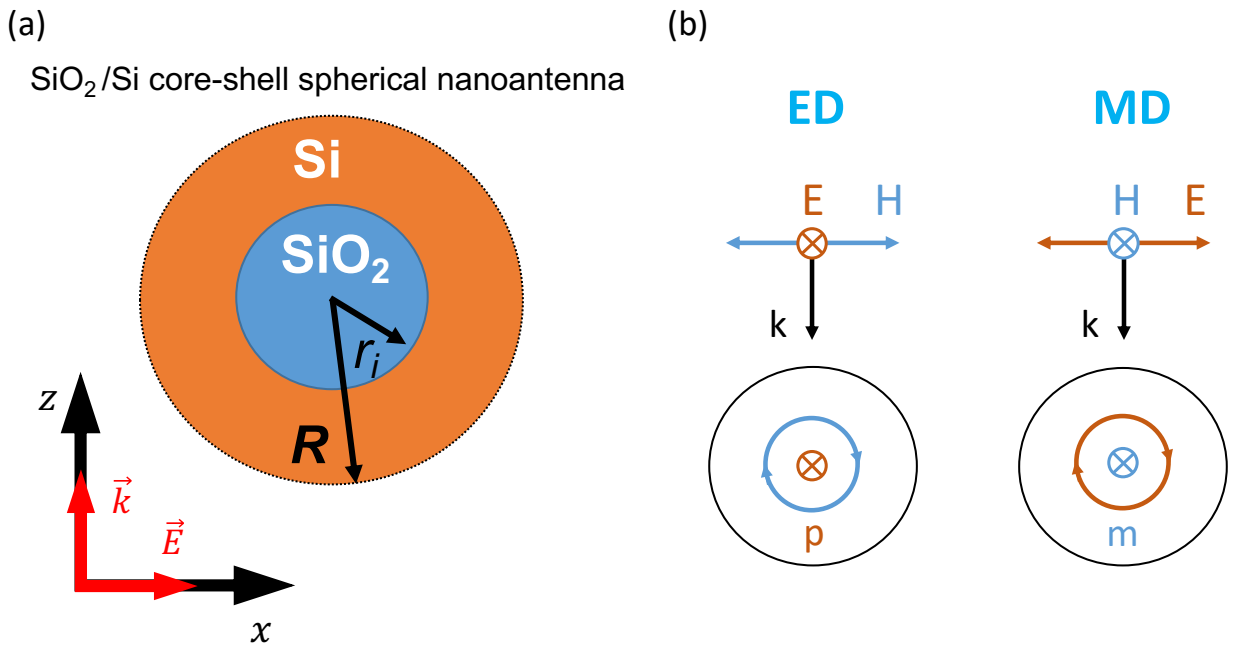

Figure 5-1 (a) Cross section of a SiO_2/Si core-shell spherical nanoantenna of total radius R and inner radius r_i excited by a plane wave. (b) Schematic representation of the electric dipolar (ED) and magnetic dipolar (MD) modes induced by the plane wave excitation. The ED mode results from the communal polarization of the nanoantenna material, which induces a magnetic current loop. The MD mode results from of an electric displacement current loop that generates a magnetic dipole moment.

We use a fast recursive transfer matrix method for a rigorous study of the nanoantenna-Spherical Bragg Resonator coupled system we propose in this work. This method can estimate the electric and magnetic field distribution, the scattering efficiencies and the radiative and non-radiative dipole decay rate in multilayer spherical structures [30]. This has made the recursive transfer matrix algorithm a powerful tool for the theoretical approach to studying different plasmonic and dielectric nanostructures [32, 220, 221]. In particular, we have already successfully applied this recursive transfer matrix method to demonstrate the feasibility of SBRs for engineering optical amplification and threshold gain for lasing [165].

5.2.1 Magnetic field

The spherical geometry of the multilayered spheres allows the electric and magnetic field in the *s-th* layer to be obtained, as a multipole vector spherical wave expansion, for each transverse electric (TE) and transverse magnetic (TM) polarization component, p [30]:

$$\vec{H}(s,\vec{r}) = -i\frac{\varepsilon_s}{\mu_s}\sum_{pL}\left[A_{pL}(s)\vec{J}_{pL}(k_s,\vec{r}) + B_{pL}(s)\vec{G}_{pL}(k_s,\vec{r})\right] \quad 5\text{-}1$$

where $L = l,m$ are the orbital and magnetic angular momentum respectively, $k_s = 2\pi n_s/\lambda$ represents the wavenumber in the *s-th* spherical shell with refractive index n_s, λ is the wavelength of the incident plane wave, $A_{pL}(s)$ and $B_{pL}(s)$ are the expansion coefficients with different linear combinations of the Riccati-Bessel functions, and $\vec{J}_{pL}(k_s,\vec{r})$ and $\vec{G}_{pL}(k_s,\vec{r})$ are the vector multipoles [30, 31]. By applying the recursive algorithm, the expansion coefficients $A_{pL}(s)$ and $B_{pL}(s)$ are obtained by equating the electromagnetic field tangential components at each layer boundary [31, 32].

5.2.2 Decay rate

The total radiated power of a dipole with and without the SBR was calculated with the transfer matrix method to estimate the normalized radiative ($\Gamma^{rad}/\Gamma_0^{rad}$) and nonradiative ($\Gamma^{nrad}/\Gamma_0^{nrad}$) decay rate [54].

$$\frac{\Gamma_\perp^{rad}}{\Gamma_0^{rad}} = \frac{3}{2x_d^4}\frac{n_d}{n_h}\sum_l l(l+1)(2l+1)|f_{Ml}(x_d)|^2 \quad 5\text{-}2$$

$$\frac{\Gamma_{\parallel}^{rad}}{\Gamma_0^{rad}} = \frac{3}{4x_d^4}\frac{n_d}{n_h}\sum_l(2l+1)[|f_{El}(x_d)|^2 + |f'_{Ml}(x_d)|^2] \quad 5\text{-}3$$

$$\frac{\Gamma_{\perp}^{nrad}}{\Gamma_0^{nrad}} = \frac{3k_d^3}{2x_d^4}\frac{1}{n_d n_h} Im(n_a^2)\sum_l l(l+1)(2l+1)\Omega_{Ml}|g_{Ml}(x_d)|^2 \quad 5\text{-}4$$

$$\frac{\Gamma_{\parallel}^{nrad}}{\Gamma_0^{nrad}} = \frac{3k_d^3}{4x_d^4}\frac{1}{n_d n_h} Im(n_a^2)\sum_l(2l+1)[\Omega_{El}|g_{El}(x_d)|^2 + \Omega_{Ml}|g'_{Ml}(x_d)|^2] \quad 5\text{-}5$$

In this context, "⊥" and "∥" denote the perpendicular and parallel orientations of the dipole at position *d*, respectively. The refractive index of the host medium is represented by n_h, and l is the angular quantum number. The functions $f_{\mathrm{El,Ml}}(\mathrm{x_d})$ and $g_{\mathrm{El,Ml}}(\mathrm{x_d})$ are linear combinations of Riccati-Bessel functions, and the prime indicates differentiation with respect to the argument.[38] The dimensionless size parameter, denoted by $\mathrm{x_d}$, is defined as the product of k_d and r_d, where k_d is equal to $2\pi n_\mathrm{d}/\lambda$. The volume integrals taken over any absorbing region with refractive index n_a are denoted by $\Omega_{\mathrm{El,Ml}}$.

If the dipole is placed outside the sphere's center, the normalized radiative decay rate is given by:

$$\frac{\Gamma}{\Gamma_0} = \frac{1}{3}\frac{\Gamma_{\perp}}{\Gamma_0} + \frac{2}{3}\frac{\Gamma_{\parallel}}{\Gamma_0} \quad 5\text{-}6$$

here $\Gamma_{\perp}/\Gamma_0$ is the radially normalized component and $\Gamma_{\parallel}/\Gamma_0$ is the tangentially normalized component of dipole radiative decay [30, 36]. In addition, the quantum efficiency (QE) can be calculated as:

$$QE = \frac{\Gamma_{rad}}{\Gamma_{rad} + \Gamma_{nrad}} \quad 5\text{-}7$$

by taking into account the material loss for the calculation of the non-radiative normalized decay rate (Γ_{nrad}) of the dipole emitter.

5.3 Results and Discussion

The analytical solutions of the resonances supported by silicon (Si) nanospheres were analyzed for an increasing radius from $60\,nm$ to $130\,nm$. A fast transfer matrix method [30] was used to calculate the scattering cross-section spectra, normalized to the geometrical cross-section (scattering efficiency, *Qsca*). The total *Qsca* as a function of the radius of a Si nanosphere and the

wavelength of the incident plane wave is depicted in Figure 5-2 (a). It shows the electric and magnetic modes supported by these high refractive index nanospheres. As the Si nanosphere dimensions increase, there is a red shift of the ED and MD modes and the appearance of higher order modes supported by the nanoresonator. This is due to a larger portion of the displacement current loop remaining inside the Si nanosphere with an increased radius. In addition, as the volume and polarizability increase, the scattering efficiency and the intensity of the peaks of the resonant modes rise. As an illustrative example, Figure 5-2 (b) shows the scattering efficiency of a Si nanosphere with a diameter of $D = 208\ nm$, indicated by dashed line in Figure 5-2 (a). Multipole decomposition of the total scattering allowed the identification of electric dipole (ED), magnetic dipole (MD), and magnetic quadrupole (MQ) resonances at $\lambda \approx 630\ nm$, $\lambda \approx 800\ nm$ and $\lambda \approx 590\ nm$, respectively.

Figure 5-2 (c) represents an illustration of the evolution of a Si sphere of diameter $D = 144\ nm$ in a SiO_2/Si core-shell spherical nanoantenna of inner radius r_i variable from $0\ nm$ to $90\ nm$. The calculated total *Qsca* as a function of wavelength and inner radius is shown in Figure 5-2 (d). As can be noticed, as r_i increases, the amplitude of the resonant peaks decreases and gradually blueshift as the effective refractive index of the SiO_2/Si core-shell spherical nanoantenna experiencing the electromagnetic field is lower. Therefore, the choice of the core material is critical to the performance of the core-shell nanoantenna to enhance magnetic emitters transitions, as we will see later on.

The nature of the magnetic and electrical resonances is different, which explains the shift in the relative position of the ED and MD modes when r_i is modified. The shift in the spectral position of the ED mode seems to saturate around $\lambda \approx 400\ nm$ when the inner radius is approximately $r_i \approx 40\ nm$. In contrast, the MD mode keeps shifting toward shorter wavelengths as r_i increases.

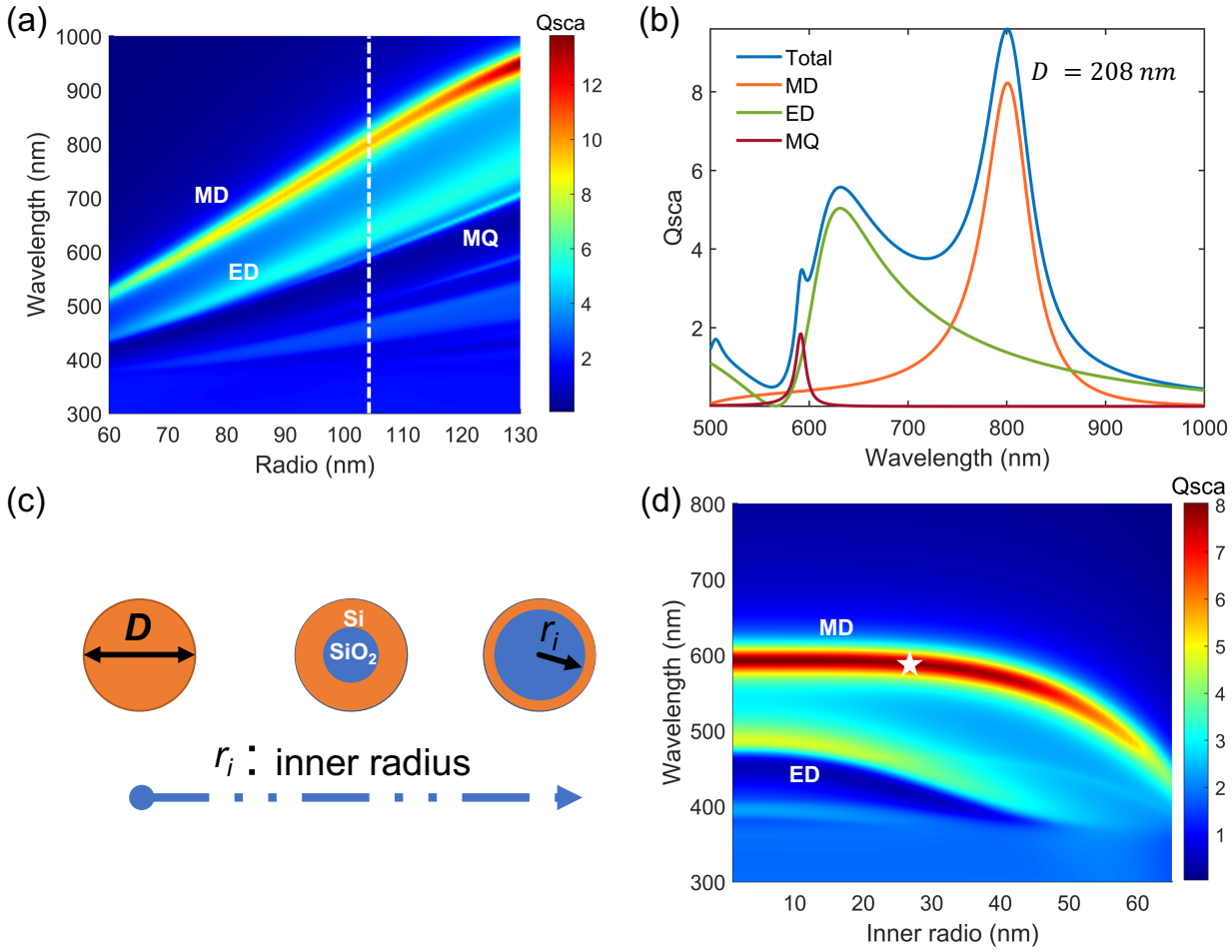

Figure 5-2 (a) Total scattering efficiency as a function of the radius of a Si nanosphere and the wavelength of the incident plane wave. (b) Contribution to the total scattering of a $208\ nm$ Si sphere from the electric dipole (ED), magnetic dipole (MD), and magnetic quadrupole (MQ) resonances, indicated as white vertical dashed line in (a). (c) Illustration of the evolution of a Si sphere of diameter $D = 144\ nm$ into a SiO_2/Si core-shell spherical nanoantenna of inner radius r_i varying from $0\ nm$ to $90\ nm$. (d) Calculated total scattering efficiency of the SiO_2/Si core-shell spherical nanoantenna of diameter $D = 144\ nm$ as a function of wavelength and inner radius, the star indicates an MD resonance at $\lambda \approx 590\ nm$.

Figure 5-3 (a) shows the scattering (*Qsca*) and absorption (*Qabs*) efficiencies of a SiO_2/Si core-shell spherical nanoantenna of radius $R = 72\ nm$ and inner radius $r_i = 27\ nm$ (symbolized by a star in Figure 5-2 (d)). The absorption efficiency is low (Figure 5-3 (a), black curve) due to the imaginary evanescent part of the silicon's refractive index, which indicates a small amount of

dissipative loss in interactions with a dipolar emitter. Two peaks corresponding to the electrical and magnetic resonances are clearly identified. Additionally, the inset figures illustrate the spatial distribution of the normalized magnitude for the total electric field $|E|^2/|E_0|^2$ at the ED resonance $\lambda \approx 455\,nm$ and the total magnetic field $|H|^2/|H_0|^2$ at the MD resonance $\lambda \approx 590\,nm$ in the (x, y) plane. The high magnetic field enhancement is concentrated inside the nanoantenna, while the electric field enhancement is minor and localized on the outer surface.

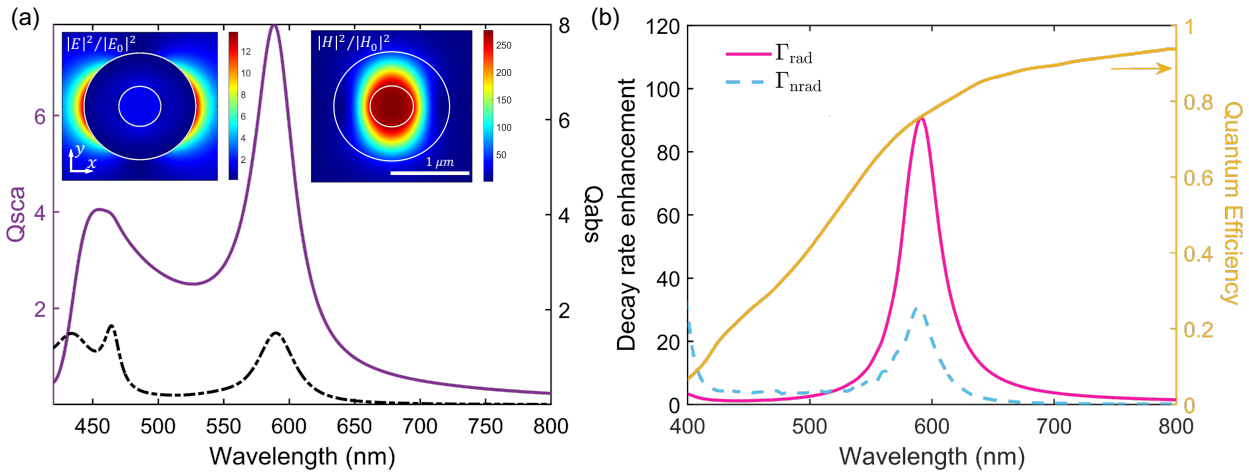

Figure 5-3 (a) Scattering efficiencies (*Qsca*) and absorption efficiencies (*Qabs*) of a SiO_2/Si core-shell nanosphere-antenna of radius $R = 72\,nm$ and inner radius $r_i = 27\,nm$. The inset figures illustrate the spatial distribution of the normalized magnitude for total electric field $|E|^2/|E_0|^2$ at the ED resonance $\lambda \approx 455\,nm$ and total magnetic field $|H|^2/|H_0|^2$ at the MD resonance $\lambda \approx 590\,nm$ on the (x, y) plane. (b) Radiative decay rate (pink line) and non-radiative decay rate (dashed cyan line) for an emitting MD located at the center of the SiO_2/Si core-shell nanosphere-antenna. Quantum efficiency for a magnetic dipolar emitter with 100% intrinsic quantum efficiency (yellow line).

We now study the interaction between a magnetic dipolar emitter and the high magnetic field obtained at the MD resonance of a SiO_2/Si core-shell spherical nanoantenna of radius $R = 72\,nm$ and inner radius $r_i = 27\,nm$. Figure 5-3 (b) presents the radiative decay rate (pink line) and the non-radiative decay rate (cyan dashed line) for a MD emitter located at the center of the nanosphere antenna. The maximum value of the radiative decay of the magnetic dipole in the studied length range is ~90, and it is about four times larger than the non-radiative decay produced by minor Si

losses. The radiative decay rate enhancement is favored by the overlap between the magnetic dipole moment of the emitter and the MD resonance of the nanoantenna [109] at λ≈590 nm. In addition, the quantum efficiency for a magnetic dipole emitter with an intrinsic quantum efficiency of 100% was calculated (Figure 5-3 b, yellow line). As can be seen, the quantum efficiency is approximately 0.8 at the maximum frequency of the radiative decay rate. As the Si losses decrease, it reaches values above 0.9 for wavelengths longer than $\lambda \approx 700\ nm$.

5.3.1 Electromagnetic field enhancement and coupling

Spherical Bragg resonators are omnidirectional photonic crystals characterized by high-quality factor resonant modes [28, 222]. These structures can be designed to act as photonic cavities with defect modes that can enhance the spontaneous emission rate of rare earth atoms and quantum dots [33, 165]. In this section, we will study the coupling of the dipolar magnetic resonance of the SiO_2/Si core-shell spherical nanoantenna, of radius $R = 72\ nm$ and inner radius $r_i = 27\ nm$, with the SBR defect mode to enhance the modal magnetic field. Figure 5-4 (a) shows a schematic of the coupled nanoantenna-SBR system proposed in this work. It consists of a SiO_2/Si core-shell spherical nanoantenna covered by concentric alternating dielectric layers with high ($n_H = 3.5$) and low ($n_L = 1.45$) refractive index. The coatings thickness (t) was chosen to satisfy the Bragg condition $t = \lambda_B/4n$ [28, 36], where n in the refractive index of the material and λ_B agrees with the dipole magnetic resonance of the nanoantenna, $\lambda \approx 590\ nm$.

First, we calculated the scattering efficiencies (*Qsca*) of the coupled nanoantenna-spherical Bragg resonator system using the coefficients of the T-matrix as described in detail by [30, 37]. Figure 5-4 (b) shows the total *Qsca* up to order four of the multipole electric and magnetic contributions for 2, 4, and 6 layers. The TM1 peak represents the resonant magnetic dipole mode and is of the Fabry-Perot type. Whereas the higher-order modes (TM2, TM3, and TM4) are similar to whispering gallery modes in ring resonators [33]. An amplitude difference between the fundamental and higher-order modes is clearly observed, as is typical in the *Qsca* spectra of SBRs [48, 165].

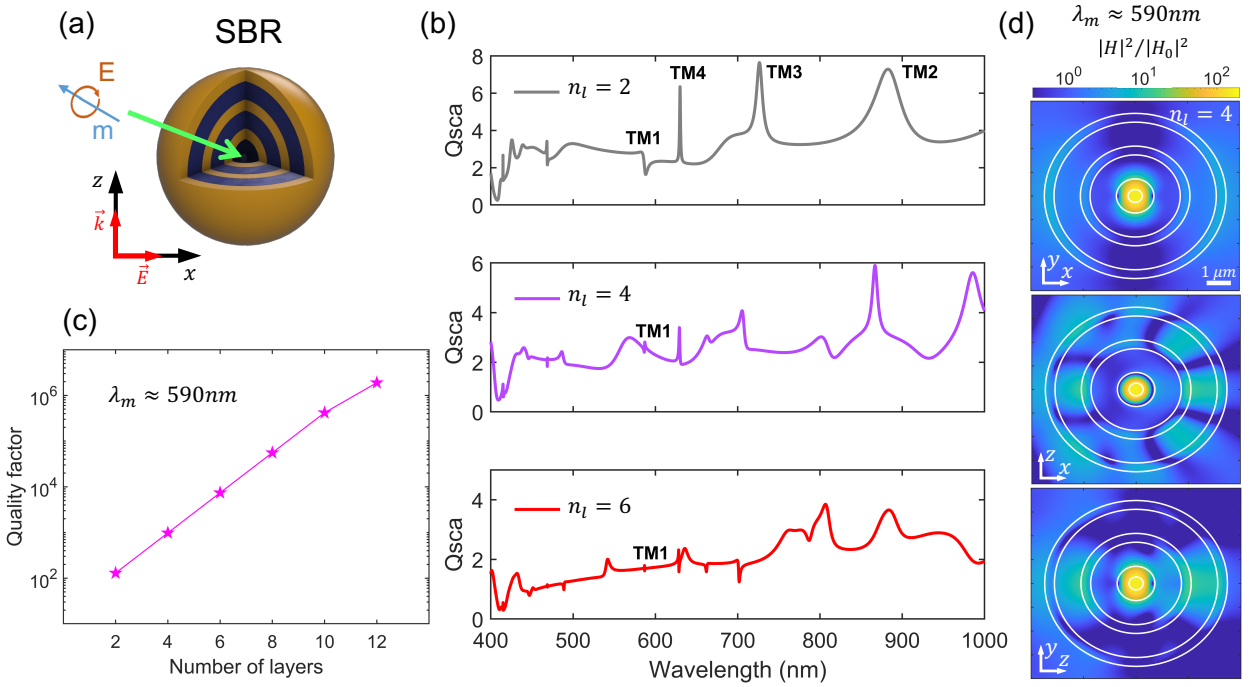

Figure 5-4 (a) Schematic of a SiO_2/Si nanoantenna-SBR coupled system. (b) Scattering efficiencies of a 2-, 4- and 6-layer spherical Bragg resonator for five electric and magnetic multipole modes. TM1 represents the magnetic resonant dipole mode, and the higher-order modes are labeled TM2, TM3, and TM4. (c) Calculated quality factor for a spherical Bragg resonator with different number of layers, n_l, at magnetic dipole resonance wavelength $\lambda \approx 590\ nm$. (d) Normalized magnitude of the total magnetic field $|H|^2/|H_0|^2$ of a 4-layer SiO_2/Si nanoantenna-SBR coupled system in the (x, y), (x, z) and (z, y) planes at $\lambda \approx 590\ nm$. The white circles represent the SiO_2/Si layers boundary.

As a second step, we calculate the quality factor $Q = \omega_0/\Delta\omega$ of the magnetic resonant dipole mode $\lambda \approx 590\ nm$ for a spherical Bragg resonator with different layers [33, 54]. From now on, we will focus our study on this mode since it coincides with the wavelength of the magnetic dipolar transition of Eu^{3+} ions ($^5D_0 \rightarrow {}^7F_1$) [105]. Figure 5-4 (c) shows an exponential trend of the quality factor with increasing layers. The calculated values show that it is possible to obtain magnetic resonant dipole modes with quality factors of $Q{\sim}10^5$ or even higher when coupling dielectric nanoantennas with an SBR. Such values are comparable to the high-quality factor of electric resonant dipole modes in SBR and for well-known whispering gallery modes.

As an illustration, in Figure 5-4 (d) is shown, the spatial distribution of the total magnetic field $|H|^2/|H_0|^2$ of the nanoantenna and a 4-layer spherical Bragg resonator coupled system at $\lambda \approx 590\ nm$. It can be noted that the most significant enhancement of the magnetic field, or hot spot, is located in the center of the structure. The presence of this hot spot is due to the displacement current produced in the nanoantenna by the incident plane wave, see Figure 5-4 (a). At the same time, the Bragg effect and the high-quality factor of the nanophotonic omnidirectional cavity allow for a considerable increase of the magnetic field in all directions.

5.3.2 Decay rate enhancement and spatial dependence

The magnetic field created at the center of the SBR is associated with the magnetic dipole moment created in the *y*-axis direction due to the currents induced by the electromagnetic wave incident in the *x*-direction. As proposed above, this can be used to promote the dipole emission of Eu^{3+}. In this section we will analyze how to enhance this interaction efficiently through the magnetic Purcell factor (MPF). This effect refers to the enhancement of the spontaneous emission rate (Γ/Γ_0) of a magnetic dipole emitter in the presence of a resonant electromagnetic environment or cavity (Γ) relative to the spontaneous emission rate in free space (Γ_0) [44, 60].

Figure 5-5 (a) shows the Purcell enhancement of a magnetic dipole emitter in the core center of the nanoantenna and a spherical Bragg resonator with a different number of layers coupled system at $\lambda \approx 590\ nm$ for two different core refractive index $n_{core} = 1.45$ and $n_{core} = 1.95$. For both cases, the exponential growth of the magnetic PF is observed as the number of the SBR layers increases since the magnetic dipole mode quality factor presented the same trend (Figure 5-4 (c)). The highest MPF values were obtained for $n_{core} = 1.45$ because the contrast with the refractive index of the silicon layer is higher. For this case, the decay rate enhancement as a function of the number of layers of the SBR resonator in a broader range of wavelengths of the MD emitter is shown in Figure 5-5 (b). At the magnetic dipole resonance wavelength, a maximum of the MPF is observed, which increases with the number of layers as the bandwidth decreases. This behavior saturates for layers larger than 10. The peaks observed at wavelengths greater than $\lambda \approx 800\ nm$ and around $\lambda \approx 400\ nm$ correspond to the upper-order magnetic resonance modes and are of the whispering gallery mode type.

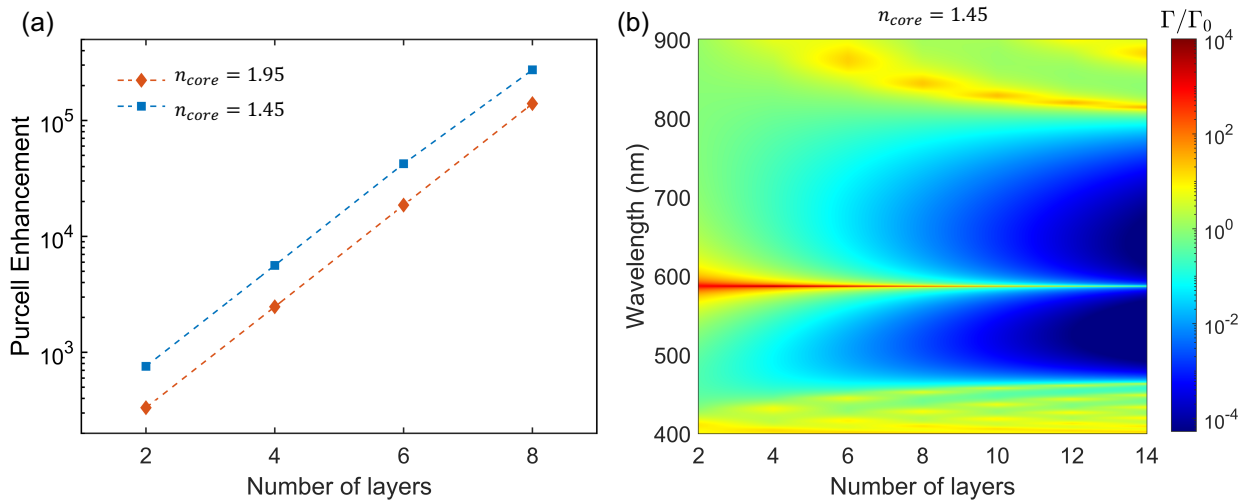

Figure 5-5 (a) Purcell enhancement of a magnetic dipole emitter in the center of a SiO_2/Si nanoantenna-SBR with a different number of layers coupled system at $\lambda \approx 590\, nm$ with core refractive index $n_{core} = 1.95$ and $n_{core} = 1.45$. (b) Decay rate enhancement as a function of the number of layers of a SiO_2/Si spherical Bragg resonator and the wavelength of the MD emitter.

In particular, the increase of the magnetic Purcell factor of a Eu^{3+} dipolar emitter at the center of a 4-layer SBR nanoantenna coupled system as a function of wavelength is shown in Figure 5-6 (a). The maximum value of the obtained decay rate is ~5600 and is at the frequency of the defect mode of the spherical resonator. As discussed in Section 5.3, the most significant enhancement of Eu^{3+} emission at $\lambda \approx 590\, nm$ is achieved by placing it in the magnetic hot spots. Therefore, it is interesting to study how sensitive is the high decay rate obtained with respect to the position of the magnetic dipole emitter inside the core of the SBR.

Figure 5-6 (b) shows the perpendicular component ($\Gamma_\perp/\Gamma_0$), parallel component ($\Gamma_\parallel/\Gamma_0$), and total decay rate (Γ/Γ_0) with respect to the x-position of the MD emitter along the x-axis. The perpendicular and parallel components of the dipole decay rate are equal when the dipole is positioned at the center of the antenna due to the symmetry of the cavity. In contrast, for off-center positions, the decay rate is given by Equation 5-6. As can be seen, the total decay rate maintains high values at any point inside the core, as expected since the magnetic field is homogeneously distributed throughout this area (Figure 5-4 (d)).

Another essential aspect to consider is how the emitter polarization has little influence on the total decay rate. This is reflected in the high values obtained for the perpendicular and parallel

components of the decay rate. The possibility to obtain high values for the decay rate of a dipolar magnetic emitter despite its polarization is due to the omnidirectionality of the SBR and can be very useful for the fabrication process. This result reveals an essential property of our nanoantenna-SBR coupled system, unlike the dielectric nanospheres [110, 223], dimers [124, 224], and concentric ring resonators [21, 125], that have been recently proposed with values of the order of those reported by us only for specific positions and dipole moment of the magnetic emitter.

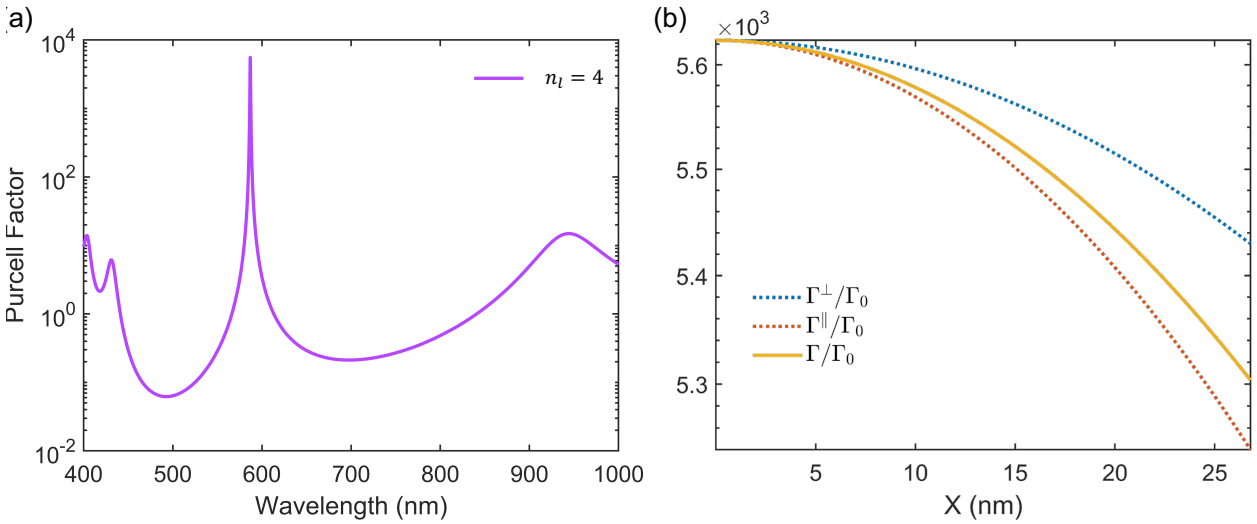

Figure 5-6 (a) Radiative decay rate enhancement of a 4-layer SiO_2/Si spherical Bragg resonator as a function of wavelength. (b) Perpendicular component, parallel component, and total decay rate at $\lambda \approx 590\ nm$ with respect to the x position of the MD emitter along the x-axis. The center of the SBR is set at $x = 0$.

Our work demonstrates that SBRs are a promising structure for enhancing magnetic fields in fully dielectric spherical nanoantennas by boosting the magnetic transitions of quantum emitters. Enhancing this magnetic light-matter interaction offers a promising alternative for developing nanoscale light sources for all-photonic chips. Furthermore, it contributes to the ongoing efforts within the scientific community to enhance light-matter interactions by controlling the magnetic local density of states [225].

Our coupled nanoantenna-SBR structure has the potential to act as a magnetophotonic crystal when dielectric magneto-optical active materials, such as garnets [226-228], are placed into the core. The dielectric tensor of these materials contains non-diagonal (magneto-optical) elements that induce

polarization conversion through non-diagonal polarizability for the nanoantennas-SBR structure. The Faraday rotation effect is the most prominent effect in this process, which makes it essential in various applications such as isolators, modulators, routers, baffles, sensors, and magnetometers [229-231].

Resonant systems have shown that the amount of electromagnetic field probing the magneto-optical material is linked to polarization conversion. Previous work on core-shell spherical structures has demonstrated up to a five-fold enhancement in magneto-optical polarization conversion at the magnetic dipolar (MD) and magnetic quadrupolar (MQ) resonance positions [226]. Therefore, the electromagnetic field enhancement induced in a dielectric nanoantenna coupled to SBRs at the MD resonance can significantly improve the magneto-optical polarization conversion.

Although our research addresses this phenomenon theoretically, Eu^{3+} doped SiO_2 nanospheres in the range of $90\ nm$ to $120\ nm$ have been successfully obtained [232]. SiO_2/Si core-shell structures have also been fabricated by plasma enhanced chemical vapor deposition (PECVD) [218]. Therefore, this work paves the way for the future fabrication of high Purcell Factor structures based on SiO_2/Si core-shell spherical nanoantenna coupled to a spherical Bragg resonator.

5.4 Conclusions

Our study focused on enhancing the emission of a Eu^{3+} emitter using a SiO_2/Si core-shell spherical nanoantenna coupled with a Spherical Bragg Resonator. We optimized the SBR to favor the magnetic dipole resonance of the SiO_2/Si nanoantenna at a wavelength of approximately $\lambda \approx 590\ nm$. Our coupled SBR-nanoantenna system, consisting of only four layers, had a high-quality factor. Moreover, we achieved a remarkable magnetic field enhancement of $|H|^2/|H_0|^2 \sim 10^3$, which was concentrated in the core of the nanoantenna. We also attained a record radiative decay rate enhancement of up to $\sim 5 \times 10^3$ times for an MD emitter in the nanoantenna-SBR coupled system. Notably, the radiative decay rate enhancement was insensitive to the core position of the MD emitter, indicating practical applicability for experimental purposes. Our findings offer new possibilities for enhancing the radiation of MD emitters and present a new avenue for innovative manipulations of magnetic light. Overall, our results demonstrate the potential of the coupled SBR-

nanoantenna system as a promising platform for efficient light emission and manipulation at the nanoscale.

5.5 Funding, acknowledgments, and disclosures

5.5.1 Funding

Natural Sciences and Engineering Research Council of Canada (Discovery grants, Strategic Research grants).

5.5.2 Acknowledgments

R. Kashyap acknowledges financial support for the Canadian NSERC Discovery grants and Strategic Research grants programs.

5.5.3 Disclosures

The authors declare no conflicts of interest.

5.5.4 Data availability

Data underlying the results presented in this paper are not publicly available at this time but may be obtained from the authors upon reasonable request.

CHAPTER 6. ARTICLE 4: HIGH-Q TAMM PLASMON-LIKE RESONANCE IN SPHERICAL BRAGG MICROCAVITY RESONATORS

Yalina García-Puente, Baptiste Auguié, and Raman Kashyap

Published in: Optics Express, March 11, 2024

This work proposes a novel Tamm plasmon-like resonance supporting structure consisting of an Au/SiO_2 core-shell metal nanosphere structure surrounded by a TiO_2/SiO_2 Spherical Bragg Resonator (SBR). The cavity formed between the core metal particle and the SBR supports a localized mode similar to Tamm plasmons in planar dielectric multilayers. Theoretical simulations reveal a sharp absorption peak in the SBR bandgap region, associated with this mode, together with strong local field enhancement. We studied the modification of a dipolar electric emitter's radiative and non-radiative decay rates in this resonant structure, resulting in a quantum efficiency of $\sim 90\%$ for a dipole at a distance of $r = 60\ nm$ from the Au nanosphere surface. A 30-layer metal-SBR Tamm plasmon-like resonant supporting structure results in a Q up to $\sim 10^3$. The Tamm plasmon-like mode is affected by the Bragg wavelength and the number of layers of the SBR, and the thickness of the spacer cavity layer. These results will open a new avenue for generating high-Q Tamm plasmon-like modes for switches, optical logic computing devices, and nonlinear applications.

6.1 Introduction

Over the past few decades, there has been extensive research into the interaction of resonant light and metal nanostructures, resulting in remarkable advancements in manipulating optical intensity at scales well below the wavelength of light [126, 127]. Surface plasmon resonances (SPRs) facilitate this interaction by harnessing the coherent oscillations of conduction electrons, resulting in an accumulation of induced charges at the metal surface, along with significant enhancements in the local field [126, 128]. Various design approaches, such as micro-disks, spherical resonators, metallic gratings, Au nanopillars, and nanoparticle arrays, have been proposed to achieve high-Q resonances and minimize radiative and Ohmic losses [142, 233-236]. Plasmon resonances have been shown to enhance light-matter interactions in various applications of interest, ranging from

photochemistry to high-harmonic generation, plasmonic nano-ovens and photodetection, as well as improve sensing and light management applications [138, 237-241].

Tamm plasmon polaritons (TPPs) are a type of hybrid plasmonic–dielectric resonance that have recently gained significant attention due to their exclusive properties and potential for practical applications [137]. Tamm plasmon polaritons are generally defined as an electromagnetic mode confined between a dielectric mirror or Bragg reflector and a terminating metallic boundary. This asymmetric structure may be seen as a cavity surrounded by two mirrors, or equivalently, with the resulting mode having a mixed photonics–dielectric character; the enhanced electromagnetic field decays very rapidly inside the metal layer, while the field penetration into the DBR affords the resonance a much higher quality factor than with surface plasmon resonance platforms [135, 136]. This field confinement leads to substantial field enhancement and sensitive environmental response. Unlike conventional surface plasmon resonances, TPPs can be directly excited at normal incidence, making them a promising alternative to standard SPs. Tamm plasmons have many potential applications, including absorbers, lasers, switches, sensors, solar photovoltaic cells, photo-catalysis, filters, and others [137-141].

Photonic crystals (PCs) have shown great potential for developing high-Q electromagnetic resonances, paving the way for their implementation in photonic and optoelectronic devices [142]. In Tamm plasmon research, a frequently used class of plasmonic nanostructure is a distributed Bragg reflector (DBR) coated with a thin metal layer. DBRs consist of layers with alternating high and low refractive indices with an optical thickness of about one-quarter wavelength [143-145]. However, recent experimental studies by *Yang et al*. have demonstrated that employing a thicker metal layer under the DBR can yield a higher Q-factor ~ 20 [151, 242]. Furthermore, introducing a defect layer into the DBR structure has enabled the observation of TPPs modes with $FWHM \sim 2\ nm$ and $Q \sim 778$ at the near-infrared region [152]. The original TPP structure was one-dimensional (1D), with a planar multilayer. These structures are relatively easy to fabricate, but limit the electric field confinement to 1D (the axis of the multilayer stack). In order to maximize light-matter interaction, a three-dimensional (3D) confinement is ideally required, which may be achieved by patterning the metal layer to further confine the TPP mode [142, 243].

Alternatively, we propose here a novel Tamm plasmon-supporting configuration that is intrinsically 3D and spherically symmetric. We investigate the near-infrared scattering properties of a SBR Tamm-like structure, obtained by surrounding an Au/SiO_2 core-shell metal nanosphere structure with a TiO_2/SiO_2 SBR. The SBR exhibits resonant modes with high-quality factor and small modal volume [28, 33, 180] and has been shown to successfully manipulate electrical and magnetic quantum emitters for optical amplification and lasing [165, 244]. By including a metal nanoparticle at the center of the structure, a new electromagnetic mode can be confined at the metal–SBR interface. Our theoretical model predicts a sharp absorption peak in the SBR bandgap window, which can be attributed to the coupling of light with a TPP-like mode confined between the core metal nanosphere and the surrounding SBR. Additionally, we examine a dipolar magnetic emitter's radiative and non-radiative decay rates and find a quantum efficiency of approximately $\sim 90\%$ for a dipole at a distance of $r = 60\ nm$ from the Au nanosphere surface. We predict that a 30-layer SBR with an Au/SiO_2 core-shell metal nanosphere structure yields TPP modes with a high-quality factor of up to $\sim 10^3$. Furthermore, we observe that the TPP induced in the structure depends mainly on the number of layers (N), the Bragg wavelength of the SBR, and the thickness of the defect cavity layer. These findings suggest that high-Q TPP-like modes can be excited in a spherical geometry, with intriguing characteristics that may find applications for nano-lasing and other resonantly-enhanced light-matter interactions at the nanoscale. At present, the fabrication of such structures seems relatively difficult [40, 42], but the same type of resonance could also be observed in larger structures in a different wavelength range, allowing easier fabrication methods such as 3D-printing [180].

6.2 Theory of light scattering by multilayered spherical plasmonic nanoparticles

Metallic nanoparticles (NPs) have unique properties due to their size, particularly when compared to metal skin depth. At this size range, the electric field of incoming light can penetrate the metal and polarize the conduction electrons leading to collective oscillations [133, 134]. One fascinating property of these NPs is the emergence of localized surface plasmons (LSPs), non-propagating excitations distributed over the entire particle volume. The frequency of the plasmon resonance can be controlled by altering the dielectric properties of the surrounding medium or the NP's size,

shape, and composition [127]. This resonant interaction with light is illustrated in Figure 6-1, showing the calculated absorbance of an Au/SiO_2 core-shell nanosphere placed in air with a spacer cavity thickness of $t_{cavity} = 239\,nm$ and different Au radii, r_{core} = 20 nm, $r_{core} = 30\,nm$ and $r_{core} = 40\,nm$. The absorbance curves peak at around $520\,nm - 550\,nm$, related to the Au nanosphere's localized surface plasmon resonance (LSPR). The schematic view of the Au/SiO_2 core-shell nanosphere is also depicted.

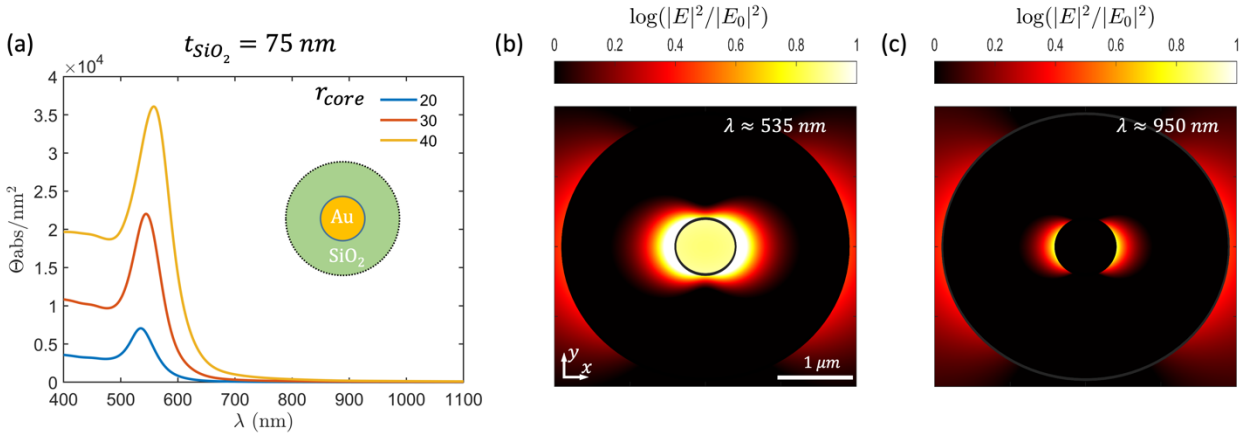

Figure 6-1 (a) Calculated Au/SiO_2 core-shell nanosphere absorbance with spacer cavity shell thickness $t_{cavity} = 239\,nm$ and different Au radius r_{core}. (Inserted) Schematic view of the Au/SiO_2 core-shell nanosphere. Normalized electric field intensity $|E|^2/|E_0|^2$ in (b) with $\lambda \approx 535\,nm$ and (c) $\lambda \approx 950\,nm$.

To further illustrate the plasmonic resonances and the electric field enhancement at the surface of the Au/SiO_2 core-shell nanosphere, the electric field distribution of the Au/SiO_2 nanosphere at $\lambda \approx 530\,nm$ and $\lambda \approx 950\,nm$ were simulated and depicted in Figure 6-1 (b) and (c), respectively. The electric field strength is normalized to its maximum value. At the LSPR wavelength ~530nm, the increased absorption substantially enhanced the electric field around the Au nanosphere. Interband transitions are the primary mechanism that causes loss in these gold nanoparticles in the high-energy end of the visible spectrum. This process involves exciting single particles from the occupied 5d valence band to the vacant levels of the 6s-6p conduction band in gold [245]. On the other hand, at $\lambda \approx 950\,nm$, the electric field distribution is more uniform and weaker. At these long wavelengths, Au can be characterized by the Drude model since it follows the behavior of free electron metals [127].

This study will emphasize a Tamm-like structure composed of a core-shell Au/SiO_2 nanoparticle and a Spherical Bragg Resonator (SBR) in the near-infrared (NIR) region where the intrinsic damping of Au is reduced. The complex dielectric function reported in [197] for Au and refractive index of $n_{\mathrm{L}} = 1.44$ for SiO_2 [196] and $n_{\mathrm{H}} = 1.75$ for TiO_2 [242] were utilized to conduct the theoretical calculations.

Our theoretical model follows the treatment of SBRs described in [165], using the transfer matrix method. Transfer matrices are commonly used to describe analytically the scattering properties of multilayered spherical structures, and efficient codes are available for their computation [112]. We make use of the relationship between T-matrix and S-matrix [112] to determine the S-matrix coefficients:

$$\bar{\bar{S}} \equiv \bar{\bar{I}} + 2\bar{\bar{T}} \tag{6-1}$$

where $\bar{\bar{I}}$ is the identity matrix.

The S-matrix is diagonalized due to the spherical geometry of our structures, which can be represented by the decoupling of electric and magnetic multipoles of order l in spherical coordinates. Thus, the S-matrix fully characterizes the scattering process for each multipole l and diagonal component p. Working with the S-matrix is advantageous as it enables direct identification of electromagnetic modes that can be excited in the structure. Specifically, we apply a Weierstrass factorization to each component p, corresponding to two singularities: poles and zeros [187]. Poles represent eigenmodes, while zeros are associated with perfect absorption [194], and their position describes the scattering properties of the system [187].

The normalized radiative decay rate (Γ) of a dipole located at the core center in multilayer spheres can be estimated using this transfer matrix by [30, 37]:

$$\frac{\Gamma_{\perp}}{\Gamma_0} = \frac{3}{2x_d^4}\frac{n_d}{n_h}\sum_l l(l+1)(2l+1)|f_{El}(x_d)|^2 \tag{6-2}$$

$$\frac{\Gamma_{\parallel}}{\Gamma_0} = \frac{3}{4x_d^4}\frac{n_d}{n_h}\sum_l (2l+1)[|f_{Ml}(x_d)|^2 + |f'_{El}(x_d)|^2] \tag{6-3}$$

where "$\perp$" and "$\parallel$" correspond to the perpendicular and parallel orientation of the dipole located at position d, n_{host} is the refractive index of the host medium, l is the angular quantum number, and $f_{\mathrm{El,Ml}}(\mathrm{x_d})$ are linear combinations of Riccati-Bessel functions multiplied by expansion coefficients determined through raising and lowering composite transfer matrices, while the prime represents

the differentiation with respect to the argument [30, 37]. The dimensionless size parameter is defined by $x_d = k_d r_d$ where $k_d = 2\pi n_d/\lambda$.

Also, for the case where a plane wave illuminates the SBR, the total absorption can be obtained from the S or T matrices as [30, 37]:

$$\theta_{abs} = \frac{\pi}{2k^2}\sum_{p,l}(2l+1)\left|1 - S_{pl}\right|^2 = \frac{\pi}{2k^2}\sum_{p,l}(2l+1)\left(1 - \left|1 + 2T_{pl}\right|^2\right) \qquad 6\text{-}4$$

where k is the wave vector.

For independent validation of the results, we have also used the Matlab package SPLAC by Etchegoin and Le Ru, which implements a slightly different recursive algorithm for multilayered spheres, also based on Mie theory [246, 247]. The accuracy of these algorithms for solving the Maxwell equations in different spherical multilayer plasmonic structures has been widely demonstrated in previous works [220, 242]. In our experience, the results of both codes show excellent agreement in simple structure, and in far-field cross-sections, but for near-field calculations involving many layers and high-quality resonances (as in Figure 6-8 below), the STRATIFY code appears to suffer from numerical instabilities, and we therefore relied on SPLAC for these near-field calculations.

6.3 Results and discussion

The 3D Tamm-like structure we propose is composed of a core-shell metal nanosphere structure embedded at the center of a SBR (metal-SBR), as sketched in Figure 6-2 (a). The core-shell structure consists of a gold core surrounded by a SiO_2 shell with radii of $r_{core} = 20\,nm$ and $t_{cavity} = 239\,nm$, respectively. The TiO_2/SiO_2 SBR surrounding the core-shell structure is designed to act as a Bragg mirror at the Bragg wavelength $\lambda_B \approx 950\,nm$. The SBR shell thickness was fixed at $L_{SiO2} = \lambda_B/4n_L = 163.79\,nm$ and $L_{TiO2} = \lambda_B/4n_H = 135.71\,nm$. A plane wave propagating in the x direction and linearly polarized along z is used as the excitation source and the host medium is air ($n_{\mathrm{host}} = 1$).

The absorption characteristics of the Tamm-like structure were analyzed by varying the number of SBR layers from $N = 10$ to $N = 30$, and the results are presented in Figure 6-2 (b). The calculated absorbance of the metal–SBR structure presents a sharp peak in the absorption cross-section, with maximum amplitude reaching $\sim 10^4 nm^2$, at around $\lambda \approx 900\,nm$. We attribute this distinctive

spectral feature to the excitation of a Tamm plasmon-like mode, confined between the spherical Bragg reflector and the metal core nanosphere. Note that this resonance wavelength is far detuned from the localized plasmon resonance of the core-shell particle (Figure 6-1, resonance at 535nm); this new mode has a distinct character, involving both photonic and plasmonic features. As the number of SBR layers increases, the absorption increases, and the peak becomes narrower. Importantly, the absorption maximum in this metal-SBR structure coincides with a large increase in the electromagnetic field. Furthermore, another peak starts to be noticeable around $\lambda \approx 950\,nm$ when the number of SBR layers exceeds $N = $ -20 . The increased absorption with the number of SBR layers also indicates the potential for achieving higher-Q plasmonic microcavities. These findings are promising for various applications, such as sensing and optoelectronics.

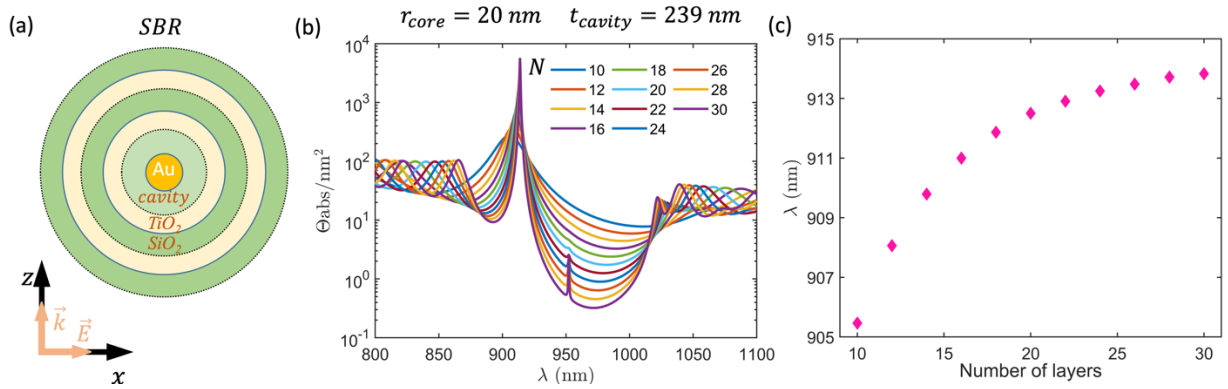

Figure 6-2 (a) Schematic view of the proposed Tamm plasmon-like resonance supporting structure, composed of a TiO_2/SiO_2 SBR with an Au/SiO_2 core-shell metal nanosphere structure in the core. (b) Calculated absorbance of the Tamm plasmon-like resonance supporting structure of Au radius $r_{core} = 20\,nm$, spacer cavity shell thickness $t_{cavity} = 239\,nm$, and Bragg wavelength $\lambda_B \approx 950\,nm$ excited by a plane wave varying the number of the SBR layers from 10 to 30. (c) Wavelength dependence of the maximum absorption with the number of SBR layers.

The wavelength dependence of the maximum absorption with the number of SBR layers is presented in Figure 6-2 (c). It is observed that the absorption maximum of the metal-SBR moves towards higher frequencies as the number of SBR layers increases. This shift is attributed to the introduction of a phase change between the reflected wave by the SBR and by the metal core, thereby influencing the observed absorption behavior.

In the following, we will concentrate on a Tamm-like structure consisting of an Au/SiO_2 core-shell nanosphere of radius $r_{core} = 20\,nm$ and shell thickness $t_{cavity} = 239\,nm$, surrounded by a 30-layer TiO_2/SiO_2 SBR with Bragg wavelength $\lambda_B \approx 950\,nm$. A detailed study of their eigenmodes was performed to obtain the resonant condition of the metal-SBR structure. Figure 6-3 presents the maps obtained of the S_{pl} matrix component of order $l = 1$ and $l = 2$ in the complex frequency plane for TE and TM polarization. The circumferences in the maps indicate the two lowest-order modes of the structure, namely TE1 and TM2. It is observed that the absorption maximum of the metal-SBR structure coincides with the electric dipole core mode TE1 of the structure. The electric dipole mode TE1 is a Tamm-like mode that is confined between the Au core and the TiO_2/SiO_2 SBR. This agrees with the result presented in Figure 6-2 (b) and corroborates that the absorption peak at around $\lambda \approx 913\,nm$ is due to the excitation of a Tamm-like mode. On the other hand, with the other absorption peak observed at $\lambda \approx 950\,nm$ in Figure 6-2 (b) is identified as the magnetic quadrupole mode TM2.

In order to illustrate the Tamm-like mode's influence on a dipole emitter, namely the loss and local density of states, Figure 6-4 presents the radiative decay rate enhancement of an electric dipole in the spacer layer of the 30-layer TiO_2/SiO_2 metal-SBR structure at a distance of $r = $ -22 nm from the Au nanosphere surface. Figure 6-4 (a) shows the perpendicular and parallel components of the radiative and non-radiative decay rates up to $l = 5$ and $l = 20$, plotted as solid and dashed lines, respectively. The perpendicular and parallel components of the radiative and non-radiative decay rates are directly proportional to the local density of states. The results shows a peak $\lambda \approx 913\,nm$ in the perpendicular and parallel components of the decay rate and another peak at $\lambda \approx 950\,nm$ in the parallel component. The increased radiative decay rate indicates that the metal-SBR structure promotes dipole emission, which is directly related to the enhanced electromagnetic field. It is also observed that there is no significant difference in the radiative decay rate between the $l = 5$ and $l = 20$, which implies that the performed calculation converged.

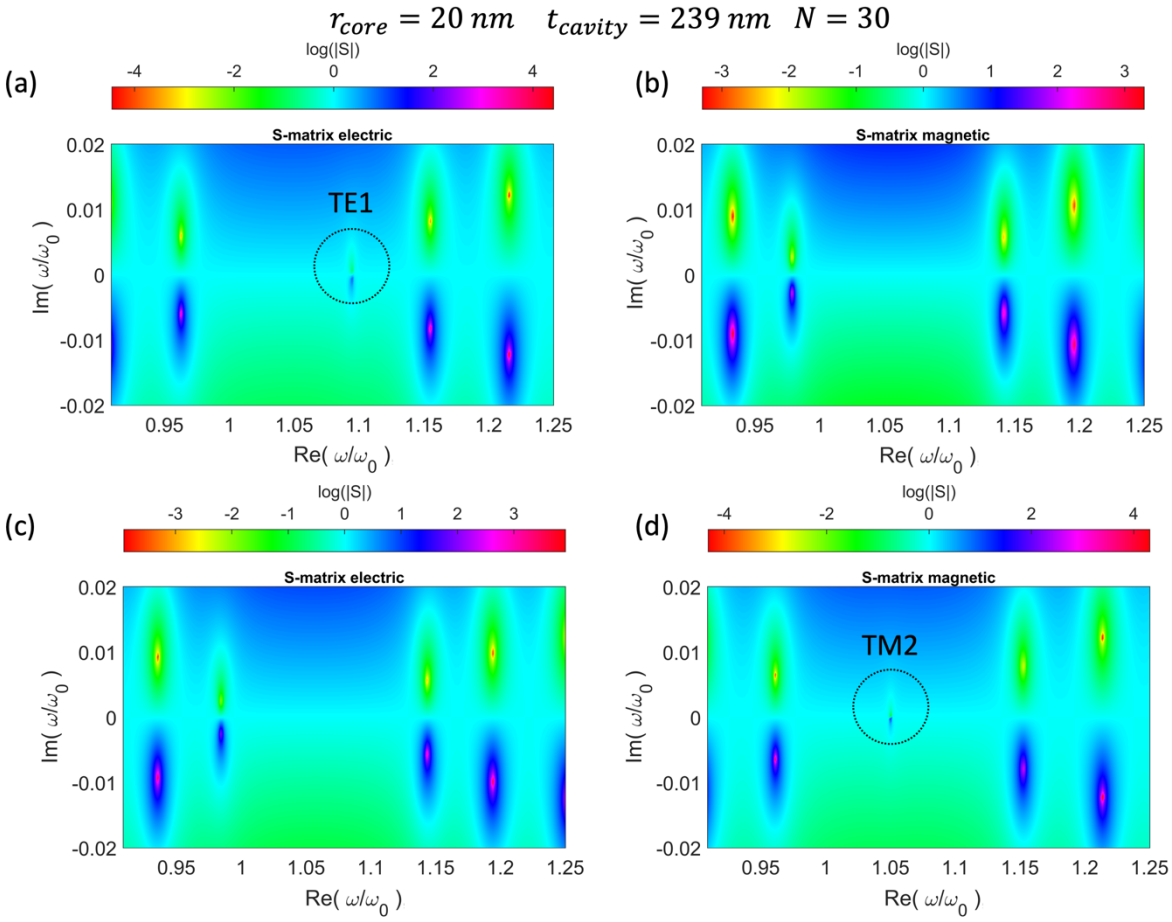

Figure 6-3 Maps of the S_{pl} matrix component of order $l = 1$ and $l = 2$ in the complex frequency plane for TE (a,b) and TM (c,d) polarization. The Tamm plasmon-like resonance supporting structure comprises an Au core with radius $r_{core} = 20\,nm$ and a SiO_2 spacer cavity shell thickness $t_{cavity} = 239\,nm$, surrounded by a 30-layer TiO_2/SiO_2 SBR with Bragg wavelength $\lambda_B \approx 950\,nm$. The circumferences signal the structure's two lowest-order modes, TE1 and TM2.

In particular, Figure 6-4 (b) and (c) show the dipole $l = 1$ and quadrupole $l = 2$ contributions to the perpendicular and parallel components of the radiative decay rate increase. Notably, the maximum at $\lambda \approx 913\,nm$ nm coincides with the TE1 mode obtained in Figure 6-3.. In addition, the maximum in the $l = 2$ dipolar contribution of the radiative decay rate coincides with the magnetic quadrupole mode TM2. Overall, these results provide further evidence of the enhanced electromagnetic field in the metal-SBR structure, which promotes these dipole and quadrupolar emissions.

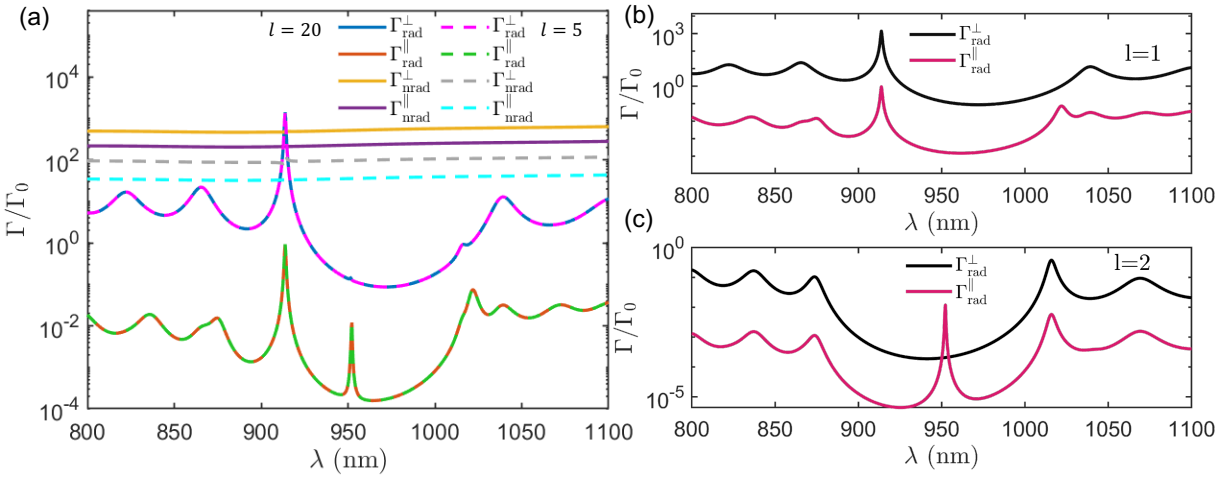

Figure 6-4 Radiative decay rate enhancement of an electric dipole placed in the cavity (spacer) shell of the 30-layer TiO_2/SiO_2 SBR at $r = 22\ nm$ from the surface of the Au core nanosphere. (a) Perpendicular and parallel components of the radiative and nonradiative decay rates up to other $l = 5$ and $l = 20$ are plotted as solid and dotted lines, respectively. (b) Dipolar $l = 1$ and (c) quadrupolar $l = 2$ contribution to perpendicular and parallel components of the radiative decay rate enhancement.

In Figure 6-5 (a), we can see the dependence of the radiative and non-radiative decay rate enhancement on the distance of the dipole from the Au nanosphere surface at $\lambda \approx 913\ nm$. It is observed that the enhancement of radiative and non-radiative decay rates is of the order of $\sim 10^2$ and $\sim 10^3$, respectively, for positions of the dipole near the Au nanosphere surface $r = -22\ nm$. This suggests that the metal-SBR structure enhances the decay rate of the dipole by at least one order of magnitude, which can have important implications for various applications such as sensing and lasing. Moreover, it is interesting to note that the distinction between the parallel and perpendicular components of the decay rate enhancement diminishes as we move farther from the surface of the Au nanosphere. The difference between the parallel and perpendicular components becomes negligible, indicating that the enhancement does not depend on the dipole's orientation.

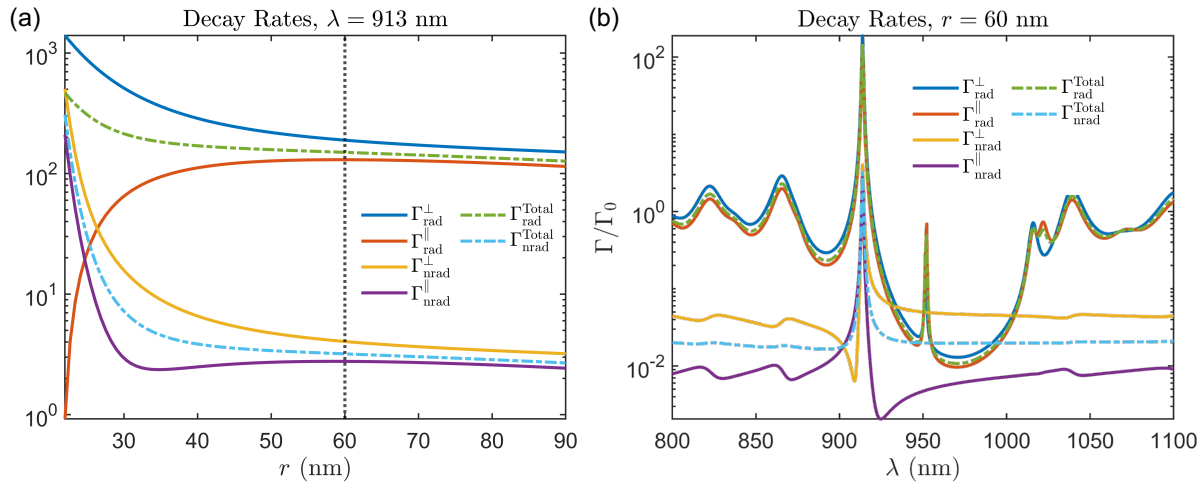

Figure 6-5 (a) Perpendicular, parallel, and total radiative and nonradiative decay rate enhancement dependency on the dipole distance from the Au nanosphere surface r at $\lambda \approx 930\ nm$. (b) Radiative decay rate enhancement of an electric dipole in the spacer shell of the metal-SBR structure at $r = 60\ nm$ from the surface of the Au nanosphere.

The previously reported decrease in the nonradiative decay rate for $r = 22\ nm$ ensures the possibility of improving the quantum efficiency ($\eta = \Gamma_{rad}/\Gamma_{rad} + \Gamma_{nrad}$) of a dipole placed in that region. In particular, for $r = 60\ nm$, the dipolar quantum efficiency is approximately ~0.9, and Figure 6-5 shows the radiative and nonradiative decay rate for this case. As noted, a maximum is observed at TE1 and TM2 frequencies, confirming the results obtained in Figure 6-4.

The decay rate enhancement for increasing numbers of layers in the TiO_2/SiO_2 SBR, with an Au radius of $r_{core} = 20\ nm$ and a spacer cavity shell thickness of $t_{cavity} = 239\ nm$, is depicted in Figure 6-6 (a). A maximum in the decay rate is appreciated at the TE1 dipole resonance wavelength. Its value increases, and the bandwidth becomes narrower as the number of layers increase. Furthermore, a second peak is also noticed at the TM2 resonance frequency. In addition, the enhanced decay rate stripes observed at wavelengths above $\lambda \approx 1050\ nm$ and around $\lambda \approx 825\ nm$ correspond to higher-order magnetic resonance modes. They are of the whispering gallery mode (WGM) type, as confirmed by near-field maps (not shown).

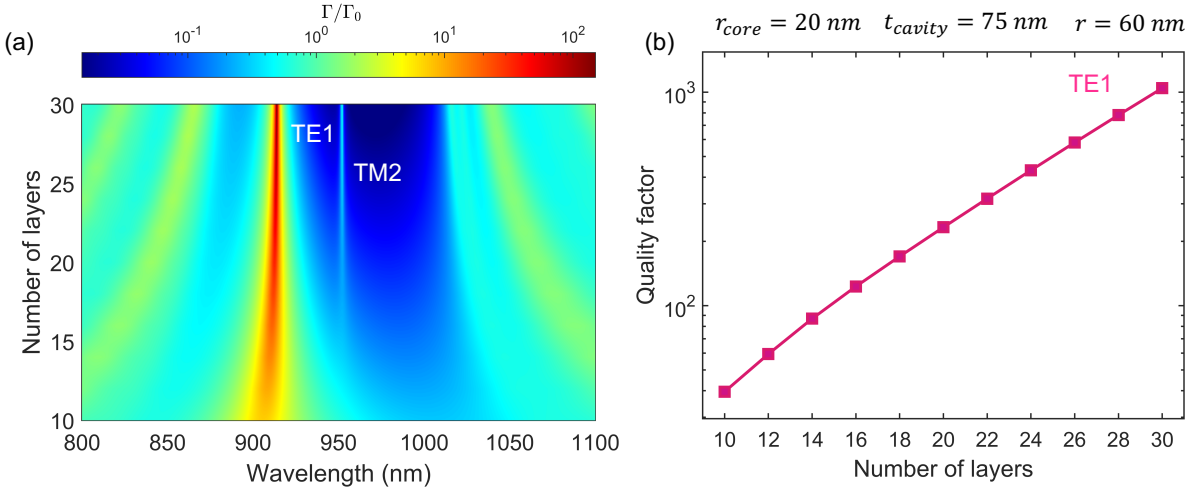

Figure 6-6 (a) Decay rate enhancement as a function of the number of layers of the TiO_2/SiO_2 SBR with Au radius core $r_{core} = 20\,nm$, spacer cavity shell thickness $t_{cavity} = 239\,nm$, and Bragg wavelength $\lambda_B \approx 950\,nm$. The dipolar electric and magnetic resonances are labeled by TE1 and TM1, respectively. (b) Calculated quality factor for a spherical Bragg resonator with a different number of layers at TE1 $\approx 913\,nm$.

The calculated quality factor $Q = \omega 0/\Delta\omega$ for the electric resonant dipole mode TE1 ($\lambda \approx$ -913 nm) in the spherical Bragg resonator as a function of different layers is shown in Figure 6-6 (b). A nonlinear relation between the quality factor and the number of layers was found. The results suggest that it is possible to obtain plasmonic Tamm modes with quality factors of $Q \approx$ -10^3 or even higher by coupling an Au nanosphere with an SBR. Such values are comparable to the quality factor of electric resonant dipole modes in SBR and the well-known whispering gallery modes, but here the mode volume is confined to the region immediately outside the core metal nanosphere. These findings are crucial as they demonstrate the possibility of strong coupling between an electric dipole and the plasmonic resonances in an metal-SBR structure. The results also highlight the significance of the number of layers in the metal-SBR structure in achieving high-quality plasmonic Tamm modes. We note that, similarly to the planar case, there will be a critical coupling condition [30] leading to maximum absorption, though for the parameters of this study the absorption simply increases with the number of layers.

As demonstrated in planar structures, choosing the materials and geometrical parameters is a key factor for TPP resonance [136, 143, 242]. Figure 6-7 shows the calculated absorbance of the Au

structure as a function of the spacer cavity shell thickness and Bragg wavelength. In Figure 6-7 (a), the radius of the Au core is fixed at $r_{core} = 20\,nm$, and the number of layers is $N = 30$, with a Bragg wavelength of approximately $\lambda_B \approx 950\,nm$. As the thickness of the SiO2 spacer cavity layer increases, the absorbance at the TE1 resonance frequency also increases, and the maximum peak of the absorbance shifts towards longer wavelengths. This shift can be attributed to the change in optical path length in the effective cavity defined between the metallic core and the enclosing SBR.

On the other hand, in Figure 6-7 (b), the spacer cavity shell thickness is fixed at $t_{cavity} = $ -239 nm, and the absorbance is plotted as a function of the wavelength for different values of the Bragg wavelength λ_B, which corresponds to different SBR layer thicknesses. When the Bragg wavelength is changed, an adjustment in the thicknesses of the SBR layers is intrinsically required, leading to a shift in the effective refractive index of the cavity mode. This modification of the refractive index directly influences the resonant condition of the cavity, resulting in the observed wavelength shift of the resonant mode.

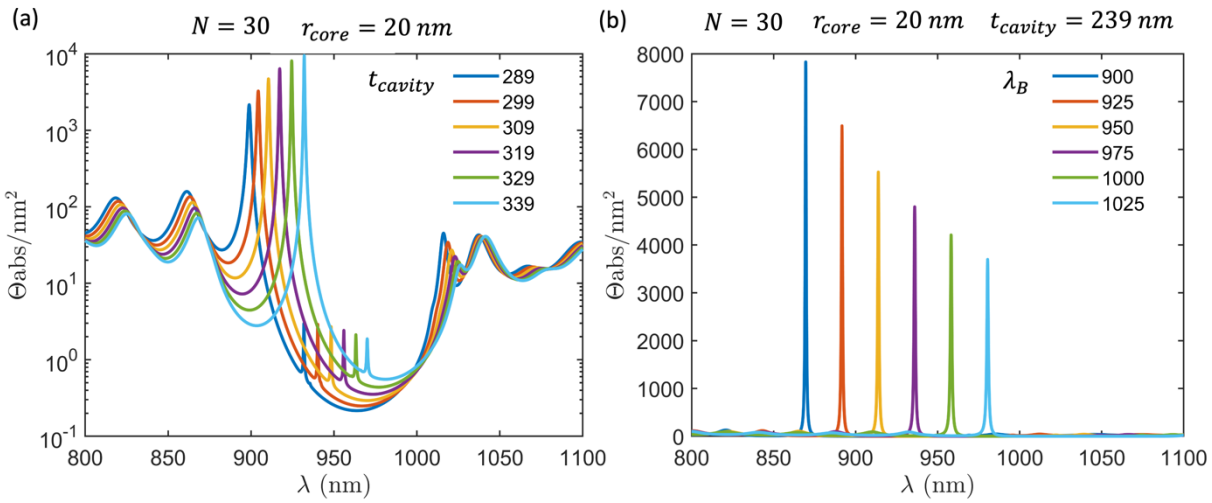

Figure 6-7 (a) The calculated absorbance of the metal-SBR structure with an Au radius $r_{core} = 20\,nm$, $N = 30$, and Bragg wavelength $\lambda_B \approx 950\,nm$, varying the spacer cavity shell thickness from $t_{cavity} = 289\,nm$ to $t_{cavity} = 339\,nm$ and (b) for different Bragg wavelengths λ_B and spacer cavity shell thickness $t_{cavity} = 239\,nm$.

Overall, the results highlight the critical role of fine-tuning the thickness of the spacer cavity layer and the Bragg wavelength for optimizing the absorbance of Tamm-like structures. By carefully

adjusting these parameters, achieving high absorbance at specific resonant frequencies is possible, which can be helpful for various applications in photovoltaics, sensing, and other light-matter applications relying on high local fields, 3D confinement, and small mode volume. We believe that our findings are expected to pave the way for developing novel plasmonic devices with improved performance and high-quality factor plasmonic resonances.

This paper proposes a novel Tamm plasmon-like resonance supporting structure by coupling an Au/SiO_2 core-shell metal nanosphere structure with a TiO_2/SiO_2 SBR. In Figure 6-8, the calculated electric field intensity distribution at $\lambda = 911\ nm$ is presented for the metal-SBR structure, where the Au/SiO_2 core-shell nanosphere of radius $r_{core} = 20\ nm$ and shell thickness $t_{cavity} = 239\ nm$, surrounded by a 30-layer TiO_2/SiO_2 SBR with Bragg wavelength $\lambda_B \approx 950\ nm$. Note the use of a logarithmic scale on the y-axis, as the local field is amplified by 3 orders of magnitude immediately outside the metal core (the incident plane wave is taken with a unit field amplitude $|E_0| = 1$). These near-field calculations were performed using the SPLAC Matlab package [246, 247], which is an implementation of Mie theory for multilayered spheres focusing on nanophotonics and near-field applications. We found excellent agreement between both codes in far-field calculations, however the STRATIFY code appears to suffer from numerical instabilities in near-field calculations. The inserted image provides a closer view around the Au nanoparticle, with vertical dotted lines denoting the interfaces between layers. The examined mode is highly localized near the Au particle, with a field profile exhibiting evanescent decay on both sides of the metal/dielectric interface, akin to Tamm plasmon polaritons observed in conventional multilayered planar structures [135, 136] and the multilayered cylindrical system proposed by C. E. Little et al. [248]. The field profile within the Bragg layers decays rapidly but presents more complex intensity fluctuations than in a planar configuration.

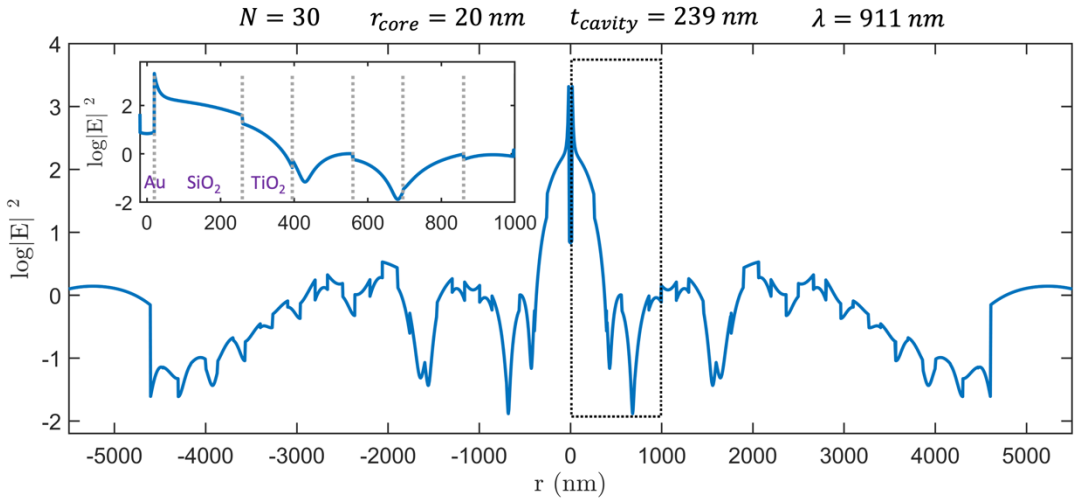

Figure 6-8 Calculated electric field intensity distribution of the metal-SBR structure with an Au radius $r_{core} = 20\ nm$, $N = 30$, Bragg wavelength $\lambda_B \approx 950\ nm$, and spacer cavity shell thickness $t_{cavity} = 239\ nm$ at $\lambda = 911\ nm$. Inserted figure: Zoom around the Au nanoparticle, the vertical dotted lines denote the layers interface.

The achievement of a Tamm-like mode with a low-index dielectric adjacent to the metal is very intriguing, particularly when contrasted with the behavior observed in planar geometries. In the planar multilayer geometry, the cavity layer between DBR and metal must be of high refractive index, to allow the existence of a Tamm plasmon mode. In the case of a low refractive index cavity, the presence of sharper absorbance has been attributed to a coupling between the cavity mode and a TPP mode [249]. Here, both high-index or low-index cavities allow the existence of a confined mode resembling a Tamm plasmon, in the spherical geometry. We have focused on the low-index cavity case, but the high-index configuration shows similar features, albeit at a different resonance wavelength. One potential explanation is that, unlike planar geometries, the spherical symmetry of the SBR allows for separating electric and magnetic components and introduces the possibility of distinct phase-matching conditions for each polarization. While the term "Tamm-like mode" has been employed in this work to describe the modes, due to the obvious analogy with the planar geometry, it becomes apparent that their exact character will require a deeper analytical exploration to fully understand how the phase matching condition characterizing planar TPPs translates in the spherical geometry. This revelation adds a layer of complexity to the behavior of SBRs, necessitating further investigation to comprehend their intricacies fully.

This questions surrounding the nature and connection of the observed modes in our SBRs to the original Tamm plasmon concept underscores the richness and complexity of these 3D cavity structures. Our work sheds light on the unique characteristics of SBRs and catalyzes future research endeavors to unravel their potential applications in photonics, optoelectronics, and various related fields. As we continue to explore the intricacies of SBRs, we advance our understanding of these resonant modes and pave the way for innovative technological applications, thus driving progress in advanced electromagnetic emission engineering and lasing applications.

6.4 Conclusion

Our theoretical investigation has proposed a novel Tamm-like resonance supporting structure with promising optical properties. The coupling of an Au/SiO2 core-shell metal nanosphere structure with a TiO2/SiO2 SBR results in a TPP-like mode that induces a peak in the SBR bandgap region due to the coupling between the localized plasmon resonance of the core metal particle and defect modes in the SBR. Our results demonstrate that the TPP-like mode characteristics depend on the Bragg wavelength, the number of layers of the SBR, and the thickness of the defect cavity layer. The study also finds that a dipole's radiative and non-radiative decay rates at a distance of $r = 60\ nm$ from the Au nanosphere surface result in a high quantum efficiency of $\sim 90\%$. A 30-layer metal-SBR structure also yields TPP-like modes with a high-quality factor of up to $\sim 10^3$, making this structure a potential candidate for switches, optical logic computing devices, and nonlinear applications. Overall, our work opens a new avenue for generating high-Q TPP-like modes and provides valuable insights into the design and optimization of resonant nano-spherical structures for various applications in photonics and optoelectronics.

6.5 Funding, acknowledgments, and disclosures

6.5.1 Funding

Natural Sciences and Engineering Research Council of Canada (Discovery grants, Strategic Research grants).

6.5.2 Acknowledgments

R. Kashyap acknowledges financial support for the Canadian NSERC Discovery grants and Strategic Research grants programs.

6.5.3 Disclosures

The authors declare no conflicts of interest.

6.5.4 Data availability

Data underlying the results presented in this paper are not publicly available at this time but may be obtained from the authors upon reasonable request.

CHAPTER 7. GENERAL DISCUSSION

This chapter comprehensively discusses the overall results obtained in this thesis. The primary focus is on the main characteristics of Spherical Bragg Resonators (SBRs) and the unique features exhibited by millimeter-sized SBRs fabricated using 3D printing technology. We also delve into the versatility and potential of SBRs in manipulating electromagnetic properties, enhancing light emission, and designing innovative Tamm plasmonic structures, as explored in the individual papers.

7.1 Characterization of Spherical Bragg Resonators

The Spherical Bragg Resonator (SBR) is a fascinating photonic crystal characterized by its omnidirectional nature and spherical symmetry. However, replicating thin layers with a consistent chemical composition on microscopic spherical particles remains challenging, hindering comprehensive experimental characterization of SBRs and exploring their prospective applications. The first paper focuses on an experimental investigation and numerical validation of the performance of Spherical Bragg Resonators (SBRs) produced using 3D printing technology, which offers a scalable and accessible method for producing these resonators.

One key aspect of SBRs is their ability to manipulate electromagnetic properties. Through experimental and numerical analysis, we investigated the frequency dependencies of reflection and transmission coefficients and the density of photonic states within the SBRs. As was mentioned and discussed in Chapter 3, the density of photonic states experiences a significant increase within the eigenmodes of the cavity and at the boundaries of the photonic bandgap.

Our findings revealed that SBRs could significantly alter the density of electromagnetic states compared to free space. One of the notable implications of the altered density of electromagnetic states in SBRs is its impact on spontaneous emission processes. SBRs can effectively enhance or inhibit the spontaneous emission of light, depending on the specific configuration and design parameters. This property has significant implications for various applications in the field of photonics. It opens possibilities for applications in dielectric nanoantennas and optoelectronic devices across the electromagnetic spectrum, as we discussed in Articles 2, 3 and 4.

7.2 Spherical Bragg Resonator for lasing

In our second article, we comprehensively investigated achieving optical amplification and lasing in Si/SiO_2 Bragg onion resonators by introducing a gain medium at the core. Our study yielded cavity quality factor (Q) values exceeding 10^4 for a relatively small number of layers, precisely 12 layers. These Q values are comparable to those observed in well-known whispering-gallery modes, renowned for their strong light confinement and extended photon lifetimes [34]. This implies that our Si/SiO_2 Bragg onion resonators exhibit exceptional energy confinement and low loss, making them highly promising for optical amplification and lasing applications. Furthermore, our investigation revealed that the modal volume of the resonators remained nearly constant within the range of layers studied. The modal volume represents the spatial extent to which the electromagnetic field is confined within the resonator. We found that the modal volume of the Si/SiO_2 Bragg onion resonators was on the order of $(\lambda_0/n)^3$, where λ_0 is the wavelength and n is the refractive index of the core material. Our Si/SiO_2 Bragg onion resonators offer a unique platform for efficient light-matter interactions by achieving high Q values and small modal volumes simultaneously. The strong energy confinement within the resonator facilitates enhanced light-matter coupling, crucial for optical amplification and lasing.

In addition, we analyzed the scattering properties of the Si/SiO_2 Bragg onion resonators in terms of total scattering efficiencies (Ω_{sca}). These efficiencies were computed by considering the contributions of electric TE and magnetic TM multipole moments. Our results revealed distinct peaks and dips in the scattering efficiencies, reflecting the presence of resonant and anti-resonant modes within the SBR.

In our study, a gain medium was incorporated into the model by introducing an imaginary negative part to the refractive index. Specifically, we investigated using a 12-layer SBR core doped with Er^{3+} as the gain medium, where the gain factor (γ) represents the amplification or absorption property of the material. By considering the refractive index of the doped core as $n_{core} = n_o + i\gamma$, where n_o is the real part, and γ is the negative imaginary part, we effectively modeled the behavior of the gain medium within the SBR structure. The parameter γ, or gain factor, is related to the material gain (g) through the equation $g = 4\pi\gamma/\lambda$, where λ is the free-space wavelength. It is important to note that a nonlinear permittivity function must be considered for describing the post-

threshold operation. Nonlinear effects become significant when the gain exceeds the threshold value, leading to the complex and dynamic behavior of the SBR structure. We utilized two methods to determine the gain threshold for achieving lasing in the SBR system: the scattering efficiencies method and the pole-zero analysis of the S-matrix. These methods complement each other and provide a comprehensive understanding of the amplification regime and confirmation of the lasing condition.

By studying the scattering efficiencies using the transfer matrix method, we identified the gain threshold at which the net radiation and material losses in the SBR are compensated, leading to the lasing regime. This compensation is simultaneously associated with a pole of the S-matrix in the complex frequency plane. As the gain increases, the pole shifts from the lower complex plane towards the real frequency axis. The distance from the pole to the real axis, determined by the total system loss, defines the mode's Q factor and decay rate. Therefore, lasing requires an active medium and a pole in the S-matrix to compensate for material and radiative losses. This condition is achieved when a high Purcell factor is attained, indicating the presence of strong feedback in the system.

The gain factor threshold for the lasing regime is strongly influenced by the number of layers in the SBR. This observation aligns with the exponential growth of the Purcell factor, as discussed in Article 2. As we reported, a 12-layer structure makes it possible to achieve the lasing regime with an Er^{3+}-doped SiO_2 core concentration of $\sim 5.63 \times 10^{20}\ ions/cm^3$, as the threshold gain factor is reduced to $\gamma \approx 5.00 \times 10^{-5}$ from $\gamma \approx 10^{-3}$ for a 6-layer structure.

These findings highlight the dependence of the lasing threshold on the number of SBR layers and the dopant concentration. They provide important insights into the design and optimization of SBR structures for achieving efficient lasing operations. By understanding the requirements for the lasing regime, it becomes possible to tailor the SBR system to meet specific lasing criteria and advance the development of novel laser devices based on SBRs.

7.3 Nanoantenna-Spherical Bragg Resonator coupled system

This study presents a novel approach for enhancing magnetic fields in all-dielectric nanoantennas by incorporating Spherical Bragg Resonators (SBR). These SBR structures offer the potential to

amplify magnetic transitions in quantum emitters, making them promising candidates for various applications [26, 29]. In this section, we investigate the coupling between the dipolar magnetic resonance of a SiO_2/Si core-shell spherical nanoantenna and the SBR TM1 defect mode to enhance the modal magnetic field.

To quantify the enhancement, we calculate the scattering efficiencies (Ω_{sca}) of the coupled nanoantenna-SBR system using the coefficients of the T-matrix, as described in detail by [30, 31]. The TM1 peak corresponds to the resonant magnetic dipole mode and exhibits characteristics similar to Fabry-Perot resonances. Our calculations reveal that it is possible to achieve magnetic resonant dipole modes with high-quality factors (Ω_{sca}) of approximately 10^5 or even higher when coupling dielectric nanoantennas with an SBR. These Q values are comparable to the high-quality factors observed in electric resonant dipole modes in SBRs and well-known whispering gallery modes.

The combined effect of the Bragg reflection phenomenon and the high-quality factor of the nanophotonic omnidirectional cavity contributes to a significant increase in the magnetic field in all directions. The central magnetic field generated within the SBR arises from the magnetic dipole moment induced in the y-axis direction due to the currents induced by the incident electromagnetic wave propagating along the x-direction.

This research focused on enhancing the interaction between dipole emitters and resonant photonic structures by utilizing the magnetic Purcell factor (MPF). The MPF measures the improvement in the spontaneous emission rate of a dipole emitter when coupled with a resonant photonic structure. We conducted an analysis and found that increasing the number of SBR layers decreases the resonance bandwidth, resulting in a higher MPF. By carefully designing and adjusting the properties of the SBR, we can effectively control the MPF and achieve significant enhancements in the dipole emission of Eu^{3+} ions. This enhancement is essential for various applications, including efficient light sources, optical amplification, and quantum information processing.

Our analysis yields valuable insights into optimizing the SBR structure to maximize the magnetic Purcell effect and facilitate enhanced dipole emission. Specifically, we observed a remarkable increase in the magnetic Purcell factor of a Eu^{3+} dipolar emitter positioned at the center of a 4-layer SBR nanoantenna coupled system, where the obtained decay rate reaches a maximum value of

approximately 5600. This enhancement occurs at the frequency of the defect mode of the spherical resonator, as explained in Article 3.

When incorporating dielectric magneto-optical active materials, such as garnets [41-43], into the core of our coupled nanoantenna-SBR structure, it has the potential to function as a magnetophotonic crystal. These materials possess a dielectric tensor that includes non-diagonal (magneto-optical) elements, which result in polarization conversion through non-diagonal polarizability within the nanoantenna-SBR structure. The Faraday rotation effect is crucial in this process and is vital in various applications, including isolators, modulators, routers, baffles, sensors, and magnetometers [44-46].

Previous studies on resonant systems have revealed that the degree of electromagnetic field interaction with the magneto-optical material directly relates to polarization conversion. In the case of core-shell spherical structures, prior research has demonstrated a substantial enhancement of up to five times in magneto-optical polarization conversion at the positions of magnetic dipolar (MD) and magnetic quadrupolar (MQ) resonances [41]. Consequently, by coupling a dielectric nanoantenna with SBRs at the MD resonance, the electromagnetic field enhancement can significantly improve magneto-optical polarization conversion.

7.4 Tamm plasmonic Spherical Bragg Resonator

Tamm plasmonic structures have gained significant attention due to their unique optical properties and potential applications in photonics and optoelectronics. Article 4 proposes a novel Tamm plasmon-like resonance supporting structure by coupling an Au/SiO_2 core-shell metal nanosphere structure with a SiO_2/TiO_2 SBR. We investigate the near-infrared scattering properties of this structure and explore its potential for generating high-quality Tamm plasmon-polariton (TPP) like modes. Our theoretical analysis focuses on the coupling between the TPP and defect modes in the SBR and the radiative and non-radiative decay rates of a dipolar magnetic emitter near the Au nanosphere surface.

The coupling of the Au/SiO_2 core-shell metal nanosphere structure with the SiO_2/TiO_2 SBR results in a TPP mode. Our theoretical absorption results reveal a peak in the SBR bandgap region, which can be attributed to the coupling between the TPP and defect modes in the SBR. This coupling

effect allows for precise control and manipulation of the TPP mode within the desired spectral range. By engineering the parameters of the SBR, such as the number of layers and the Bragg wavelength, we can tailor the TPP mode to specific frequencies of interest. This bandgap engineering capability opens new possibilities for various applications requiring selective and efficient light manipulation.

We also analyze the radiative and non-radiative decay rates of a dipolar magnetic emitter positioned at a distance of $r = 60\ nm$ from the Au nanosphere surface. The results demonstrate a remarkably high quantum efficiency of approximately 90%. This finding highlights the potential of the proposed Tamm plasmonic structure for enhancing light-matter interactions and enabling efficient energy transfer processes. The high quantum efficiency is crucial for applications such as optical amplification, lasing, and sensing, where maximizing the emission and absorption rates is vital.

Further investigation of the Tamm plasmonic structure reveals that a 30-layer SBR Tamm structure yields TPP modes with a high-quality factor of up to $\sim 10^3$. The quality factor characterizes the sharpness and narrowness of the TPP resonance, indicating minimal losses and strong confinement of the optical mode. This remarkable quality factor makes the proposed structure a promising candidate for applications requiring high-Q TPP modes.

The potential applications of the proposed Tamm plasmon-like resonance supporting structure Tamm plasmonic structure with high-quality TPP modes are vast. The structure's unique optical properties make it suitable for sensing, trapping, and enhancing light-matter interactions. Switches, optical logic computing devices, and nonlinear applications could benefit from the precise control and manipulation of light achieved through TPP modes. The findings from this study provide valuable insights into the design and optimization of Tamm plasmonic structures, paving the way for future advancements in photonics and optoelectronics.

CHAPTER 8. CONCLUSION AND RECOMMENDATIONS

The study and application of photonic resonators represent a dynamic and rapidly evolving field, continually unveiling new possibilities for photonics and optoelectronic technologies. The significant progress in this area holds immense potential for integrated photonics, quantum optics, optical computing, and biosensing, promising breakthroughs and advancements in these fields. Spherical Bragg Resonators (SBRs) have emerged as promising structures among the various photonic microcavity candidates. Their unique ability to generate a perfect omnidirectional photonic band gap and effectively confine light makes them an attractive option for developing high-quality factor microcavities and enhancing light-matter interactions. Throughout this Ph.D. research, we have extensively explored innovative Spherical Bragg Resonator (SBR)-based systems. Our general objective has been to push the boundaries of design and material systems, delving deep into the modeling and optimization of SBR devices. It has created four distinct investigation avenues, each forming the basis of the papers presented in this Thesis.

The first article explores, for first time, millimeter-sized SBRs fabricated using 3D printing technology. Through experimental and numerical analysis, the frequency dependencies of reflection and transmission coefficients, as well as the density of photonic states in SBRs, are examined. The study also investigates the influence of the source position on the resonator's electromagnetic wave energy. The results demonstrate that SBRs can manipulate the density of electromagnetic states, offering potential enhancements or inhibitions in spontaneous emission processes. These findings prompted our in-depth exploration, modeling, and optimization of different SBR-based systems. The goal was to harness their potential in a wide range of functionalities, such as lasers, nanoantennas, and plasmonic devices. These aspirations comprised the objectives of the following three papers.

In the second article, the emphasis was on Si/SiO_2 SBRs with Er^{3+} doping in the core, focusing on optimizing the SBR geometry using experimentally derived refractive index and dopant concentration values. The outcomes reveal the onion resonator's exceptional potential for spontaneous emission engineering, as evidenced by its high-quality factor and small modal volume. Beyond resonance frequencies, the system functions as an optical amplifier when overcompensated, while achieving loss compensation around resonance frequencies triggers laser-like behavior. The model used accurately predicts lasing generation wavelength and threshold gain.

However, a future study considering a nonlinear permittivity function is needed for a more general characterization of the post-threshold operation in Si/SiO_2 SBRs with Er^{3+} doping. Through optimization of layer count, the scattering efficiency for the dipolar core mode is amplified, subsequently reducing the threshold gain factor for lasing. This investigation proposes a promising strategy for achieving threshold-less lasers via SBRs, delivering valuable insights for practical experimental showcases.

One of the key advantages of Spherical Bragg Resonators discussed and demonstrated through this Thesis is their omnidirectional nature. Being omnidirectional photonic crystals with high-quality factor resonant modes, they exhibit minimal dependence on emitter polarization regarding the total decay rate. This characteristic is reflected in the high values obtained for both the perpendicular and parallel components of the decay rate, observed in the context of a Eu^{3+} emitter emission using a SiO_2/Si core-shell spherical nanoantenna coupled with an SBR. In our third manuscript, we have achieved an unprecedented enhancement in the radiative decay rate, exceeding 10^3. The omnidirectionality of the SBR is particularly beneficial for the fabrication process as it allows for high decay rate values regardless of the orientation of the magnetic dipole. The findings suggest the potential of the coupled SBR-nanoantenna system for efficient light emission and manipulation at the nanoscale. Moreover, its prospect extends to a wide range of applications, such as routers, modulators, magnetometers, and sensors. This is due to its prospective to operate as a magnetophotonic crystal when a dielectric magneto-optical active material is incorporated within the core.

A novel Tamm plasmon-like resonance supporting structure by coupling an Au/SiO_2 core-shell metal nanosphere structure with a SiO_2/TiO_2 SBR, was proposed in the fourth article. The study investigates the near-infrared scattering properties of the SBR Tamm plasmon system and demonstrates a peak in the SBR bandgap region due to the coupling between the Tamm plasmon polariton (TPP) and defect modes in the SBR. The results show a high-quality factor for TPP modes and a high quantum efficiency for radiative decay rates. The study presents new possibilities for generating high-Q TPP modes and offers insights into the design and optimization of Tamm plasmonic structures for various applications in photonics and optoelectronics.

Overall, this thesis presents the first-time demonstrations of several key advancements in Spherical Bragg Resonators (SBRs). We successfully fabricated millimeter-sized SBRs using 3D printing technology, optimized for microwave and radio frequency applications, and conducted comprehensive measurements and characterizations to validate their performance. Our work introduced a novel Tamm plasmon-like resonance supporting structure consisting of an Au/SiO_2 core-shell metal nanosphere surrounded by a TiO_2/SiO_2 SBR, achieving a quality factor (Q) of up to $\sim 10^3$. Furthermore, we provided the first theoretical demonstration of engineering optical amplification and threshold gain for lasing within SBRs. By coupling magnetic dipole nanoantenna resonances with SBR modes, we significantly enhanced the modal magnetic field, with a 4-layer SiO2/Si SBR yielding a Purcell factor of approximately 5×10^3, the highest reported in the literature. These pioneering efforts not only validate the feasibility of using 3D printing for SBR fabrication but also open new avenues for high-Q resonant modes, optical switching, logic computing devices, and nonlinear optical applications, demonstrating the immense potential of SBRs in advancing optical and photonic technologies.

As with any pioneering research, this study has also highlighted several areas that warrant further investigation. For instance, exploring new materials with tailored properties could potentially lead to even more optimized and specialized resonator designs. Moreover, investigating the integration of SBRs with other photonic components might offer intriguing opportunities for developing complex and versatile devices.

Looking forward, the findings and knowledge presented in this thesis serve as solid foundations for continued research in this exciting field. It is hoped that this work will inspire and encourage researchers and engineers to explore new frontiers in SBR-based technologies, ultimately leading to transformative advancements that impact various industries and improve our daily lives. Through collaborative efforts and a commitment to scientific exploration, we can unlock the full potential of Spherical Bragg Resonators and contribute to the progress of photonics and optoelectronics.

REFERENCES

[1] C. Kittel, and P. McEuen, *Introduction to solid state physics*: John Wiley & Sons, 2018.

[2] E. Yablonovitch, "Photonic Band-Gap Structures," *Journal of the Optical Society of America B-Optical Physics,* vol. 10, no. 2, pp. 283-295, Feb, 1993.

[3] S. John, "Strong localization of photons in certain disordered dielectric superlattices," *Phys Rev Lett,* vol. 58, no. 23, pp. 2486-2489, Jun 8, 1987.

[4] S. G. J. John, Joannopoulos, D., Winn, J. N., & Meade, R. D., *Photonic crystals: molding the flow of light.*, second ed.: Princeton University of Press., 2008.

[5] K. Yasumoto, *Electromagnetic theory and applications for photonic crystals*: CRC press, 2018.

[6] G. J. Tang, X. T. He, F. L. Shi, J. W. Liu, X. D. Chen, and J. W. Dong, "Topological photonic crystals: Physics, designs, and applications," *Laser & Photonics Reviews,* vol. 16, no. 4, pp. 2100300, 2022.

[7] Y. Yun, A. Vetter, R. Stegmueller, S. Ferrari, W. H. P. Pernice, C. Rockstuhl, and C. Lee, "Superconducting-Nanowire Single-Photon Spectrometer Exploiting Cascaded Photonic Crystal Cavities," *Physical Review Applied,* vol. 13, no. 1, Jan 29, 2020.

[8] H. Takano, B. S. Song, T. Asano, and S. Noda, "Highly efficient multi-channel drop filter in a two-dimensional hetero photonic crystal," *Opt Express,* vol. 14, no. 8, pp. 3491-6, Apr 17, 2006.

[9] S. Chakravarty, Y. Zou, W. C. Lai, and R. T. Chen, "Slow light engineering for high Q high sensitivity photonic crystal microcavity biosensors in silicon," *Biosens Bioelectron,* vol. 38, no. 1, pp. 170-6, Oct-Dec, 2012.

[10] K. M. L. a. Y. R. Liu, "Full Vector Wave Calculation of Photonic Band Structures in Face-Centered-Cubic Dielectric Media," *Phys. Rev. Lett.,* vol. 65, pp. 2646, 1990.

[11] E. Yablonovitch, and T. J. Gmitter, "Photonic band structure: The face-centered-cubic case," *Phys Rev Lett,* vol. 63, no. 18, pp. 1950-1953, Oct 30, 1989.

[12] P. Russell, "Photonic crystal fibers," *Science,* vol. 299, no. 5605, pp. 358-62, Jan 17, 2003.

[13] P. S. J. Russell, "Photonic-Crystal Fibers," *Journal of Lightwave Technology,* vol. 24, no. 12, pp. 4729-4749, 2006.

[14] X. Zheng, M. P. C. Taverne, Y. L. D. Ho, and J. G. Rarity, "Cavity Design in Woodpile Based 3D Photonic Crystals," *Applied Sciences-Basel,* vol. 8, no. 7, Jul, 2018.

[15] C. C. a. A. Fratalocchi, "Dynamic light diffusion, Anderson localization and lasing in disordered inverted opals: 3D ab-initio Maxwell-Bloch computation," *arXiv preprint arXiv:0802.3775,* 2008.

[16] P. S. Russell, P. Holzer, W. Chang, A. Abdolvand, and J. C. Travers, "Hollow-core photonic crystal fibres for gas-based nonlinear optics," *Nature Photonics,* vol. 8, no. 4, pp. 278-286, Apr, 2014.

[17] P. R. V. J. D. Joannopoulos, and S. Fan, *Photonic Crystals*, second ed., Princeton: Princeton University Press, 1995.

[18] M. Zeisberger, A. Hartung, and M. Schmidt, "Understanding Dispersion of Revolver-Type Anti-Resonant Hollow Core Fibers," *Fibers,* vol. 6, no. 4, 2018.

[19] A. Y. P. Yeh, "Theory of a Bragg fiber," *JOSA,* vol. 68(9), pp. 1196-1201, 1978.

[20] B. Temelkuran, S. D. Hart, G. Benoit, J. D. Joannopoulos, and Y. Fink, "Wavelength-scalable hollow optical fibres with large photonic bandgaps for CO2 laser transmission," *Nature,* vol. 420, no. 6916, pp. 650-653, 2002.

[21] E. Aslan, and E. Aslan, "Engineering the boosting of the magnetic Purcell factor with a composite structure based on nanodisk and ring resonators," *Journal of Electromagnetic Waves and Applications,* vol. 36, no. 10, pp. 1339-1351, 2022.

[22] D. Brady, J. E. Sipe, and G. Papen, "Spherical distributed dielectric resonators," *Journal of the Optical Society of America B,* vol. 10, no. 4, 1993.

[23] M. E. Tobar, J. M. Le Floch, D. Cros, J. Krupka, J. D. Anstie, and J. G. Hartnett, "Spherical Bragg reflector resonators," *IEEE Trans Ultrason Ferroelectr Freq Control,* vol. 51, no. 9, pp. 1054-9, Sep, 2004.

[24] K. G. Sullivan, and D. G. Hall, "Radiation in spherically symmetric structures. II. Enhancement and inhibition of dipole radiation in a spherical Bragg cavity," *Phys Rev A,* vol. 50, no. 3, pp. 2708-2718, Sep, 1994.

[25] U. Biswas, C. Nayak, and J. K. Rakshit, "Fabrication techniques and applications of two-dimensional photonic crystal: history and the present status," *Optical Engineering,* vol. 62, no. 1, pp. 010901-010901, 2023.

[26] T. Li, G. Liu, H. Kong, G. Yang, G. Wei, and X. Zhou, "Recent advances in photonic crystal-based sensors," *Coordination Chemistry Reviews,* vol. 475, pp. 214909, 2023.

[27] M. Butt, S. N. Khonina, and N. Kazanskiy, "Recent advances in photonic crystal optical devices: A review," *Optics & Laser Technology,* vol. 142, pp. 107265, 2021.

[28] G. Burlak, S. Koshevaya, J. Sanchez-Mondragon, and V. Grimalsky, "Electromagnetic eigenoscillations and fields in a dielectric microsphere with multilayer spherical stack," *Optics Communications,* vol. 187, no. 1-3, pp. 91-105, Jan, 2001.

[29] G. N. Burlak, "Optical radiation from coated microsphere with active core," *Physics Letters A,* vol. 299, no. 1, pp. 94-101, Jun, 2002.

[30] A. Moroz, "A recursive transfer-matrix solution for a dipole radiating inside and outside a stratified sphere," *Annals of Physics,* vol. 315, no. 2, pp. 352-418, 2005.

[31] I. L. Rasskazov, A. Moroz, and P. S. Carney, "Electromagnetic energy in multilayered spherical particles," *JOSA A,* vol. 36, no. 9, pp. 1591-1601, 2019.

[32] R. Gaponenko, A. Moroz, I. L. Rasskazov, K. Ladutenko, A. Shcherbakov, and P. Belov, "Harnessing superdirectivity in dielectric spherical multilayer antennas," *Physical Review B,* vol. 104, no. 19, 2021.

[33] Y. Xu, W. Liang, A. Yariv, J. G. Fleming, and S. Y. Lin, "Modal analysis of Bragg onion resonators," *Opt Lett,* vol. 29, no. 5, pp. 424-6, Mar 1, 2004.

[34] M. A. Alzahrani, and R. C. Gauthier, "Spherical space Bessel-Legendre-Fourier localized modes solver for electromagnetic waves," *Optics Express,* vol. 23, no. 20, pp. 25717-37, Oct 5, 2015.

[35] I. L. Rasskazov, A. Moroz, and P. S. Carney, "Extraordinary Fluorescence Enhancement in Metal-Dielectric Core–Shell Nanoparticles," *The Journal of Physical Chemistry Letters,* vol. 12, no. 27, pp. 6425-6430, 2021.

[36] K. Imakita, H. Shibata, M. Fujii, and S. Hayashi, "Numerical analysis on the feasibility of a multi-layered dielectric sphere as a three-dimensional photonic crystal," *Optics Express,* vol. 21, no. 9, pp. 10651-10658, May, 2013.

[37] I. L. Rasskazov, P. S. Carney, and A. Moroz, "STRATIFY: a comprehensive and versatile MATLAB code for a multilayered sphere," *OSA Continuum,* vol. 3, no. 8, pp. 2290-2306, 2020.

[38] C. Deumie, P. Voarino, and C. Amra, "Overcoated microspheres for specific optical powders," *Appl Opt,* vol. 41, no. 16, pp. 3299-305, Jun 1, 2002.

[39] I. Gourevich, Field, L. M., Wei, Z., Paquet, C., Petukhova, A., Alteheld, A., ... & Sipe, J. E., "Polymer multilayer particles: a route to spherical dielectric resonators.," *Macromolecules,* vol. 39, pp. 1449-1454, 2006.

[40] H. Shibata, K. Imakita, and M. Fujii, "Fabrication of a core–shell–shell particle with a quarter-wave thick shell and its optical properties," *RSC Adv.,* vol. 4, no. 61, pp. 32293-32297, 2014.

[41] A. V. Medvedev, A. A. Dukin, N. A. Feoktistov, and V. G. Golubev, "A spherical distributed Bragg reflector based on a-Si1–xCx: H and a-SiO2 layers," *Technical Physics Letters,* vol. 43, no. 10, pp. 885-888, 2017.

[42] A. V. Medvedev, A. A. Dukin, N. A. Feoktistov, and V. G. Golubev, "Spherical Distributed Bragg Reflector with an Omnidirectional Stop Band in the Near-IR Spectral Range," *Semiconductors,* vol. 53, no. 7, pp. 901-905, 2019.

[43] M. Humar, and I. Muševič, "3D microlasers from self-assembled cholesteric liquid-crystal microdroplets," *Optics Express,* vol. 18, no. 26, pp. 26995-27003, 2010.

[44] E. M. Purcell, H. C. Torrey, and R. V. Pound, "Resonance absorption by nuclear magnetic moments in a solid," *Physical Review,* vol. 69, no. 1-2, pp. 37, 1946.

[45] A. L. Crook, C. P. Anderson, K. C. Miao, A. Bourassa, H. Lee, S. L. Bayliss, D. O. Bracher, X. Zhang, H. Abe, and T. Ohshima, "Purcell enhancement of a single silicon carbide color center with coherent spin control," *Nano letters,* vol. 20, no. 5, pp. 3427-3434, 2020.

[46] S. Noda, M. Fujita, and T. Asano, "Spontaneous-emission control by photonic crystals and nanocavities," *Nature Photonics,* vol. 1, no. 8, pp. 449-458, 2007.

[47] S. Wu, H. Xia, J. Xu, X. Sun, and X. Liu, "Manipulating luminescence of light emitters by photonic crystals," *Advanced Materials,* vol. 30, no. 47, pp. 1803362, 2018.

[48] W. Liang, Y. Huang, A. Yariv, Y. Xu, and S. Y. Lin, "Modification of spontaneous emission in Bragg onion resonators," *Optics Express,* vol. 14, no. 16, pp. 7398-419, Aug 7, 2006.

[49] P. Goy, J. Raimond, M. Gross, and S. Haroche, "Observation of cavity-enhanced single-atom spontaneous emission," *Physical Review Letters,* vol. 50, no. 24, pp. 1903, 1983.

[50] E. Yablonovitch, "Inhibited spontaneous emission in solid-state physics and electronics," *Phys Rev Lett,* vol. 58, no. 20, pp. 2059-2062, May 18, 1987.

[51] M. Moczała-Dusanowska, Ł. Dusanowski, S. Gerhardt, Y. M. He, M. Reindl, A. Rastelli, R. Trotta, N. Gregersen, S. Höfling, and C. Schneider, "Strain-tunable single-photon source based on a quantum dot–micropillar system," *ACS Photonics,* vol. 6, no. 8, pp. 2025-2031, 2019.

[52] Y. Wei, S. Liu, X. Li, Y. Yu, X. Su, S. Li, X. Shang, H. Liu, H. Hao, and H. Ni, "Tailoring solid-state single-photon sources with stimulated emissions," *Nature Nanotechnology,* vol. 17, no. 5, pp. 470-476, 2022.

[53] A. M. Adawi, A. Cadby, L. G. Connolly, W. C. Hung, R. Dean, A. Tahraoui, A. M. Fox, A. G. Cullis, D. Sanvitto, and M. S. Skolnick, "Spontaneous emission control in micropillar cavities containing a fluorescent molecular dye," *Advanced materials,* vol. 18, no. 6, pp. 742-747, 2006.

[54] M. Van Exter, G. Nienhuis, and J. Woerdman, "Two simple expressions for the spontaneous emission factor β," *Physical Review A,* vol. 54, no. 4, pp. 3553, 1996.

[55] E. Burstein, and C. Weisbuch, *Confined electrons and photons: New physics and applications*: Springer Science & Business Media, vol. 340, 2012.

[56] J. T. Robinson, C. Manolatou, L. Chen, and M. Lipson, "Ultrasmall mode volumes in dielectric optical microcavities," *Physical Review Letters,* vol. 95, no. 14, pp. 143901, 2005.

[57] R. Coccioli, M. Boroditsky, K. Kim, Y. Rahmat-Samii, and E. Yablonovitch, "Smallest possible electromagnetic mode volume in a dielectric cavity," *IEE Proceedings-Optoelectronics,* vol. 145, no. 6, pp. 391-397, 1998.

[58] P. B. Deotare, M. W. McCutcheon, I. W. Frank, M. Khan, and M. Lončar, "High quality factor photonic crystal nanobeam cavities," *Applied Physics Letters,* vol. 94, no. 12, 2009.

[59] J. D. Joannopoulos, P. R. Villeneuve, and S. Fan, "Photonic crystals: putting a new twist on light," *Nature,* vol. 386, no. 6621, pp. 143-149, 1997.

[60] M. Pelton, "Modified spontaneous emission in nanophotonic structures," *Nature Photonics,* vol. 9, no. 7, pp. 427-435, 2015.

[61] S. Ogawa, M. Imada, S. Yoshimoto, M. Okano, and S. Noda, "Control of light emission by 3D photonic crystals," *Science,* vol. 305, no. 5681, pp. 227-9, Jul 9, 2004.

[62] P. Lodahl, A. Floris van Driel, I. S. Nikolaev, A. Irman, K. Overgaag, D. Vanmaekelbergh, and W. L. Vos, "Controlling the dynamics of spontaneous emission from quantum dots by photonic crystals," *Nature,* vol. 430, no. 7000, pp. 654-657, 2004.

[63] T. Yoshie, J. Vučković, A. Scherer, H. Chen, and D. Deppe, "High quality two-dimensional photonic crystal slab cavities," *Applied Physics Letters,* vol. 79, no. 26, pp. 4289-4291, 2001.

[64] A. S. Solntsev, G. S. Agarwal, and Y. S. Kivshar, "Metasurfaces for quantum photonics," *Nature Photonics,* vol. 15, no. 5, pp. 327-336, 2021.

[65] N. Rivera, and I. Kaminer, "Light–matter interactions with photonic quasiparticles," *Nature Reviews Physics,* vol. 2, no. 10, pp. 538-561, 2020.

[66] D. G. Baranov, M. Wersall, J. Cuadra, T. J. Antosiewicz, and T. Shegai, "Novel nanostructures and materials for strong light–matter interactions," *Acs Photonics,* vol. 5, no. 1, pp. 24-42, 2018.

[67] Y. Akahane, T. Asano, B.-S. Song, and S. Noda, "High-Q photonic nanocavity in a two-dimensional photonic crystal," *Nature,* vol. 425, no. 6961, pp. 944-947, 2003.

[68] Z. Zhang, and M. Qiu, "Small-volume waveguide-section high Q microcavities in 2D photonic crystal slabs," *Optics Express,* vol. 12, no. 17, pp. 3988-3995, 2004.

[69] A. Chutinan, and S. Noda, "Waveguides and waveguide bends in two-dimensional photonic crystal slabs," *Physical review B,* vol. 62, no. 7, pp. 4488, 2000.

[70] P. Ji, C. Qian, J. J. Finley, and S. Yang, "Thickness insensitive nanocavities for 2D heterostructures using photonic molecules," *Nanophotonics,* vol. 12, no. 17, pp. 3501-3510, 2023.

[71] B.-S. Song, S. Noda, T. Asano, and Y. Akahane, "Ultra-high-Q photonic double-heterostructure nanocavity," *Nature materials,* vol. 4, no. 3, pp. 207-210, 2005.

[72] D. Englund, A. Faraon, I. Fushman, N. Stoltz, P. Petroff, and J. Vučković, "Controlling cavity reflectivity with a single quantum dot," *Nature,* vol. 450, no. 7171, pp. 857-861, 2007.

[73] A. Bennett, M. Pooley, R. Stevenson, M. Ward, R. Patel, A. B. de La Giroday, N. Sköld, I. Farrer, C. Nicoll, and D. Ritchie, "Electric-field-induced coherent coupling of the exciton states in a single quantum dot," *Nature Physics,* vol. 6, no. 12, pp. 947-950, 2010.

[74] A. Lyasota, S. Borghardt, C. Jarlov, B. Dwir, P. Gallo, A. Rudra, and E. Kapon, "Integration of multiple site-controlled pyramidal quantum dot systems with photonic-crystal membrane cavities," *Journal of Crystal Growth,* vol. 414, pp. 192-195, 2015.

[75] A. Gopinath, E. Miyazono, A. Faraon, and P. W. Rothemund, "Engineering and mapping nanocavity emission via precision placement of DNA origami," *Nature,* vol. 535, no. 7612, pp. 401-405, 2016.

[76] M. Barth, N. Nüsse, B. Löchel, and O. Benson, "Controlled coupling of a single-diamond nanocrystal to a photonic crystal cavity," *Optics Letters,* vol. 34, no. 7, pp. 1108-1110, 2009.

[77] Y.-C. Tsai, C.-F. Lin, and J.-W. Chang, "Controlling spontaneous emission with the local density of states of honeycomb photonic crystals," *Optical Review,* vol. 16, pp. 347-350, 2009.

[78] M. Felici, K. A. Atlasov, A. Surrente, and E. Kapon, “Semianalytical approach to the design of photonic crystal cavities,” *Physical Review B,* vol. 82, no. 11, pp. 115118, 2010.

[79] M. Nomura, K. Tanabe, S. Iwamoto, and Y. Arakawa, “High-Q design of semiconductor-based ultrasmall photonic crystal nanocavity,” *Optics Express,* vol. 18, no. 8, pp. 8144-8150, 2010.

[80] Y. Akahane, T. Asano, B.-S. Song, and S. Noda, “Fine-tuned high-Q photonic-crystal nanocavity,” *Optics Express,* vol. 13, no. 4, pp. 1202-1214, 2005.

[81] J. J. Baumberg, J. Aizpurua, M. H. Mikkelsen, and D. R. Smith, “Extreme nanophotonics from ultrathin metallic gaps,” *Nature Materials,* vol. 18, no. 7, pp. 668-678, 2019.

[82] N. J. Halas, S. Lal, W.-S. Chang, S. Link, and P. Nordlander, “Plasmons in strongly coupled metallic nanostructures,” *Chemical Reviews,* vol. 111, no. 6, pp. 3913-3961, 2011.

[83] R. Chikkaraddy, B. De Nijs, F. Benz, S. J. Barrow, O. A. Scherman, E. Rosta, A. Demetriadou, P. Fox, O. Hess, and J. J. Baumberg, “Single-molecule strong coupling at room temperature in plasmonic nanocavities,” *Nature,* vol. 535, no. 7610, pp. 127-130, 2016.

[84] K. Santhosh, O. Bitton, L. Chuntonov, and G. Haran, “Vacuum Rabi splitting in a plasmonic cavity at the single quantum emitter limit,” *Nature Communications,* vol. 7, no. 1, pp. ncomms11823, 2016.

[85] A. Krasnok, and A. Alù, “Active nanophotonics,” *Proceedings of the IEEE,* vol. 108, no. 5, pp. 628-654, 2020.

[86] P. N. Prasad, *Nanophotonics*: John Wiley & Sons, 2004.

[87] H. Shim, Z. Kuang, and O. D. Miller, “Optical materials for maximal nanophotonic response,” *Optical Materials Express,* vol. 10, no. 7, pp. 1561-1585, 2020.

[88] M.-S. Hwang, K.-Y. Jeong, J.-P. So, K.-H. Kim, and H.-G. Park, “Nanophotonic nonlinear and laser devices exploiting bound states in the continuum,” *Communications Physics,* vol. 5, no. 1, pp. 106, 2022.

[89] M. V. Rybin, K. L. Koshelev, Z. F. Sadrieva, K. B. Samusev, A. A. Bogdanov, M. F. Limonov, and Y. S. Kivshar, “High-Q supercavity modes in subwavelength dielectric resonators,” *Physical Review Letters,* vol. 119, no. 24, pp. 243901, 2017.

[90] K. Fan, R. D. Averitt, and W. J. Padilla, “Active and tunable nanophotonic metamaterials,” *Nanophotonics,* vol. 11, no. 17, pp. 3769-3803, 2022.

[91] P. Chopade, S. Jagtap, and S. Gosavi, "Material properties and potential applications of CdSe semiconductor nanocrystals," *Nanoscale Compound Semiconductors and Their Optoelectronics Applications*, pp. 105-153: Elsevier, 2022.

[92] S. Shukla, “Recent developments in biomedical applications of quantum dots,” *Adv Mater Rev,* vol. 1, no. 1, pp. 2-12, 2014.

[93] D. Granada-Ramírez, J. Arias-Cerón, P. Rodriguez-Fragoso, F. Vázquez-Hernández, J. Luna-Arias, J. Herrera-Perez, and J. Mendoza-Álvarez, "Quantum dots for biomedical applications," *Nanobiomaterials*, pp. 411-436: Elsevier, 2018.

[94] M. Chen, L. Lu, H. Yu, C. Li, and N. Zhao, "Integration of colloidal quantum dots with photonic structures for optoelectronic and optical devices," *Advanced Science,* vol. 8, no. 18, pp. 2101560, 2021.

[95] J. Wu, H. Ma, P. Yin, Y. Ge, Y. Zhang, L. Li, H. Zhang, and H. Lin, "Two-dimensional materials for integrated photonics: recent advances and future challenges," *Small Science,* vol. 1, no. 4, pp. 2000053, 2021.

[96] E. M. Dianov, "Bismuth-doped optical fibers: a challenging active medium for near-IR lasers and optical amplifiers," *Light: Science & Applications,* vol. 1, no. 5, pp. e12-e12, 2012.

[97] G. Pitruzzello, and T. F. Krauss, "Photonic crystal resonances for sensing and imaging," *Journal of Optics,* vol. 20, no. 7, pp. 073004, 2018.

[98] L. Zhang, S. Hu, Y. Lu, B. Jiang, X. Liu, X. Li, X. Zhao, X. Yan, C. Wang, and X. Jia, "Photonic crystal effects on upconversion enhancement of LiErF4: 0.5% Tm3+@ LiYF4 for noncontact cholesterol detection," *ACS Applied Materials & Interfaces,* vol. 14, no. 1, pp. 428-438, Jan 12, 2021.

[99] Y. Jia, J. Wu, X. Sun, X. Yan, R. Xie, L. Wang, Y. Chen, and F. Chen, "Integrated Photonics Based on Rare-Earth Ion-Doped Thin-Film Lithium Niobate," *Laser & Photonics Reviews,* vol. 16, no. 9, pp. 2200059, 2022.

[100] J. A. Gordon, and R. W. Ziolkowski, "The design and simulated performance of a coated nano-particle laser," *Optics Express,* vol. 15, no. 5, pp. 2622-2653, 2007.

[101] N. Passarelli, R. A. Bustos-Marún, and E. A. Coronado, "Spaser and optical amplification conditions in gold-coated active nanoparticles," *The Journal of Physical Chemistry C,* vol. 120, no. 43, pp. 24941-24949, 2016.

[102] N. Arnold, K. Piglmayer, A. V. Kildishev, and T. A. Klar, "Spasers with retardation and gain saturation: electrodynamic description of fields and optical cross-sections," *Optical Materials Express,* vol. 5, no. 11, pp. 2546-2577, 2015.

[103] M. Kasperczyk, S. Person, D. Ananias, L. D. Carlos, and L. Novotny, "Excitation of magnetic dipole transitions at optical frequencies," *Physical Review Letters,* vol. 114, no. 16, pp. 163903, 2015.

[104] D. G. Baranov, R. S. Savelev, S. V. Li, A. E. Krasnok, and A. Alù, "Modifying magnetic dipole spontaneous emission with nanophotonic structures," *Laser & Photonics Reviews,* vol. 11, no. 3, pp. 1600268, 2017.

[105] A. Vaskin, S. Mashhadi, M. Steinert, K. E. Chong, D. Keene, S. Nanz, A. Abass, E. Rusak, D.-Y. Choi, and I. Fernandez-Corbaton, "Manipulation of magnetic dipole emission from Eu3+ with Mie-resonant dielectric metasurfaces," *Nano Letters,* vol. 19, no. 2, pp. 1015-1022, 2019.

[106] B. Choi, M. Iwanaga, Y. Sugimoto, K. Sakoda, and H. T. Miyazaki, "Selective plasmonic enhancement of electric-and magnetic-dipole radiations of Er ions," *Nano Letters,* vol. 16, no. 8, pp. 5191-5196, 2016.

[107] A. B. Evlyukhin, C. Reinhardt, A. Seidel, B. S. Luk'yanchuk, and B. N. Chichkov, "Optical response features of Si-nanoparticle arrays," *Physical Review B,* vol. 82, no. 4, pp. 045404, 2010.

[108] A. García-Etxarri, R. Gómez-Medina, L. S. Froufe-Pérez, C. López, L. Chantada, F. Scheffold, J. Aizpurua, M. Nieto-Vesperinas, and J. J. Sáenz, "Strong magnetic response of submicron silicon particles in the infrared," *Optics Express,* vol. 19, no. 6, pp. 4815-4826, 2011.

[109] J. Li, N. Verellen, and P. Van Dorpe, "Enhancing magnetic dipole emission by a nano-doughnut-shaped silicon disk," *Acs Photonics,* vol. 4, no. 8, pp. 1893-1898, 2017.

[110] A. B. Evlyukhin, S. M. Novikov, U. Zywietz, R. L. Eriksen, C. Reinhardt, S. I. Bozhevolnyi, and B. N. Chichkov, "Demonstration of magnetic dipole resonances of dielectric nanospheres in the visible region," *Nano Letters,* vol. 12, no. 7, pp. 3749-3755, 2012.

[111] H. Sugimoto, and M. Fujii, "Magnetic Purcell enhancement by magnetic quadrupole resonance of dielectric nanosphere antenna," *ACS Photonics,* vol. 8, no. 6, pp. 1794-1800, 2021.

[112] C. F. a. H. Bohren, D. R., *Absorption and scattering of light by small particles*, New York: Wiley-Interscience, 1998.

[113] J. Xu, Y. Wu, P. Zhang, Y. Wu, R. A. Vallée, S. Wu, and X. Liu, "Resonant scattering manipulation of dielectric nanoparticles," *Advanced Optical Materials,* vol. 9, no. 15, pp. 2100112, 2021.

[114] P. D. Terekhov, K. V. Baryshnikova, Y. A. Artemyev, A. Karabchevsky, A. S. Shalin, and A. B. Evlyukhin, "Multipolar response of nonspherical silicon nanoparticles in the visible and near-infrared spectral ranges," *Physical Review B,* vol. 96, no. 3, pp. 035443, 2017.

[115] I. Sinev, I. Iorsh, A. Bogdanov, D. Permyakov, F. Komissarenko, I. Mukhin, A. Samusev, V. Valuckas, A. I. Kuznetsov, and B. S. Luk'yanchuk, "Polarization control over electric and magnetic dipole resonances of dielectric nanoparticles on metallic films," *Laser & Photonics Reviews,* vol. 10, no. 5, pp. 799-806, 2016.

[116] U. Zywietz, M. K. Schmidt, A. B. Evlyukhin, C. Reinhardt, J. Aizpurua, and B. N. Chichkov, "Electromagnetic resonances of silicon nanoparticle dimers in the visible," *Acs Photonics,* vol. 2, no. 7, pp. 913-920, 2015.

[117] H. Sugimoto, and M. Fujii, "Core/shell architecture made from Mie-resonant silicon nanoparticle: Design, fabrication, and photonic applications," *Chemical Physics Reviews,* vol. 5, no. 2, 2024.

[118] M. Wu, S. T. Ha, S. Shendre, E. G. Durmusoglu, W.-K. Koh, D. R. Abujetas, J. A. Sánchez-Gil, R. Paniagua-Domínguez, H. V. Demir, and A. I. Kuznetsov, "Room-temperature lasing in colloidal nanoplatelets via Mie-resonant bound states in the continuum," *Nano Letters,* vol. 20, no. 8, pp. 6005-6011, 2020.

[119] D. Sanvitto, and S. Kéna-Cohen, "Shiny condensates," *Nat. Mater,* vol. 15, pp. 1047, 2016.

[120] T. Volz, A. Reinhard, M. Winger, A. Badolato, K. J. Hennessy, E. L. Hu, and A. Imamoğlu, "Ultrafast all-optical switching by single photons," *Nature Photonics,* vol. 6, no. 9, pp. 605-609, 2012.

[121] H. Wang, J. Wen, W. Wang, N. Xu, P. Liu, J. Yan, H. Chen, and S. Deng, "Resonance coupling in heterostructures composed of silicon nanosphere and monolayer WS2: a magnetic-dipole-mediated energy transfer process," *ACS Nano,* vol. 13, no. 2, pp. 1739-1750, 2019.

[122] F. Todisco, R. Malureanu, C. Wolff, P. Gonçalves, A. S. Roberts, N. A. Mortensen, and C. Tserkezis, "Magnetic and electric Mie-exciton polaritons in silicon nanodisks," *Nanophotonics,* vol. 9, no. 4, pp. 803-814, 2020.

[123] J. Yan, C. Ma, P. Liu, C. Wang, and G. Yang, "Generating scattering dark states through the Fano interference between excitons and an individual silicon nanogroove," *Light: Science & Applications,* vol. 6, no. 1, pp. e16197-e16197, 2017.

[124] D. Rocco, A. Lamprianidis, A. E. Miroshnichenko, and C. De Angelis, "Giant electric and magnetic Purcell factor in dielectric oligomers," *JOSA B,* vol. 37, no. 9, pp. 2738-2744, 2020.

[125] Y. Brûlé, P. Wiecha, A. Cuche, V. Paillard, and G. C. des Francs, "Magnetic and electric Purcell factor control through geometry optimization of high index dielectric nanostructures," *Optics Express,* vol. 30, no. 12, pp. 20360-20372, 2022.

[126] S. A. Maier, *Plasmonics: fundamentals and applications*: Springer, 2007.

[127] V. Amendola, R. Pilot, M. Frasconi, O. M. Maragò, and M. A. Iatì, "Surface plasmon resonance in gold nanoparticles: a review," *Journal of Physics: Condensed Matter,* vol. 29, no. 20, pp. 203002, 2017.

[128] J. A. Polo Jr, and A. Lakhtakia, "Surface electromagnetic waves: a review," *Laser & Photonics Reviews,* vol. 5, no. 2, pp. 234-246, 2011.

[129] G. C. Papavassiliou, "Optical properties of small inorganic and organic metal particles," *Progress in Solid State Chemistry,* vol. 12, no. 3-4, pp. 185-271, 1979.

[130] Y. Chen, and H. Ming, "Review of surface plasmon resonance and localized surface plasmon resonance sensor," *Photonic Sensors,* vol. 2, pp. 37-49, 2012.

[131] S. V. Boriskina, T. A. Cooper, L. Zeng, G. Ni, J. K. Tong, Y. Tsurimaki, Y. Huang, L. Meroueh, G. Mahan, and G. Chen, "Losses in plasmonics: from mitigating energy dissipation to embracing loss-enabled functionalities," *Advances in Optics and Photonics,* vol. 9, no. 4, pp. 775-827, 2017.

[132] X. Huang, and M. A. El-Sayed, "Gold nanoparticles: Optical properties and implementations in cancer diagnosis and photothermal therapy," *Journal of Advanced Research,* vol. 1, no. 1, pp. 13-28, 2010.

[133] P. K. Jain, X. Huang, I. H. El-Sayed, and M. A. El-Sayed, "Review of some interesting surface plasmon resonance-enhanced properties of noble metal nanoparticles and their applications to biosystems," *Plasmonics,* vol. 2, pp. 107-118, 2007.

[134] T. Klar, M. Perner, S. Grosse, G. Von Plessen, W. Spirkl, and J. Feldmann, "Surface-plasmon resonances in single metallic nanoparticles," *Physical Review Letters,* vol. 80, no. 19, pp. 4249, 1998.

[135] M. Sasin, R. Seisyan, M. Kalitteevski, S. Brand, R. Abram, J. Chamberlain, A. Y. Egorov, A. Vasil'Ev, V. Mikhrin, and A. Kavokin, "Tamm plasmon polaritons: Slow and spatially compact light," *Applied Physics Letters,* vol. 92, no. 25, pp. 251112, 2008.

[136] M. Kaliteevski, I. Iorsh, S. Brand, R. Abram, J. Chamberlain, A. Kavokin, and I. Shelykh, "Tamm plasmon-polaritons: Possible electromagnetic states at the interface of a metal and a dielectric Bragg mirror," *Physical Review B,* vol. 76, no. 16, pp. 165415, 2007.

[137] C. Kar, S. Jena, D. V. Udupa, and K. D. Rao, "Tamm plasmon polariton in planar structures: A brief overview and applications," *Optics & Laser Technology,* vol. 159, pp. 108928, 2023.

[138] A. Philip, and A. R. Kumar, "The performance enhancement of surface plasmon resonance optical sensors using nanomaterials: A review," *Coordination Chemistry Reviews,* vol. 458, pp. 214424, 2022.

[139] N. Bellassai, R. D'Agata, V. Jungbluth, and G. Spoto, "Surface plasmon resonance for biomarker detection: advances in non-invasive cancer diagnosis," *Frontiers in Chemistry,* vol. 7, pp. 570, 2019.

[140] I. A. Shelykh, A. V. Kavokin, Y. G. Rubo, T. Liew, and G. Malpuech, "Polariton polarization-sensitive phenomena in planar semiconductor microcavities," *Semiconductor Science and Technology,* vol. 25, no. 1, pp. 013001, 2009.

[141] S. Tsintzos, N. Pelekanos, G. Konstantinidis, Z. Hatzopoulos, and P. Savvidis, "A GaAs polariton light-emitting diode operating near room temperature," *Nature,* vol. 453, no. 7193, pp. 372-375, 2008.

[142] B. Wang, P. Yu, W. Wang, X. Zhang, H. C. Kuo, H. Xu, and Z. M. Wang, "High-Q Plasmonic Resonances: Fundamentals and Applications," *Advanced Optical Materials,* vol. 9, no. 7, pp. 2001520, 2021.

[143] B. Auguié, M. C. Fuertes, P. C. Angelomé, N. L. Abdala, G. J. Soler Illia, and A. Fainstein, "Tamm plasmon resonance in mesoporous multilayers: toward a sensing application," *Acs Photonics,* vol. 1, no. 9, pp. 775-780, 2014.

[144] A. M. Ahmed, and A. Mehaney, "Ultra-high sensitive 1D porous silicon photonic crystal sensor based on the coupling of Tamm/Fano resonances in the mid-infrared region," *Scientific Reports,* vol. 9, no. 1, pp. 6973, 2019.

[145] E. Buzavaite-Verteliene, I. Plikusiene, T. Tolenis, A. Valavicius, J. Anulyte, A. Ramanavicius, and Z. Balevicius, "Hybrid Tamm-surface plasmon polariton mode for highly sensitive detection of protein interactions," *Optics Express,* vol. 28, no. 20, pp. 29033-29043, 2020.

[146] C. Symonds, G. Lheureux, J. P. Hugonin, J. J. Greffet, J. Laverdant, G. Brucoli, A. Lemaître, P. Senellart, and J. Bellessa, "Confined Tamm plasmon lasers," *Nano Letters,* vol. 13, no. 7, pp. 3179-3184, 2013.

[147] G. Lheureux, S. Azzini, C. Symonds, P. Senellart, A. Lemaître, C. Sauvan, J.-P. Hugonin, J.-J. Greffet, and J. Bellessa, "Polarization-controlled confined Tamm plasmon lasers," *ACS Photonics,* vol. 2, no. 7, pp. 842-848, 2015.

[148] M. Parker, E. Harbord, L. Chen, E. Clarke, K. Kennedy, J. Rarity, and R. Oulton, "Telecommunication wavelength confined Tamm plasmon structures containing InAs/GaAs quantum dot emitters at room temperature," *Physical Review B,* vol. 100, no. 16, pp. 165306, 2019.

[149] O. Gazzano, S. Michaelis de Vasconcellos, K. Gauthron, C. Symonds, P. Voisin, J. Bellessa, A. Lemaître, and P. Senellart, "Single photon source using confined Tamm plasmon modes," *Applied Physics Letters,* vol. 100, no. 23, 2012.

[150] S. Azzini, G. Lheureux, C. Symonds, J.-M. Benoit, P. Senellart, A. Lemaitre, J.-J. Greffet, C. Blanchard, C. Sauvan, and J. Bellessa, "Generation and spatial control of hybrid Tamm plasmon/surface plasmon modes," *ACS Photonics,* vol. 3, no. 10, pp. 1776-1781, 2016.

[151] Z.-Y. Yang, S. Ishii, T. Yokoyama, T. D. Dao, M.-G. Sun, P. S. Pankin, I. V. Timofeev, T. Nagao, and K.-P. Chen, "Narrowband wavelength selective thermal emitters by confined Tamm plasmon polaritons," *ACS Photonics,* vol. 4, no. 9, pp. 2212-2219, 2017.

[152] H. Lu, Y. Li, H. Jiao, Z. Li, D. Mao, and J. Zhao, "Induced reflection in Tamm plasmon systems," *Optics Express,* vol. 27, no. 4, pp. 5383-5392, 2019.

[153] C. P. Mavidis, A. C. Tasolamprou, S. B. Hasan, T. Koschny, E. N. Economou, M. Kafesaki, C. M. Soukoulis, and W. L. Vos, "Local density of optical states in the three-dimensional band gap of a finite photonic crystal," *Physical Review B,* vol. 101, no. 23, 2020.

[154] E. Yablonovitch, and T. Gmitter, "Photonic band structure: The face-centered-cubic case," *Physical Review Letters,* vol. 63, no. 18, pp. 1950, 1989.

[155] P. S. J. Russell, P. Hölzer, W. Chang, A. Abdolvand, and J. Travers, "Hollow-core photonic crystal fibres for gas-based nonlinear optics," *Nature Photonics,* vol. 8, no. 4, pp. 278-286, 2014.

[156] J. Joannopoulos, R. Meade, and J. Winn, "Photonic Crystals–Princeton," *Princeton, NJ*, 1995.

[157] P. Yeh, A. Yariv, and E. Marom, "Theory of Bragg fiber," *JOSA,* vol. 68, no. 9, pp. 1196-1201, 1978.

[158] T. A. Nguyen, and H. T. Dung, "Deterministic and storable single photons from a multilayer microsphere," *Physical Review A,* vol. 76, no. 3, 2007.

[159] A. Tandaechanurat, S. Ishida, D. Guimard, M. Nomura, S. Iwamoto, and Y. Arakawa, "Lasing oscillation in a three-dimensional photonic crystal nanocavity with a complete bandgap," *Nature Photonics,* vol. 5, no. 2, pp. 91-94, 2010.

[160] G. Burlak, S. Koshevaya, J. Sanchez-Mondragon, and V. Grimalsky, "Electromagnetic oscillations in a multilayer spherical stack," *Optics Communications,* vol. 180, no. 1-3, pp. 49-58, 2000.

[161] C. Vandenbem, and J. P. Vigneron, "Mie resonances of dielectric spheres in face-centered cubic photonic crystals," *J Opt Soc Am A Opt Image Sci Vis,* vol. 22, no. 6, pp. 1042-7, Jun, 2005.

[162] A. H. Taflove, Susan C, *Computational electrodynamics : the finite-difference time-domain method*, vol. 3, no. 15, pp. 629-670, Boston: MA : Artech House, 2005.

[163] I. L. Rasskazov, A. Moroz, and P. S. Carney, "Extraordinary fluorescence enhancement in metal-dielectric core-shell nanoparticles," *The Journal of Physical Chemistry Letters*, vol. 12, no. 27, pp. 6425-6430, 2021.

[164] L. K. Sørensen, A. D. Utyushev, V. I. Zakomirnyi, and H. Ågren, "Atomistic description of plasmonic generation in alloys and core shell nanoparticles," *Physical Chemistry Chemical Physics,* vol. 23, no. 1, pp. 173-185, 2021.

[165] Y. García-Puente, and R. Kashyap, "Spherical Bragg resonators for lasing applications: a theoretical approach," *Optics Express,* vol. 30, no. 26, pp. 47720-47732, 2022.

[166] J. Krupka, A. Cwikla, M. Mrozowski, R. N. Clarke, and M. E. Tobar, "High Q-factor microwave Fabry-Perot resonator with distributed Bragg reflectors," *IEEE Transactions on Ultrasonics, Ferroelectrics, and Frequency Control,* vol. 52, no. 9, pp. 1443-1451, 2005.

[167] M. E. Tobar, J.-M. Le Floch, D. Cros, and J. G. Hartnett, "Distributed Bragg reflector resonators with cylindrical symmetry and extremely high Q-factors," *IEEE Transactions on Ultrasonics, Ferroelectrics, and Frequency Control,* vol. 52, no. 1, pp. 17-26, 2005.

[168] O. V. Minin, S. Zhou, and I. V. Minin, "Optical Super-Resonances in Mesoscale Dielectric Cenosphere: Giant Magnetic Field Generations," *Annalen der Physik,* vol. 535, no 12, pp. 2300337, 2023.

[169] J.-M. Le Floch, M. E. Tobar, D. Mouneyrac, D. Cros, and J. Krupka, "Discovery of Bragg confined hybrid modes with high Q factor in a hollow dielectric resonator," *Applied Physics Letters,* vol. 91, no. 14, 2007.

[170] R. Gaponenko, M. S. Sidorenko, D. Zhirihin, I. L. Rasskazov, A. Moroz, K. Ladutenko, P. Belov, and A. Shcherbakov, "Experimental demonstration of superdirective spherical dielectric antenna," *Journal of Applied Physics,* vol. 134, no. 1, 2023.

[171] W. Liang, Y. Xu, Y. Huang, A. Yariv, J. Fleming, and S.-Y. Lin, "Mie scattering analysis of spherical Bragg "onion" resonators," *Optics Express,* vol. 12, no. 4, pp. 657-669, 2004.

[172] J. Krupka, M. E. Tobar, J. G. Hartnett, D. Cros, and J.-M. Le Floch, "Extremely high-Q factor dielectric resonators for millimeter-wave applications," *IEEE Transactions on Microwave Theory and Techniques,* vol. 53, no. 2, pp. 702-712, 2005.

[173] M. E. Tobar, J.-M. Le Floch, D. Cros, J. Krupka, J. D. Anstie, and J. G. Hartnett, "Spherical Bragg reflector resonators," *IEEE Transactions on Ultrasonics, Ferroelectrics, and Frequency Control,* vol. 51, no. 9, pp. 1054-1059, 2004.

[174] J.-M. Le Floch, G. Humbert, Q. Shan, D. Férachou, R. Bara-Maillet, M. Aubourg, J. G. Hartnett, V. Madrangeas, and D. Cros, "Invited article: Dielectric material characterization techniques and designs of high-Q resonators for applications from micro to millimeter-

waves frequencies applicable at room and cryogenic temperatures," *Review of Scientific Instruments,* vol. 85, no. 3, 2014.

[175] A. Kaur, J. C. Myers, M. I. M. Ghazali, J. Byford, and P. Chahal, "Affordable terahertz components using 3D printing," *IEEE 65th Electronic Components and Technology Conference*, pp. 2071-2076, 2015.

[176] A. Camposeo, L. Persano, M. Farsari, and D. Pisignano, "Additive Manufacturing: Applications and Directions in Photonics and Optoelectronics," *Adv Opt Mater,* vol. 7, no. 1, pp. 1800419, Jan 4, 2019.

[177] H. Y. Jeong, E. Lee, S.-C. An, Y. Lim, and Y. C. Jun, "3D and 4D printing for optics and metaphotonics," *Nanophotonics,* vol. 9, no. 5, pp. 1139-1160, 2020.

[178] F. Castles, D. Isakov, A. Lui, Q. Lei, C. E. Dancer, Y. Wang, J. M. Janurudin, S. C. Speller, C. R. Grovenor, and P. S. Grant, "Microwave dielectric characterisation of 3D-printed BaTiO3/ABS polymer composites," *Sci Rep,* vol. 6, pp. 22714, Mar 4, 2016.

[179] C. R. Tubío, J. A. Nóvoa, J. Martín, F. Guitián, J. R. Salgueiro, and A. Gil, "3D printing of Al2O3 photonic crystals for terahertz frequencies," *RSC Advances,* vol. 6, no. 3, pp. 2450-2454, 2016.

[180] Y. García-Puente, J.-J. Laurin, and R. Kashyap, "Photomic Crystals." *Frontiers in Optics + Laser Science APS/DLS*, Optica Publishing Group, pp. FTu6B. 4, 2019.

[181] X. Zhang, Z.-J. Wang, X. Wang, Y.-H. Zhang, J. Qu, and S.-N. Ding, "Band-Edge Effect-Induced Electrochemiluminescence Signal Amplification Based on Inverse Opal Photonic Crystals for Ultrasensitive Detection of Carcinoembryonic Antigen," *Analytical Chemistry,* vol. 94, no. 27, pp. 9919-9926, 2022.

[182] Y. Jang, G. Lee, E. Kim, and J. Rho, "Impulse mitigation in nonlinear composite-based woodpile phononic crystals," *Applied Physics Letters,* vol. 121, no. 20, pp. 201706, 2022.

[183] M. Gayathri, T. Alagesan, and N. Yogesh, "Cavity confinement in defect-based honeycomb photonic crystals and the design of waveguide–cavity fano-coupler for dielectric loss sensing," *Optics Communications,* vol. 508, pp. 127757, 2022.

[184] A. Dukin, "Investigation of the optical properties of a spherical distributed Bragg reflector," *Journal of Physics: Conference Series,* vol. 1400, no. 6, pp. 066005, 2019.

[185] T. Christopoulos, O. Tsilipakos, G. Sinatkas, and E. E. Kriezis, "On the calculation of the quality factor in contemporary photonic resonant structures," *Optics Express,* vol. 27, no. 10, pp. 14505-14522, 2019.

[186] V. Grigoriev, and F. Biancalana, "Exact analytical representations for broadband transmission properties of quarter-wave multilayers," *Optics Letters,* vol. 36, no. 19, pp. 3774-3776, 2011.

[187] V. Grigoriev, A. Tahri, S. Varault, B. Rolly, B. Stout, J. Wenger, and N. Bonod, "Optimization of resonant effects in nanostructures via Weierstrass factorization," *Physical Review A,* vol. 88, no. 1, pp. 011803, 2013.

[188] V. Grigoriev, A. Tahri, S. Varault, B. Rolly, B. Stout, J. Wenger, and N. Bonod, “Optimization of resonant effects in nanostructures via Weierstrass factorization,” *Physical Review A,* vol. 88, no. 1, 2013.

[189] J. M. Felício, C. A. Fernandes, and J. R. Costa, "Complex permittivity and anisotropy measurement of 3D-printed PLA at microwaves and millimeter-waves," *22nd International Conference on Applied Electromagnetics and Communications*. pp. 1-6, 2016.

[190] N. V. Gama, A. Ferreira, and A. Barros-Timmons, “Polyurethane foams: Past, present, and future,” *Materials,* vol. 11, no. 10, pp. 1841, 2018.

[191] K. J. Vahala, “Optical microcavities,” *Nature,* vol. 424, no. 6950, pp. 839-846, 2003.

[192] T. Reynolds, N. Riesen, A. Meldrum, X. Fan, J. M. Hall, T. M. Monro, and A. François, “Fluorescent and lasing whispering gallery mode microresonators for sensing applications,” *Laser & Photonics Reviews,* vol. 11, no. 2, pp. 1600265, 2017.

[193] N. Toropov, G. Cabello, M. P. Serrano, R. R. Gutha, M. Rafti, and F. Vollmer, “Review of biosensing with whispering-gallery mode lasers,” *Light: Science & Applications,* vol. 10, no. 1, pp. 1-19, 2021.

[194] A. Krasnok, D. Baranov, H. Li, M.-A. Miri, F. Monticone, and A. Alú, “Anomalies in light scattering,” *Advances in Optics and Photonics,* vol. 11, no. 4, pp. 892-951, 2019.

[195] W. J. Miniscalco, and R. S. Quimby, “General procedure for the analysis of Er 3+ cross sections,” *Optics letters,* vol. 16, no. 4, pp. 258-260, 1991.

[196] B. Brixner, “Refractive-index interpolation for fused silica,” *JOSA,* vol. 57, no. 5, pp. 674-676, 1967.

[197] E. D. Palik, *Handbook of optical constants of solids*: Academic press, 1998.

[198] Y. Chen, Y. Yin, L. Ma, and O. G. Schmidt, “Recent Progress on Optoplasmonic Whispering-Gallery-Mode Microcavities,” *Advanced Optical Materials,* vol. 9, no. 12, pp. 2100143, 2021.

[199] G. Burlak, and V. Grimalsky, “High quality electromagnetic oscillations in inhomogeneous coated microsphere,” *Optics Communications,* vol. 263, no. 2, pp. 342-349, Jul, 2006.

[200] D. Ramachari, L. R. Moorthy, and C. Jayasankar, “Gain properties and concentration quenching of Er3+-doped niobium oxyfluorosilicate glasses for photonic applications,” *Optical materials,* vol. 36, no. 4, pp. 823-828, 2014.

[201] A. Kennyon, “Recent Developments in Rare-Earth Doped Materials for Optoelectronics Progress,” *Quantum Electron,* vol. 26, pp. 225-284, 2002.

[202] R. L. Savio, M. Miritello, A. Shakoor, P. Cardile, K. Welna, L. Andreani, D. Gerace, T. Krauss, L. O’Faolain, and F. Priolo, “Enhanced 1.54 μm emission in Y-Er disilicate thin films on silicon photonic crystal cavities,” *Optics Express,* vol. 21, no. 8, pp. 10278-10288, 2013.

[203] Y. Gong, M. Makarova, S. Yerci, R. Li, M. J. Stevens, B. Baek, S. W. Nam, L. Dal Negro, and J. Vučković, “Observation of transparency of erbium-doped silicon nitride in photonic crystal nanobeam cavities,” *Optics Express,* vol. 18, no. 13, pp. 13863-13873, 2010.

[204] A. Polman, "Erbium implanted thin film photonic materials," *Journal of Applied Physics,* vol. 82, no. 1, pp. 1-39, 1997.

[205] M. Bayer, T. L. Reinecke, F. Weidner, A. Larionov, A. McDonald, and A. Forchel, "Inhibition and enhancement of the spontaneous emission of quantum dots in structured microresonators," *Physical Review Letters,* vol. 86, no. 14, pp. 3168, 2001.

[206] T. Jakubczyk, H. Franke, T. Smolenski, M. Sciesiek, W. Pacuski, A. Golnik, R. d. Schmidt-Grund, M. Grundmann, C. Kruse, and D. Hommel, "Inhibition and enhancement of the spontaneous emission of quantum dots in micropillar cavities with radial-distributed Bragg reflectors," *ACS Nano,* vol. 8, no. 10, pp. 9970-9978, 2014.

[207] Z.-J. Yang, R. Jiang, X. Zhuo, Y.-M. Xie, J. Wang, and H.-Q. Lin, "Dielectric nanoresonators for light manipulation," *Physics Reports,* vol. 701, pp. 1-50, 2017.

[208] A. I. Kuznetsov, A. E. Miroshnichenko, M. L. Brongersma, Y. S. Kivshar, and B. Luk'yanchuk, "Optically resonant dielectric nanostructures," *Science,* vol. 354, no. 6314, pp. aag2472, 2016.

[209] M. Decker, and I. Staude, "Resonant dielectric nanostructures: a low-loss platform for functional nanophotonics," *Journal of Optics,* vol. 18, no. 10, pp. 103001, 2016.

[210] S. Jahani, and Z. Jacob, "All-dielectric metamaterials," *Nature Nanotechnology,* vol. 11, no. 1, pp. 23-36, 2016.

[211] W. J. Padilla, and R. D. Averitt, "Imaging with metamaterials," *Nature Reviews Physics,* vol. 4, no. 2, pp. 85-100, 2022.

[212] T. Feng, W. Zhang, Z. Liang, and Y. Xu, "Unidirectional emission in an all-dielectric nanoantenna," *Journal of Physics: Condensed Matter,* vol. 30, no. 12, pp. 124002, 2018.

[213] W. Yang, S. Xiao, Q. Song, Y. Liu, Y. Wu, S. Wang, J. Yu, J. Han, and D.-P. Tsai, "All-dielectric metasurface for high-performance structural color," *Nature Communications,* vol. 11, no. 1, pp. 1-8, 2020.

[214] Q. Zhao, J. Zhou, F. Zhang, and D. Lippens, "Mie resonance-based dielectric metamaterials," *Materials Today,* vol. 12, no. 12, pp. 60-69, 2009.

[215] M. Caldarola, P. Albella, E. Cortés, M. Rahmani, T. Roschuk, G. Grinblat, R. F. Oulton, A. V. Bragas, and S. A. Maier, "Non-plasmonic nanoantennas for surface enhanced spectroscopies with ultra-low heat conversion," *Nature Communications,* vol. 6, no. 1, pp. 1-8, 2015.

[216] A. E. Krasnok, A. Maloshtan, D. N. Chigrin, Y. S. Kivshar, and P. A. Belov, "Enhanced emission extraction and selective excitation of NV centers with all–dielectric nanoantennas," *Laser & Photonics Reviews,* vol. 9, no. 4, pp. 385-391, 2015.

[217] I. Staude, V. V. Khardikov, N. T. Fofang, S. Liu, M. Decker, D. N. Neshev, T. S. Luk, I. Brener, and Y. S. Kivshar, "Shaping photoluminescence spectra with magnetoelectric resonances in all-dielectric nanoparticles," *ACS Photonics,* vol. 2, no. 2, pp. 172-177, 2015.

[218] A. Matsumori, H. Sugimoto, and M. Fujii, "Silicon Nanosphere with Accessible Magnetic Hotspot," *Advanced Optical Materials,* vol. 10, no. 8, pp. 2102574, 2022.

[219] S. Karaveli, S. Wang, G. Xiao, and R. Zia, "Time-resolved energy-momentum spectroscopy of electric and magnetic dipole transitions in Cr3+: MgO," *ACS Nano,* vol. 7, no. 8, pp. 7165-7172, 2013.

[220] I. L. Rasskazov, A. Moroz, and P. S. Carney, "Extraordinary Fluorescence Enhancement in Metal-Dielectric Core-Shell Nanoparticles," *J Phys Chem Lett,* vol. 12, no. 27, pp. 6425-6430, Jul 15, 2021.

[221] S. Sun, I. L. Rasskazov, P. S. Carney, T. Zhang, and A. Moroz, "Critical Role of Shell in Enhanced Fluorescence of Metal–Dielectric Core–Shell Nanoparticles," *The Journal of Physical Chemistry C,* vol. 124, no. 24, pp. 13365-13373, 2020.

[222] Y. Xu, W. Liang, A. Yariv, J. Fleming, and S.-Y. Lin, "High-quality-factor Bragg onion resonators with omnidirectional reflector cladding," *Optics Letters,* vol. 28, no. 22, pp. 2144-2146, 2003.

[223] A. D. Utyushev, R. Gaponenko, S. Sun, A. Shcherbakov, A. Moroz, and I. L. Rasskazov, "Generation of nearly pure and highly directional magnetic light in fluorescence of rare earth ions," *arXiv preprint arXiv:2212.05552*, 2022.

[224] P. Albella, M. A. Poyli, M. K. Schmidt, S. A. Maier, F. Moreno, J. J. Sáenz, and J. Aizpurua, "Low-loss electric and magnetic field-enhanced spectroscopy with subwavelength silicon dimers," *The Journal of Physical Chemistry C,* vol. 117, no. 26, pp. 13573-13584, 2013.

[225] B. Reynier, E. Charron, O. Markovic, X. Yang, B. Gallas, A. Ferrier, S. Bidault, and M. Mivelle, "Full control of electric and magnetic light–matter interactions through a nanomirror on a near-field tip," *Optica,* vol. 10, no. 7, pp. 841-845, 2023.

[226] N. de Sousa, L. S. Froufe-Pérez, J. J. Sáenz, and A. García-Martín, "Magneto-optical activity in high index dielectric nanoantennas," *Scientific Reports,* vol. 6, no. 1, pp. 30803, 2016.

[227] S. Xia, D. O. Ignatyeva, Q. Liu, J. Qin, T. Kang, W. Yang, Y. Chen, H. Duan, L. Deng, and D. Long, "Enhancement of the Faraday effect and magneto-optical figure of merit in all-dielectric metasurfaces," *ACS Photonics,* vol. 9, no. 4, pp. 1240-1247, 2022.

[228] A. A. Voronov, D. Karki, D. O. Ignatyeva, M. A. Kozhaev, M. Levy, and V. I. Belotelov, "Magneto-optics of subwavelength all-dielectric gratings," *Optics Express,* vol. 28, no. 12, pp. 17988-17996, 2020.

[229] J. Qin, S. Xia, W. Yang, H. Wang, W. Yan, Y. Yang, Z. Wei, W. Liu, Y. Luo, and L. Deng, "Nanophotonic devices based on magneto-optical materials: recent developments and applications," *Nanophotonics*, 2022.

[230] N. Maccaferri, K. E. Gregorczyk, T. V. De Oliveira, M. Kataja, S. Van Dijken, Z. Pirzadeh, A. Dmitriev, J. Åkerman, M. Knez, and P. Vavassori, "Ultrasensitive and label-free molecular-level detection enabled by light phase control in magnetoplasmonic nanoantennas," *Nature Communications,* vol. 6, no. 1, pp. 6150, 2015.

[231] K.-J. Jeong, D. K. Lee, V. T. Tran, C. Wang, J. Lv, J. Park, Z. Tang, and J. Lee, "Helical magnetic field-induced real-time plasmonic chirality modulation," *ACS Nano,* vol. 14, no. 6, pp. 7152-7160, 2020.

[232] L. Petit, J. Griffin, N. Carlie, V. Jubera, M. García, F. Hernández, and K. Richardson, "Luminescence properties of Eu3+ or Dy3+/Au co-doped SiO2 nanoparticles," *Materials Letters,* vol. 61, no. 14-15, pp. 2879-2882, 2007.

[233] B. Min, E. Ostby, V. Sorger, E. Ulin-Avila, L. Yang, X. Zhang, and K. Vahala, "High-Q surface-plasmon-polariton whispering-gallery microcavity," *Nature,* vol. 457, no. 7228, pp. 455-458, 2009.

[234] M. G. Silveirinha, "Trapping light in open plasmonic nanostructures," *Physical Review A,* vol. 89, no. 2, pp. 023813, 2014.

[235] X. Yang, G. Xiao, Y. Lu, and G. Li, "Narrow plasmonic surface lattice resonances with preference to asymmetric dielectric environment," *Optics express,* vol. 27, no. 18, pp. 25384-25394, 2019.

[236] W. Zhou, and T. W. Odom, "Tunable subradiant lattice plasmons by out-of-plane dipolar interactions," *Nature Nanotechnology,* vol. 6, no. 7, pp. 423-427, 2011.

[237] J.-Y. Jing, Q. Wang, W.-M. Zhao, and B.-T. Wang, "Long-range surface plasmon resonance and its sensing applications: A review," *Optics and Lasers in Engineering,* vol. 112, pp. 103-118, 2019.

[238] S. a. Pillai, and M. Green, "Plasmonics for photovoltaic applications," *Solar Energy Materials and Solar Cells,* vol. 94, no. 9, pp. 1481-1486, 2010.

[239] L. Wang, M. Hasanzadeh Kafshgari, and M. Meunier, "Optical properties and applications of plasmonic-metal nanoparticles," *Advanced Functional Materials,* vol. 30, no. 51, pp. 2005400, 2020.

[240] M. A. García, "Surface plasmons in metallic nanoparticles: fundamentals and applications," *Journal of Physics D: Applied Physics,* vol. 44, no. 28, pp. 283001, 2011.

[241] L. Meng, R. Yu, M. Qiu, and F. J. García de Abajo, "Plasmonic nano-oven by concatenation of multishell photothermal enhancement," *ACS Nano,* vol. 11, no. 8, pp. 7915-7924, 2017.

[242] B. Auguié, A. Bruchhausen, and A. Fainstein, "Critical coupling to Tamm plasmons," *Journal of Optics,* vol. 17, no. 3, pp. 035003, 2015.

[243] C. Symonds, G. Lheureux, J. P. Hugonin, J. J. Greffet, J. Laverdant, G. Brucoli, A. Lemaitre, P. Senellart, and J. Bellessa, "Confined Tamm plasmon lasers," *Nano Letters,* vol. 13, no. 7, pp. 3179-3184, 2013.

[244] Y. García-Puente, and R. Kashyap, "Magnetic Purcell Enhancement in a Nanoantenna-Spherical Bragg Resonator Coupled System," *Annalen der Physik*, pp. 2300147, 2023.

[245] M. G. Blaber, M. D. Arnold, and M. J. Ford, "A review of the optical properties of alloys and intermetallics for plasmonics," *Journal of Physics: Condensed Matter,* vol. 22, no. 14, pp. 143201, 2010.

[246] E. Le Ru, and P. Etchegoin, "SPlaC package v1. 0 guide and supplementary information," *Victoria University, Tech. Rep*, 2008.

[247] E. Le Ru, and P. Etchegoin, "SERS and plasmonics codes (SPlaC)," *Matlab codes freely available from http://www. vuw. ac. nz/raman/book/codes. aspx*, 2009.

[248] C. Little, R. Anufriev, I. Iorsh, M. Kaliteevski, R. Abram, and S. Brand, “Tamm plasmon polaritons in multilayered cylindrical structures,” *Physical Review B,* vol. 86, no. 23, pp. 235425, 2012.

[249] Z. Wang, J. K. Clark, Y.-L. Ho, B. Vilquin, H. Daiguji, and J.-J. Delaunay, “Narrowband thermal emission realized through the coupling of cavity and Tamm plasmon resonances,” *ACS Photonics,* vol. 5, no. 6, pp. 2446-2452, 2018.

.

APPENDIX A LIST OF PUBLICATION

Journal Publications

- **Y. García-Puente** Baptiste Auguié and R. Kashyap, " High-Q Tamm plasmon-like resonance in Spherical Bragg microcavity Resonators", Optics Express, (Accepted, Feb 2024).
- **Y. García-Puente**, J.-J. Laurin and R. Kashyap, Experimental characterization of Spherical Bragg Resonators for electromagnetic emission engineering at microwave frequencies, Scientific Reports 13 (2023) 20532.
- **Y. García-Puente** and R. Kashyap, Magnetic Purcell Enhancement in a Nanoantenna-Spherical Bragg Resonator Coupled System, Annalen der Physik (2023) 2300147.
- A.R. Hlil, J.-S. Boisvert, H.M. Titi, **Y. Garcia-Puente**, W. Correr, S. Loranger, J. Thomas, A. Riaz, Y. Messaddeq, R. Kashyap, Effect of Photoinitiators Doped in PDMS for Femtosecond-Laser Writing: Characterization and Outcomes, ACS omega (2023).
- **Y. García-Puente** and R. Kashyap, "Spherical Bragg resonators for lasing applications: a theoretical approach," Optics Express **30**, 47720-47732 (2022).
- A. R. Hlil, J. Thomas, **Y. Garcia-Puente**, J.-S. Boisvert, B. C. Lima, A. Rakotonandrasana, L. J. Maia, A. Tehranchi, S. Loranger, and A. S. Gomes, "Structural and optical properties of Nd: YAB-nanoparticle-doped PDMS elastomers for random lasers," *Scientific reports,* vol. 11, no. 1, pp. 1-10, 2021.
- E. Martínez-Montes, **Y. García-Puente**, M. Zañartu, and P. Prado-Gutierrez, "Chirp analyzer for estimating amplitude and latency of steady-state auditory envelope following responses," *IEEE Transactions on Neural Systems and Rehabilitation Engineering,* vol. 28, no. 12, pp. 2744-2753, 2020.
- A. Hlil, B. Lima, J. Thomas, J.-S. Boisvert, H. Iden, **Y. Garcia-Puente**, L. Maia, Y. Ledemi, Y. Messaddeq, and A. Gomes, "Rare earth doped PDMS elastomeric random lasers," *Optical Materials,*vol. 97, pp. 109387, 2019.
- **Y. García-Puente**, A. Santana-Gil, A. Peláiz-Barranco, O. García-Zaldívar, F. Calderón-Piñar, and A. C. García-Wong, "Device for the Detection of Mechanical Pulses by Using a Piezoelectric Sensor," *Revista Cubana de Física,* vol. 28, no. 2, pp. 5, 2011-12-15, 2011.

• **Y. García-Puentes**, A. Santana-Gil, and A. Peláiz-Barranco, “Automatization of a Measuring System for Material Analysis by Application of AC Electric Fields,” *Revista Cubana de Física,* vol. 26, no. 2B, pp. 4, 2009-12-15, 2009.

Conference Papers

• **Y. García-Puente**, J. J. Laurin, R. Kashyap, “Photomic Crystals”, Frontiers in Optics, Optical Society of America, 2019, p. FTu6B-4.